Performance Evaluation of Phoswich Detector Cell for the Balloon-Borne Astronomical Soft Gamma-Ray Polarimeter PoGOLite

Kanai, Yoshikazu

Master thesis

Department of Particle-, Nuclear-, and Astro-Physics,
Graduate School of Science and Engineering,
Tokyo Institute of Technology

February, 2007

Abstract

Soft gamma-ray polarimetry is expected to reveal the emission mechanism of high-energy astrophysical sources and the material distribution around the sources. However, no significant results have not obtained. We are developing a soft gamma-ray polarimetry experiment with a balloon, PoGOLite (Polarized Gamma-Ray Polarimeter − Light Version) aiming for the first observation in 2009. PoGOLite will perform a most sensitive polarization measurements ever in the energy band of 25−100 keV. The main detector of the polarimeter is the Phoswich Detector Cell (PDC) using three kinds of scintillators read out by a photomultiplier tube (PMT). Evaluation of the performance of the PDC is an important part of the development. In this study, we have performed following three experiments.

After the procurement of PoGOLite flight-model PMT assemblies (PMT-ASSYs) was started, we have conducted their acceptance tests. We have developed an efficient testing procedure in the limited time and actually tested 53 PMT-ASSYs. The test items cover the bias voltage dependency on the gain, the power consumption, cramping of large output signals, the noise level and the behavior in low temperatures. All PMT-ASSYs but four ones with high noise levels were found to work properly.

In order to examine the performance of the PDC when it is used in the polarimeter, we have constructed a prototype polarimeter using a unit of the flight-model PDC and tested it with a polarized X-ray beam. The beam energies were set to 30, 50 and 70 keV. The modulation factor, which represents the performance of the polarimeter, and the detection efficiency are derived. The experimental values are compared to the results obtained with a Monte Carlo simulation with the Geant4 and they are consistent within $\sim 10\%$ accuracy. These results show that the prototype polarimeter performed in line with the simulation.

The flight-model PDC and PMT-ASSY has been tested with a proton beam for the evaluation of the whole PDC system to the cosmic-ray background at the balloon altitude. It will be used as a feedback to the future development of the signal processing electronics. As a result, we find that the system is not affected significantly by the proton rate an order of magnitude larger than the background rate expected in flight. In addition, we propose a new pulse shape discrimination method, which is used to identify the emitting scintillator in the PDC. This method will provide the better discrimination performance and the simpler electronics than those with another established method we have often used.

Contents

List of Figures

List of Tables

Chapter 1

Introduction

1.1 Background on X-ray and gamma-ray polarimetry

Celestial sources can be studied via the electromagnetic radiation using their spectrum, time variability, two-dimensional projected image and polarization degree and angle. In the longer wavelengths from the radio band to the optical band, these four ways are commonly utilized. On the other hand in the shorter wavelengths band above X-ray, only the former three parameters can be obtained. For a number of X-ray and gamma-ray sources, such observations alone do not identify the dominant emission mechanism and polarization measurements are expected to yield important additional information. Spectral dependence of polarization helps identifying the emission process and orientation of the polarization plane probes the distributions of magnetic field, radiation field, and matter around the sources. Polarization measurement will be particularly important for study on pulsars, accreting black holes, and jet-dominated active galaxies. Strong X-ray and gamma-ray polarization can arise from synchrotron emission in ordered magnetic fields, photon propagation in extremely strong magnetic fields ($B > 10^{12}$ gauss) and anisotropic Compton scattering [1].

Despite potential importance of polarization measurement, there has been only one significant polarization detection in the X-ray band (2.6 and 5.2 keV) from the Crab nebula with an instrument aboard the OSO-8 satellite using Bragg diffraction [2, 3]. Due to its small effective area, the instrument was not able to detect polarization from the Crab pulsar and other sources [4, 5]. In the hard X-ray and gamma-ray band, polarization has not been detected significantly for sources other than the sun [6]. There is a report of polarization detection from a gamma-ray burst with an instrument on the RHESSI satel-

lite in 2002 [7]. This claim has been seriously challenged and hence remains controversial [8, 9].

Polarization measurements are known to be most effective in the hard X-ray and soft gamma-ray band where non-thermal processes are expected to produce high degrees of polarization. Two techniques have been developed to measure X-ray or soft gamma-ray polarization from astrophysical sources. Below 10 keV, polarization can be deduced by tracking the electron from photo-absorption in an imaging gas detector (see [10] for example). From $\sim$ 25 keV to a few hundred keV, polarization can be determined by measuring the azimuthal angle distribution of Compton-scattered photons. To apply the polarimetry technique to astronomical observation, an instrument is generally launched into a satellite orbit because X-rays and gamma-rays are absorbed by the earth atmosphere. However, now it is regarded as quite risky to launch instruments aboard satellites, in view of the failures of the past. Instruments relying on the latter technique can make observation even on a high altitude balloon because the atmospheric overburden ($\sim 3-4$ g/cm^2) is transparent in its energy range ($>$ 25 keV). For balloon experiments, it is rather easy to develop instruments and the launches cost much less (a few hundred thousand dollars), compared to satellites. On the other hand, the short observation time (from several hours to a month) and the large background produced by cosmic-ray particles in this energy band decrease the sensitivity, and poses a big challenge for the detector design.

Recently, polarimetry techniques have been well cultivated through ground-based experiments. Several instruments are under development to detect X-ray or gamma-ray polarization from astronomical sources on the Compton scattering technique: some are designed for flights on a balloon and other on a satellite. Most instruments set their primary target at gamma-ray bursts including POLAR [11] ($E = 10-300$ keV, satellite) and GRAPE [12] ($E = 50-300$ keV, long-duration balloon or satellite). PHENEX [13] is designed to detect 10 % polarization from Crab nebula in the $40-300$ keV range in a 3-hour balloon observation. CIPHER [14] is designed for observing steady sources in the energy range between 10 keV and 1 MeV with capability of detecting 5 % polarization in the Crab nebula in a 3-hour observation on a satellite orbit.

1.2 PoGOLite project

Polarized Gamma-ray Observer − Light Version (PoGOLite) is a balloon-borne astronomical soft gamma-ray polarimeter and measures polarization in the energy range of $25-100$ keV by using the azimuthal angle anisotropy of Compton scattered photons. PoGOLite is an international collaboration of the United States (Stanford Linear Accel-

erator Center, University of Hawaii), Sweden (Royal Institute of Technology, Stockholm University), France (Ecole Polytechnique) and Japan (Tokyo Institute of Technology, Hiroshima University, Institute of Space and Astronautical Science, Yamagata University). The first observation is scheduled in 2009. Prior to it, a flight of a scaled-down engineering model is also planned in 2008.

1.2.1 Technical overview

The PoGOLite detector consists of a hexagonal close-packed array of 217 well-type phoswich detector cells (PDCs) made of two kinds of plastic scintillators and bismuth germanate oxide (BGO) scintillators and 54 side anti-coincidence detectors (SAS) made of BGO scintillators, as shown in figure 1.1. This design is based on the well-type phoswich technology proven to be very effective in reducing cosmic-ray background through the WELCOME balloon experiment [15, 16, 17, 18, 19, 20, 21] and the Hard X-ray Detector aboard Suzaku, the fifth Japanese satellite for X-ray astronomy [22, 23, 24, 25, 26, 27, 28, 29].

The instrument was originally designed as an array of 397 PDCs and 72 SASs, PoGO [30, 31, 32]. Through the detector simulation and design, cost estimation and prototype testing, we reached the lighter version, PoGOLite. The lighter-weight design will allow to reach a higher altitude (42 km with a 1.11 million m^3 balloon) and thus a smaller atmospheric overburden of 3 g/cm^2. This decreases the lower energy limit to 25 keV. The lighter design also simplifies implementation of rotating mechanism around its axis, which is essential in reducing systematic errors in polarization measurement.

Each PDC, as shown in figure 1.2, is composed of a thin-walled tube (well) of a plastic scintillator at the top ('slow scintillator,' fluorescence decay time 285 ns), a solid rod of a plastic scintillator ('fast scintillator,' decay time 2 ns), and a BGO crystal at the bottom (decay time 300 ns), all viewed by one photomultiplier tube (PMT). We developed PMT assemblies (hereafter PMT-ASSY) which include PMTs, circuits and high voltage modules (detailed description in chapter 3). The wells serve as an active collimator, the fast scintillators as Compton scatterer and active photon detectors, and the bottom BGOs act as a lower active shield. We also use thin tin and lead foils wrapped around the slow scintillator tubes as passive collimator for the low-energy photons. Signals from the fast scintillator and those from the slow/BGO scintillator can be discriminated by their temporal profiles (Pulse Shape Discrimination, PSD). In this work, we performed PSD by comparing the outputs from two shaping amplifiers with different shaping times ('double integration method') in chapter 4, and by examining the rise times of output waveforms from a charge sensitive amplifier (CSA) in chapter 5. Each SASs is consisted of three BGO scintillator rods with 20 cm tall and 4 cm wide. They are optically connected in

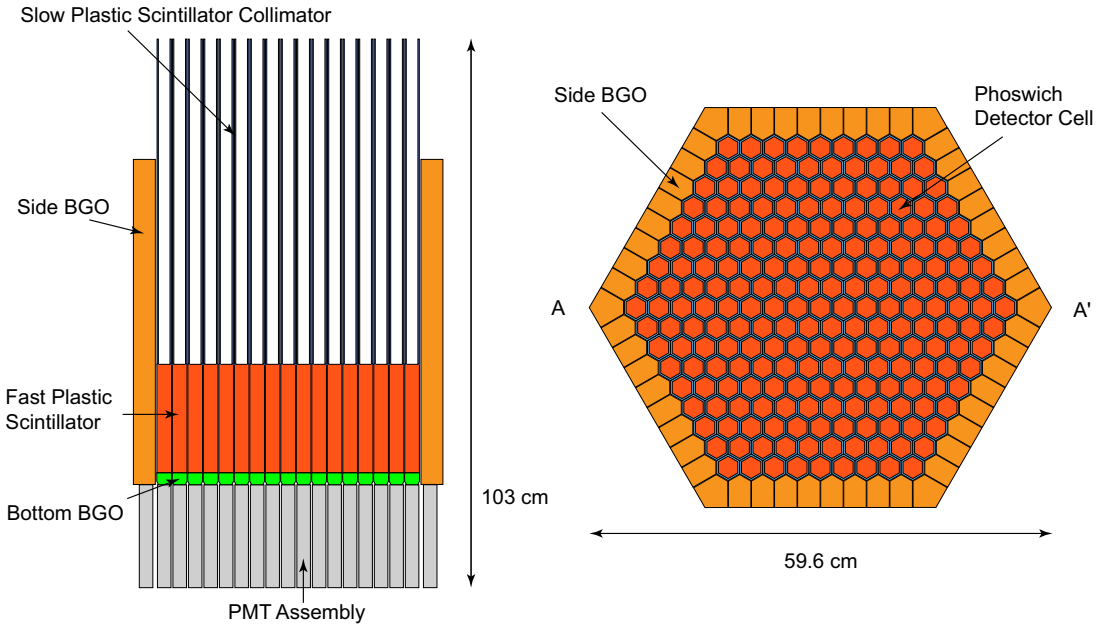

Figure 1.1: The PoGOLite detector array. Vertical cross-section AA' (left) and top view (right).

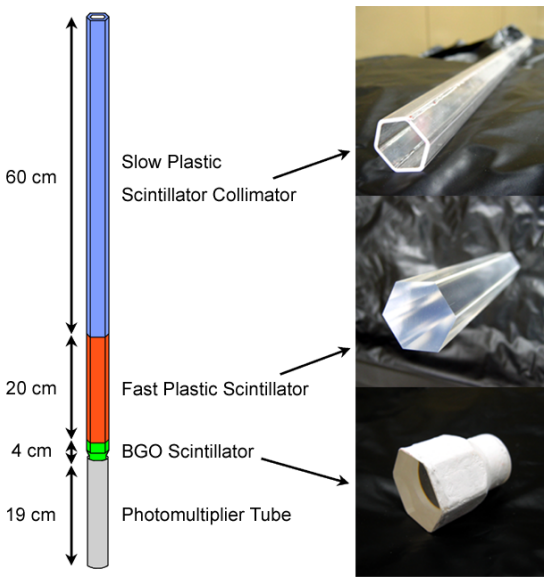

Figure 1.2: A schematic view of a PDC and photographs of the component scintillators. The diameter of PMT is 2.6 cm and the width of scintillators is $\sim$ 2.7 cm.

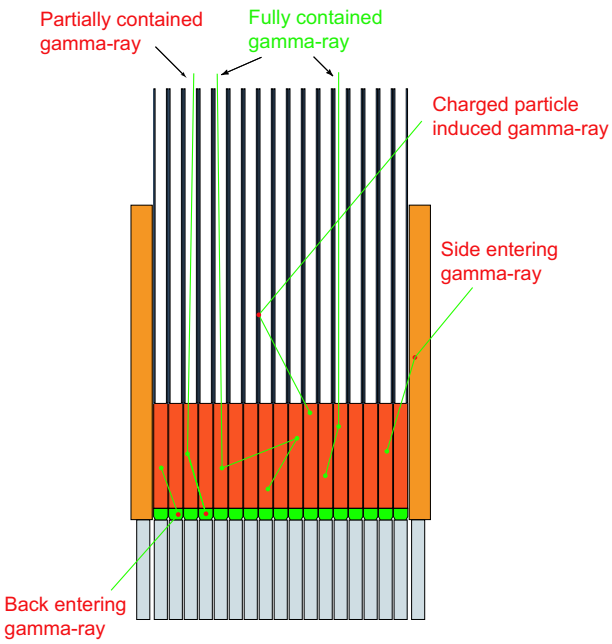

Figure 1.3: Possible photon interactions in the instrument. The green circles represent energy depositions in the fast scintillators while red ones for the anti-coincidence detectors. We accept only the 'fully contained gamma-ray' events.

their longitudinal and read by a PMT. Figure 1.3 shows possible photon interactions in the instrument.

The energy deposited in a valid Compton scattering event is measured at least two locations in the fast scintillators, the Compton scattering site and the photo-absorption site. The direction of the scattered photon is deduced from the relative magnitudes of the energy deposited at these locations. The polarization is simply determined from the distribution of azimuthal scattering angles. See §2.2 for the detailed description on polarimetry relying on the Compton kinematics. A coincidence of multiple background events can be ruled out by imposing energy depositions compatible with Compton scattering. This is the 'Compton kinematics filtering.'

Major background sources are cosmic-rays, atmospheric gamma-rays and astronomical gamma-rays. The detector response to the latter two kinds has been studied by Monte Carlo simulation with a realistic background model for the balloon environment [33]. If gamma-rays enter the Compton scatterer from the aperture, they become irreducible background. Gamma-rays can be scattered in the collimator without being detected and hit the Compton scatterer, they also become background. These gamma-rays are reduced by making the aperture narrow ($\sim 2.4 \times 2.4$ deg^2), surrounding the Compton scatterer with thick BGO crystals, and Compton kinematics filtering. Background related to charged cosmic-rays is eliminated by the BGO shields and the active collimator embedded in the

PDCs. Background due to neutrons is reduced to a negligible level by tight Compton kinematics filter. The background rate is expected to be equivalent to $\sim$ 10 mCrab[1] at 40 keV.

Current design of data acquisition (DAQ) system is as below. Signals from all PMTs in the 217 PDCs are constantly digitized with flash ADCs (analog to digital converters) at 20 MHz or higher. Events with pulse height between lower and upper threshold levels trigger the system and waveforms of all units are read. The event is recorded in data storage if passing the following criteria;

- hit pattern is valid (e.g. not too many PDCs are hit or hit PDCs are not separated much);
- there is no PDC with upper discriminator hit;
- no slow or BGO scintillators are hit.

The stored data are processed by the off-line analysis. The SASs will not be used to veto events in flight because the trigger rate of SASs are expected so high ($\sim$ 100 kHz) as to eliminate valid events by chance coincidence, but the waveforms will be recorded for subsequent analysis. We estimate that the event recording rate is reduced to 0.5$-$1 kHz from the original hit rate of $\sim$ 13 kHz.

The pointing system and gondola design have been adopted from the flight-proven High Energy Focusing Telescope (HEFT) design [34]. Figure 1.4 is a sketch of the gondola. The height and width will be 3.0$-$3.5 m and $\sim$ 2 m, respectively. The polarimeter in a pressure vessel, which prevents discharge, is mounted on an offset pivot to allow full-sky viewing. The pointing accuracy is better than 5% of the field of view which maximizes the effective area. A GPS with four antennas, two star trackers, gyroscopes, accelerometers and magnetometers determine the attitude, and the polarimeter tracks targets with two fly wheels for elevation and azimuth. The polarimeter rotates around its optical axis to cancel out the systematic bias in the observed polarization. The total weight of the payload other than the ballast will be 1000 kg. The level flight altitude will be $>$ 41 km (3 g/cm^2 atmospheric overburden) with a 1.11 M m^3 balloon. The overall design of the PoGOLite polarimeter and gondola has incorporated features needed to make long duration balloon flights from Sweden to North America.

Finally, we summarize the performance of PoGOLite in table 1.1.

[1] 'Crab' is a unit of the photon flux normalized with the summed flux from Crab nebula and Crab pulsar. The intensity of 1 Crab is $\frac{dN}{dE} = 9.7 \times E^{-2.1}$[photons/s/cm^2/keV] in 20$-$200 keV, where E is the energy in keV.

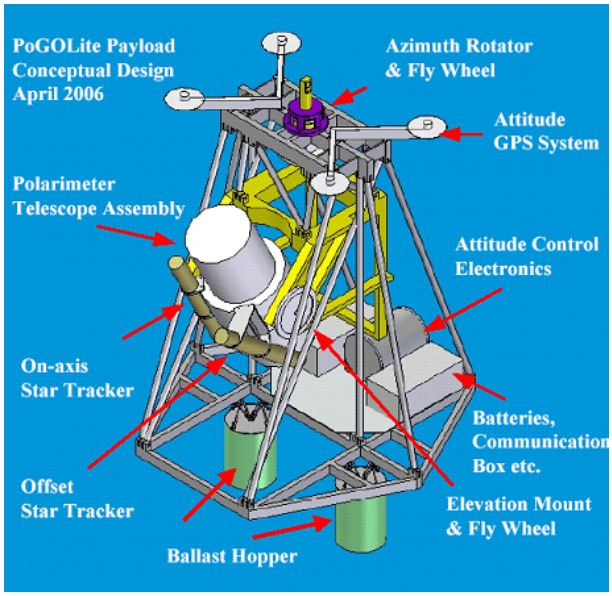

Figure 1.4: The design of a gondola for PoGOLite. The polarimeter in a pressure vessel (the white cylinder at the center) tracks the target source with using two fly wheels for elevation and azimuth.

Table 1.1: The performance of PoGOLite.

Nominal energy band	25−100 keV
Geometrical area	934 cm^2
Effective area (at 40 keV)	260 cm^2
Field of view	2.4×2.4 deg^2
Background (at 40 keV)	$\sim$ 10 mCrab
Modulation factor † (at 40 keV)	0.23
Minimum detectable polarization with	
3σ confidence for 100 mCrab sources	10 %

† Modulation factor represents how the full (100%) polarization is smeared by the detector (see §2.2).

1.2.2 Scientific goals

Most of high-energy astronomical sources are predicted to be polarized in the X-ray and gamma-ray bands from their emission models. Since there is no polarimetry data, numerous sources are interesting sources to be studied. We pick up three classes of sources expected to be highly polarized.

Rotation powered pulsars

Rotation powered pulsars are isolated, fast rotating neutron stars which releases their rotation kinetic energy as the electromagnetic emission. They place a high priority on the observation with PoGOLite. Polarimetry in the radio and optical bands revealed that the emission is from opened magnetic field lines while the mechanism of the high-energy radiation is still unknown.

There exist three competitive emission models. In *polar cap* model [35, 36], particles are accelerated near the neutron star's surface around the magnetic pole (polar cap), and the high-energy photons are emitted with curvature radiation under the strong magnetic field and inverse-Comptonization induced pair cascades. *Outer gap* model [37, 38, 39] assumes the particle acceleration in the 'vacuum gap', which evolves in the outer magnetosphere along the last open field line between the null-charge surface and the light cylinder, and high-energy radiation from photon-photon pair-creation induced cascades. *Caustic* model [40, 41] is purely geometrical one. The emission is thought to arise at the both magnetic poles while at only one pole or region for the polar cap and outer gap models.

The Crab pulsar is the primary target for PoGOLite. One pulse period includes two peaks called P1 and P2 in the X-ray and gamma-ray bands. Figure 1.5 shows results from theoretical calculations for the intensity, polarization direction and polarization degree as functions of the pulse phase. Rapid changes of polarization are predicted with two peaks of the intensity. The polarization angles and degrees significantly vary among three models for P1 while not being so different for P2. Such a phase-resolved observation with PoGOLite will clearly discriminate between the presented models [57].

Accreting black hole binaries

Every galactic black holes is supposed to be a part of a binary system, and the accreting materials from a companion star make an 'accretion disk' around the black hole, which is so hot to produce X-rays. Most of the black holes fluctuate between two states called 'hard state' and 'soft state' with dramatic changes of both of the luminosity and the spectrum. The difference of mass accretion rates result in the transitions and the accretion geometry as shown in figure 1.6.

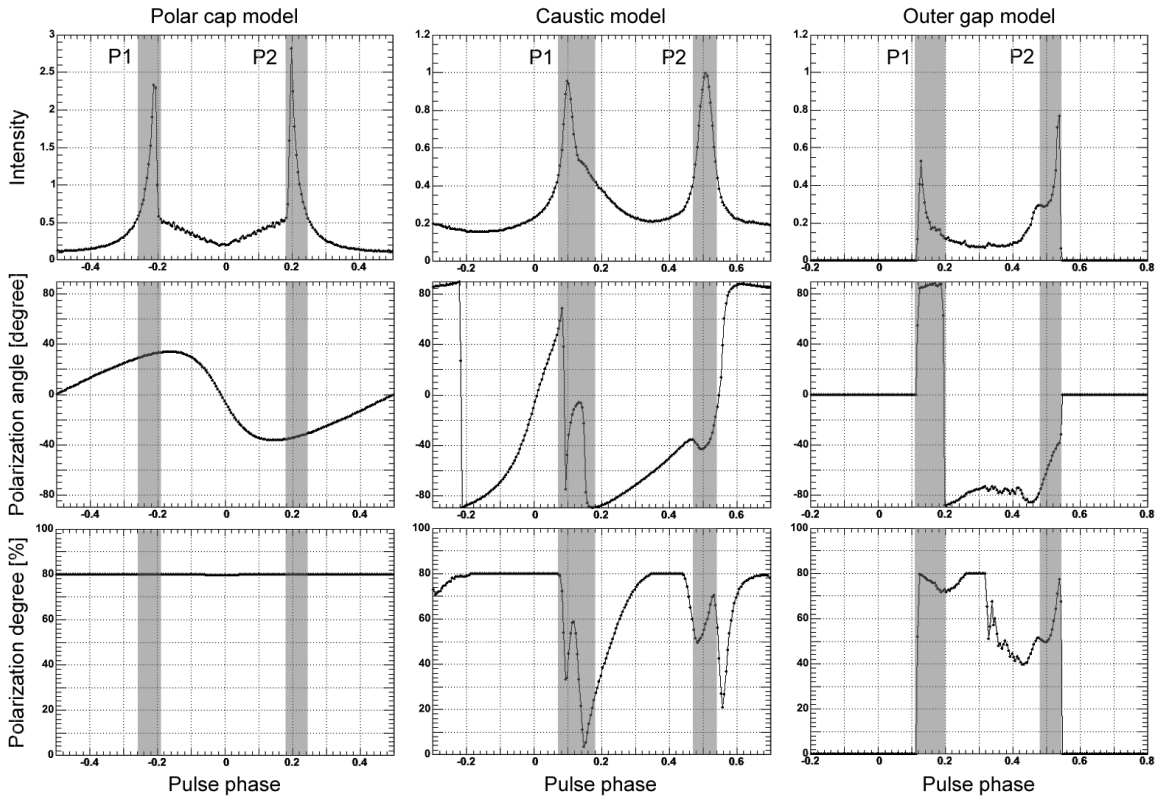

Figure 1.5: Simulation of the relative intensity (top row), polarization angle (middle row) and polarization degree (bottom row) for the three Crab pulsar models. We have the pulse phase on the horizontal axis. The polar cap (left column) and caustic (center column) models are from [40] and the outer gap model (right column) is from [38]. Numerical data are from Alice Harding.

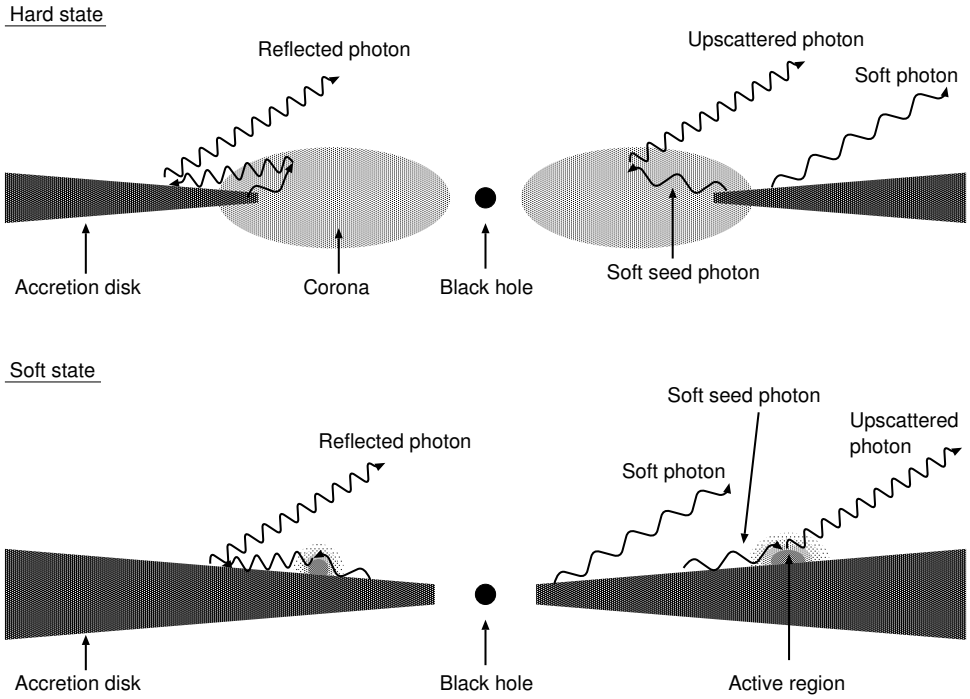

Figure 1.6: The presented accretion geometries around a black hole for the hard state (top) and the soft state (bottom). In the hard state, the optically thick accretion disk recedes from the central black hole while the disk moves inward in the soft state. Hard X-rays originate by soft 'seed photons' upscattered at the inner hot corona (hard state) or the active regions (soft state). Some of the hard photons are reflected by the disk.

In the hard state, the hard X-rays with a power-law spectrum are emitted by the thermal Comptonization of thermal low-energy photons from the disk in the inner 'corona.' Some hard X-ray photons are reflected at the outer part of the disk and come into our line of sight. Though the initial power-law component is thought to be non-polarized, the polarization parallel to the disk plane is expected for the reflection component. The polarization degree will depend on the inclination of the accretion disk [42].

The emission mechanism is not known well for the hard X-rays in the soft state. One theory holds that the thermal disk photons are scattered up by an energetic nonthermal electrons which are distributed in the 'active regions' on (or above) the disk. Like in the hard state, the disk reflects a part of hard X-rays, thus the polarization arises. Polarimetry might provide the distribution of the nonthermal electrons.

Polarization measurements, as above, will restrict the models on the accretion geometry derived by temporal and spectroscopic studies. An important target for us is Cygnus X-1, the brightest and best-studied black hole. Our simulation shows the minimum detectable polarization is 10% for both states of Cygnus X-1 [43].

Accreting pulsars with a strong magnetic field

Strongly magnetized (with the order of $10^{12} - 10^{13}$ gauss) rotating neutron stars in binary systems are believed to originate their X-ray emissions from the gravitational energy of the accreted materials. The materials flow along the magnetic field lines into the regions near the polar cap, where the X-rays and gamma-rays originate. In a strong magnetic field $\mathbf{B}$, electrons in a plasma gyrate on a plane perpendicular to $\mathbf{B}$ (cyclotron gyration) and have a larger cross section to the photons with the electric vector perpendicular to $\mathbf{B}$ (cyclotron absorption). Thus the observed X-rays and gamma-rays near the cyclotron energy can be polarized in parallel to the direction of the magnetic field lines projected onto the celestial sphere [44]. The polarization degree and angle will modulate with the pulse phase because the orientation of $\mathbf{B}$ changes. The maximum polarization arises when $\mathbf{B}$ parallels the celestial sphere.

This type of sources may serve an opportunity to study physical processes under an extreme environment, the strong magnetic field and the intense gravity with the compact mass of a neutron star. Hercules X-1 is the prime target.

1.2.3 Development progress and motivations of this study

We have completed designs and begun procurements for some components. PDCs and SASs have been evaluated their light ourput and started to be assembled. Procurement of PMT-ASSYs has been started. Their acceptance tests appear in this report. Basic

architecture of the DAQ system has been determined and the development is in progress. Prototyping of the rotation mechanism for the polarimeter and assembling of the star trackers have been started.

Since acceptance tests of the PMT-ASSYs have to be conducted after the start of the mass production, we have to develop the test items and efficient procedures of the tests.

The prototype polarimeter has been updated with the first full PDC unit. Evaluations with polarized gamma-rays from ^{241}Am source have been performed in a laboratory [45], but the detector response in the lower energy band need to be examined, too. So we have tested the prototype with a highly polarized photon beam at a synchrotron facility and compared its performance with a computer simulation.

PoGOLite will suffer high radiation background in balloon flights. The first prototype analog electronics and the PDC have enabled us to evaluate the total response of whole PDC system to the large input signals with charged particles. We have examined the response with a proton beam.

1.3 Outline

This chapter has given the background of X-ray and gamma-ray polarimetry, and overview of the PoGOLite instruments and the scientific goals.

Chapter 2 explains minimum amounts of basic knowledge on scintillators, PMTs and polarimetry. This chapter also include properties of the scintillators used in PoGOLite instruments.

In chapter 3, an overview of the PoGOLite PMT-ASSYs is presented, and their acceptance tests are performed. An average performance of the PMT-ASSYs are shown.

The 7-unit prototype polarimeter is tested with a polarized photon beam in chapter 4. Its results are quantitatively compared to a simulation using Geant4 package. The 'double integration method' for PSD is shown there.

Chapter 5 describes a proton beam test of a PDC at Research Center of Nuclear Physics in Osaka University. A radiation environment expected in the balloon flights has been simulated. A new PSD method which will simplify the readout electronics is proposed and compared with the classical method which appears in chapter 4.

Finally, conclusions and future plans are summarized in chapter 6.

Chapter 2

Theory

In this chapter, we give a minimum knowledge on scintillators, photomultipliers and polarimetry utilizing Compton scattering processes. The properties of the scintillators used in PoGOLite is also shown.

2.1 Scintillators and photomultiplier tubes

The light output of scintillators is mainly characterized with two parameters, the total number of output photons N_0 and the decay time constant τ. The number of photons emitted at the time t is approximately described with them, as

$$N(t) \;=\; \frac{N_0}{\tau} \exp\left(-\frac{t}{\tau}\right).$$

The phoswich technique is fundamentally based on the difference of the decay times between scintillators. We show the sizes and properties of the three scintillators used in the Phoswich Detector Cells as below.

The fast scintillator (EJ−204) is provided by ELJEN Technology in Texas, USA. It is processed as hexagonal rods with 2.775 cm wide and 20 cm tall. EJ−204 has a very short decay time of $\sim$ 2 ns, and is therefore referred to as 'fast' scintillator. The wavelength with the maximum emission is 408 nm.

The slow scintillator (EJ−240) is also provided by ELJEN Technology. Its shape is hexagonal tube with 60 cm long, 2.70 cm wide and the wall thickness of 2 mm. Their decay time of 285 ns is quite long for a plastic scintillator, so EJ−240 is called 'slow' scintillator. The wavelength with the maximum emission is 435 nm.

The BGO scintillator is supplied by Nikolaev Institute of Inorganic Chemistry in Novosibirsk, Russia. Since the bottom BGO scintillator of the PDC works as an active shield and a light guide for the fast and slow scintillators, it is formed of the combination

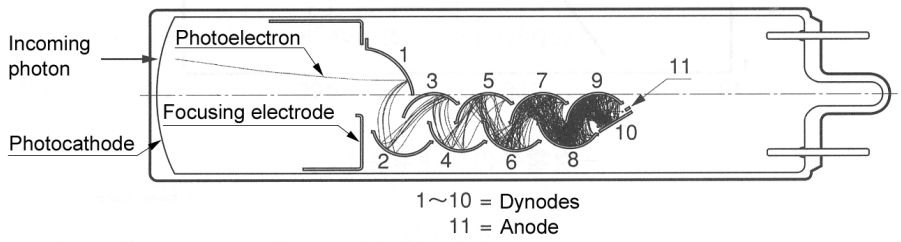

Figure 2.1: A simulation on the trajectories of electrons in a PMT [46].

of a hexagonal rod with 2.85 cm wide and a cylinder with a diameter of 2.30 cm, and the total length is 4.0 cm. The decay time is 300 ns and the wavelength with the maximum emission is 480 nm.

The scintillating photons are read by PMTs. Photons coming into a PMT are converted to photoelectrons in a *photocathode* with a ratio called *quantum efficiency* which depends on the wavelength of the light and the material of the photocathode. Then the electrons are multiplied by $\sim 10^6$ times with several *dynodes* where the stepwise voltages are applied (figure 2.1). Generally a negative high voltage of about -1000 V, called *bias voltage*, is applied to a photocathode to work a PMT. The bias voltage is divided to be put onto each dynodes by ladders of resistors called *divider circuit* or *bleeder*. A *gain* of a PMT G is given by a power-law function of the bias voltage E as

$$G \;=\; A \cdot E^{kn} \tag{2.1}$$

where A is a constant, k is a constant of $\sim 0.7{-}0.8$ (depending on the material and the structure of the dynodes) and n is the number of the dynodes. We give more detailed description of the PoGOLite PMTs in chapter 3.

The light output of the scintillators is reduced with its propagation in scintillators or light guides and the quantum efficiency of a PMT. The simplest value which we can evaluate the light yield with is the number of photoelectrons emitted from the photocathode in a PMT. We express a light yield with this 'total' output per 1 keV energy deposit, p.e./keV, where p.e. is short for photoelectrons.

The numbers of photoelectrons always fluctuate following Poisson probability distribution. If we assume the number of photoelectrons is n and the mean of the Poisson distribution is μ, the distribution is given by

$$P_P\,(n;\mu) \;=\; \frac{\mu^n}{n!}e^{-\mu}.$$

The electron multiplication takes place in a PMT following Gaussian probability distribution. Let us define n_e as the number of the output electrons from a PMT and G as the

gain of the PMT. The probability distribution of the output from the PMT is described as

$$P\left(n_e/G;\mu,\sigma\right) = \sum_{n=0}^{\infty} P_P\left(n;\mu\right) P_G\left(n_e/G;n,n\sigma\right) \tag{2.2}$$

$$= \frac{e^{-\mu}}{\sqrt{2\pi\sigma^2}} \sum_{n=1}^{\infty} \frac{\mu^n}{n\cdot n!} \exp\left(-\frac{\left(n_e/G-n\right)^2}{2\left(n\sigma\right)^2}\right) \tag{2.3}$$

where $P_G\left(x;m,s\right)$ gives Gaussian distribution with a mean m and a standard deviation s,

$$P_G\left(x;m,s\right) = \frac{1}{\sqrt{2\pi s^2}} \exp\left(-\frac{\left(x-m\right)^2}{2s^2}\right).$$

We know empirically $\sigma \sim 0.35$ for the PoGOLite PMTs. Since $n_e/G, \mu$ and σ are non-dimensional values, equation 2.3 is scalable arbitrarily, thus also gives a spectrum of mono-energetic incident photons. The light yield for the energy deposit of E [keV] is given by μ/E [p.e./keV].

2.2 X-ray/gamma-ray polarimetry utilizing Compton scattering

A *polarization direction* is defined as the direction where the amplitude of superposed electric vectors of the incident electromagnetic waves becomes maximum. A *linear polarization degree*, or simply a *polarization degree*, P is defined with the intensity parallel to polarization direction $I_\parallel$ and that for the perpendicular direction $I_\perp$, as

$$P \equiv \frac{I_\parallel - I_\perp}{I_\parallel + I_\perp}.$$

We call $P = 1$ and $P = 0$ as the full polarization and the non-polarization, respectively. Strictly the polarization is expressed with four *Stokes parameters*. A detailed description is found in [47].

Since X-rays and gamma-rays have a strong nature of particles, one cannot detect them as 'polarized waves' like in the radio and optical band. Photons with the energy of ~ 30 keV $-$ 1 MeV tend to be Compton-scattered in materials, thus it is preferable to use Compton scattering for the polarization measurement in this band. PoGOLite is categorized as this 'scatter type' polarimeter.

Klein-Nishina formula, which describes the differential scattering cross-section in the Compton scattering process, for the polarized photons is

$$\frac{d\sigma}{d\Omega} = \frac{r_0^2}{2}\frac{k^2}{k_0^2}\left(\frac{k_0}{k} + \frac{k}{k_0} - 2\sin^2\theta\cos^2\varphi\right).$$

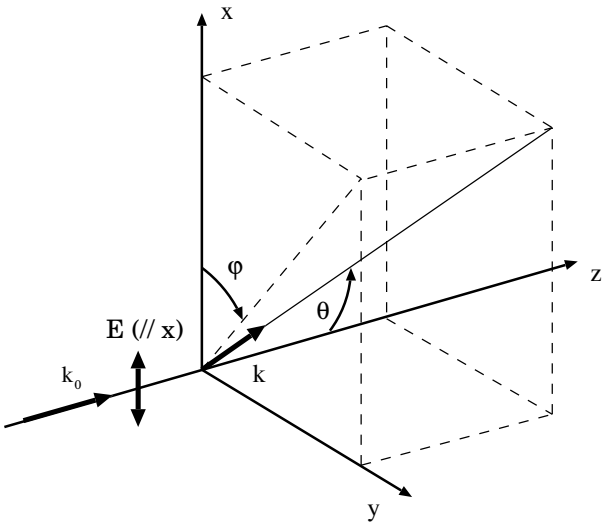

Figure 2.2: The geometry of a Compton scattering process. The electric vector, or the polarization vector, of the incident photon **E** is parallel to the x axis.

We have here r_0 as the classical electron radius, and k_0 and k as momenta of the incident and scattered photons, respectively. θ and φ are respectively the polar and azimuth scatter angles from the incident photon's electric vector, or the polarization vector. The geometry of the scattering is shown in figure 2.2. This formula is also expressed with the energy of the incident photon, E_0, as

$$\frac{d\sigma}{d\Omega} = \frac{r_0^2 \varepsilon^2}{2}\left(\frac{1}{\varepsilon} + \varepsilon - 2\sin^2\theta\cos^2\varphi\right), \tag{2.4}$$

where

$$\varepsilon = \frac{1}{1 + \frac{E_0}{m_e c^2}(1 - \cos\theta)}$$

and $m_e c^2$ is the electron rest mass (511 keV).

When E_0 and θ are fixed, equation 2.4 can be written as

$$\frac{d\sigma}{d\Omega} = A - B\cos 2\varphi,$$

where A and B are constants with a relation of $A > B$. This function reaches maximum at $\varphi = 90°$ and 270°. In other words, photons tend to be scattered at right angles to the initial polarization vector. This is known as the azimuthal anisotropy in Compton scattering.

Let us consider that a detector with a finite volume detects the scattered photons. The number of detected photons modulates with φ following equation 2.2. For a general description, φ is replaced with $(\varphi - \delta)$, and we obtain

$$N(\varphi) = A - B\cos 2(\varphi - \delta).$$

When we assume $N_{\max}$ and $N_{\min}$ are the number of the maximum and minimum counts of the photons, a *modulation factor* of a polarimeter is defined as

$$M \equiv \frac{N_{\max} - N_{\min}}{N_{\max} + N_{\min}}.$$

therefore we obtain

$$M = \frac{(A+B)-(A-B)}{(A+B)+(A-B)} = \frac{B}{A}.$$

When the incident photons are not fully polarized, this value is called as the *observed modulation factor* and denoted by $M_{\rm obs}$. On the other hand, M_{100} especially represents the modulation factor for the full polarization. There is a relationship between $M_{\rm obs}$ and M_{100} as

$$M_{\rm obs} = M_{100} P.$$

Therefore, the incident polarization can be determined by

$$P = \frac{M_{\rm obs}}{M_{100}}$$

if we know the polarimeter's response, M_{100}.

Chapter 3

Acceptance tests of the flight-model photomultiplier tube assemblies

In this chapter, we describe acceptance tests of the flight-model PMT-ASSYs (photomultiplier tube assemblies) which were developed for the PoGOLite project.

3.1 Overview of the photomultiplier tube assemblies for PoGOLite

3.1.1 Requirements for the photomultiplier tubes

There have been some requirements specific to the PMTs for PoGOLite, as listed below.

- Size: The size of the PDCs (Phoswich Detector Cells) was optimized by detailed simulations. The width of the bottom BGO scintillator was derived as $\sim$ 3 cm, which allowed the PMT with a 1 inch diameter.
- Quantum efficiency: The light output from the scintillators and the quantum efficiency of the PMTs affect critically to the sensitivity of PoGOLite because only a few keV is deposited when a low-energy photon is Compton-scattered. A larger quantum efficiency is of course better. Because the wavelength of the maximum emission of the fast scintillator is 408 nm, a bi-alkali photocathode, which has a maximum quantum efficiency at $\sim$ 390 nm, is suitable.
- Gain: We have to read out signals of one p.e. level, which is expected in the energy depositions of $\sim$ 1 keV. The gain of the PMT should be as large as possible in order to separate these signals from the noise.

- Noise: Noise must be as low as possible to read one p.e. signals.

- Magnetic field shielding: Since trajectories of the electrons are distorted, a PMT gain is generally very sensitive to a magnetic field, even to the earth magnetism of the order of 10^{-1} gauss. The magnetic field must be shielded by metals with high permeability, called μ metals.

- Power consumption: The lower power consumption is better for balloon experiments since the power is supplied from batteries. Generally, a PMT uses a large power of ~ 1 W. PoGOLite uses 271 PMTs, thus PMTs are supposed to account for a large part of the total power consumption. The weight of the batteries, which reflects the power consumption, shares responsibility to lower the balloon flight altitude. It is important to reduce the power consumption of the PMTs for lightening the payload.

- Discharge: The ambient pressure is ~ 1 mmHg at the balloon altitude, where the discharge occurs very often. Though a pressure vessel will be used to envelope the whole detector, more conservative design requires measures to discharge for each PMT-ASSYs.

- Radiation environment: Cosmic-ray protons, electrons and positrons deposit the energy of 10 keV $-$ 1 MeV in a PDC at a rate of ~ 350 Hz. These background events make the non-negligible anode current compared to the bleeder current, which increases the gain of the PMT. For the large output signals from the PMTs, it typically takes ~ 1 ms to recover. This makes a very long dead time of $\sim 30\%$ and enormously reduces the sensitivity in the observation. Problems of large deadtime caused by particles have been reported from detectors on earlier satellites such as HEXTE aboard RXTE [48, 49]. Therefore, we have to develop a new bleeder that realizes short recovery time.

- Thermal environment: The ambient temperature changes with the altitude as shown in figure 3.1. Though we have not finished the detailed thermal design of the detector system, $> -1°$C/min is expected during the ascent of the balloon thanks to a large heat capacitance. The temperature goes down to ~ 250 K at the level flight altitude of 40 km but the actual temperature of the PMTs will be slightly higher than 250 K due to the heat generation from themselves. Our PMTs have to be tolerant of the rapid changing of the temperature and to work in the cool environment.

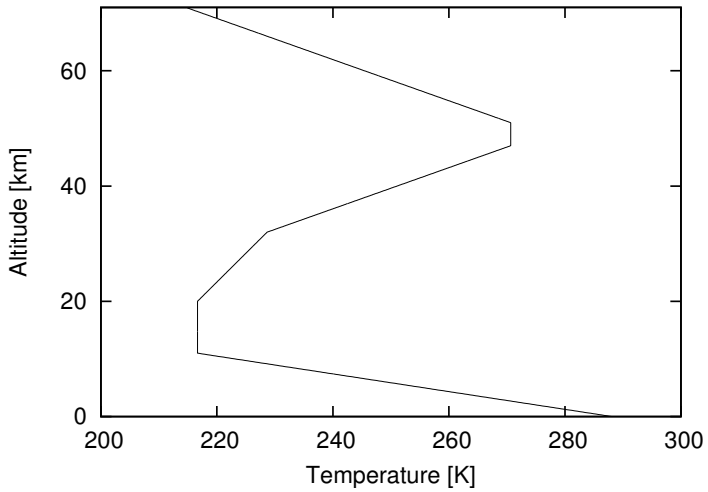

Figure 3.1: Changes of the atmospheric temperature with the altitude, from US Standard Atmosphere, 1976 [50]. About 250 K is expected as the ambient temperature at the altitude of $\sim$ 40 km.

3.1.2 Features of the flight-model photomultiplier assemblies

We developed PoGOLite flight-motel PMT-ASSYs (R7899EGKNP) satisfying the requirements with Hamamatsu Photonics K.K. The R7899 PMT which has a 1 inch diameter and a bi-alkali photocathode was selected. A PMT, a bleeder circuit and a high voltage unit are built in a cylindrical μ metal case. The photocathode of the PMT is placed at 1 cm deep from the end of the metal case in order to shield the magnetic field effectively. The photocathode is grounded in order to prevent the discharge from cathode to the case, scintillator and the air. The high voltage unit needs a +12 V power supply and a positive reference voltage of 0$-$5 V. The reference voltage is boosted by 250 times with a DC to DC converter inside the PMT-ASSY. Thus we can apply 0$-$1250 V to the PMT. The low voltages of +12 V and +5 V are never discharge, while the ordinal high voltage supplies from external power units require coating cables to avoid the discharge from cracks on them.

The bleeder circuit was designed with the techniques against large pulses adopted in the PMTs of Suzaku/HXD [25]. The circuit diagram is shown in figure 3.2. The 1 MΩ resistance ladder divides the bias voltage of +1100 V (typical) from the high voltage module, C4900-51MOD, thus the bleeder current of $\sim$ 80 μA is expected. The maximum output current of the original C4900-51 is 0.5 mA, which is over-spec for us. Since the power consumption was able to be reduced by limiting the maximum output current, C4900-51 was modified for our PMT-ASSYs.

There are some components in the bleeder to reduce the effects of the large signals.

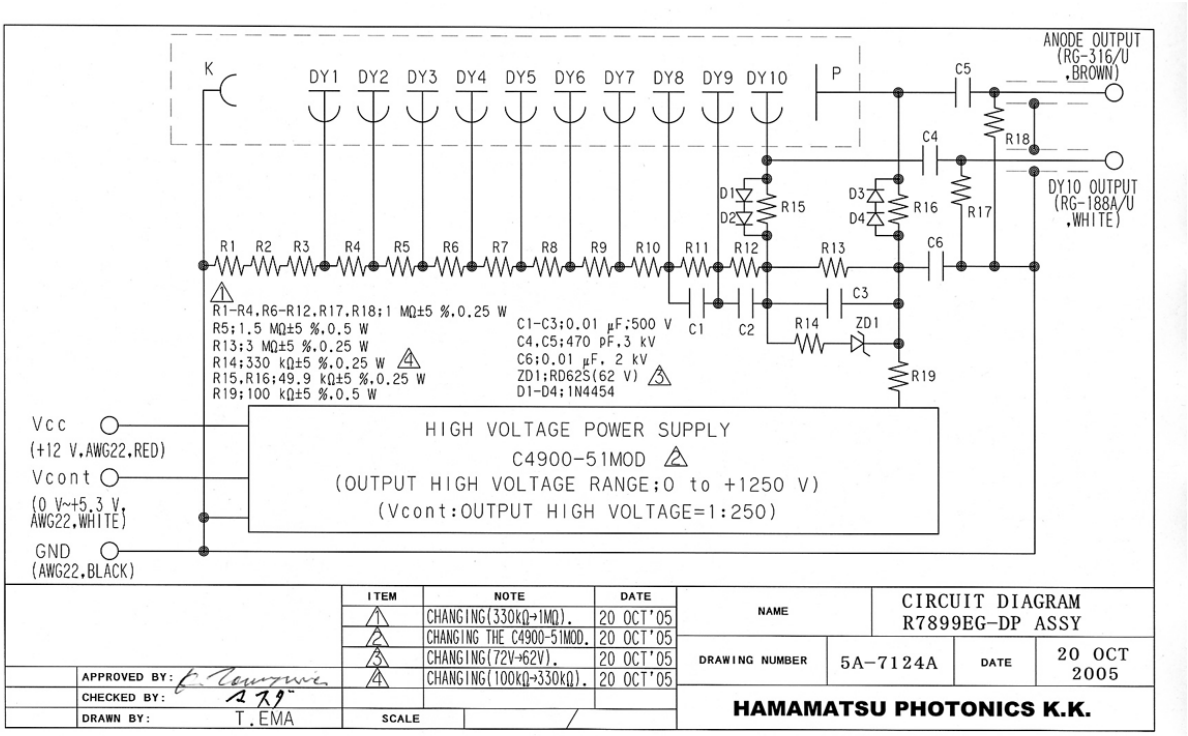

Figure 3.2: The bleeder circuit diagram of the PMT-ASSYs for PoGOLite.

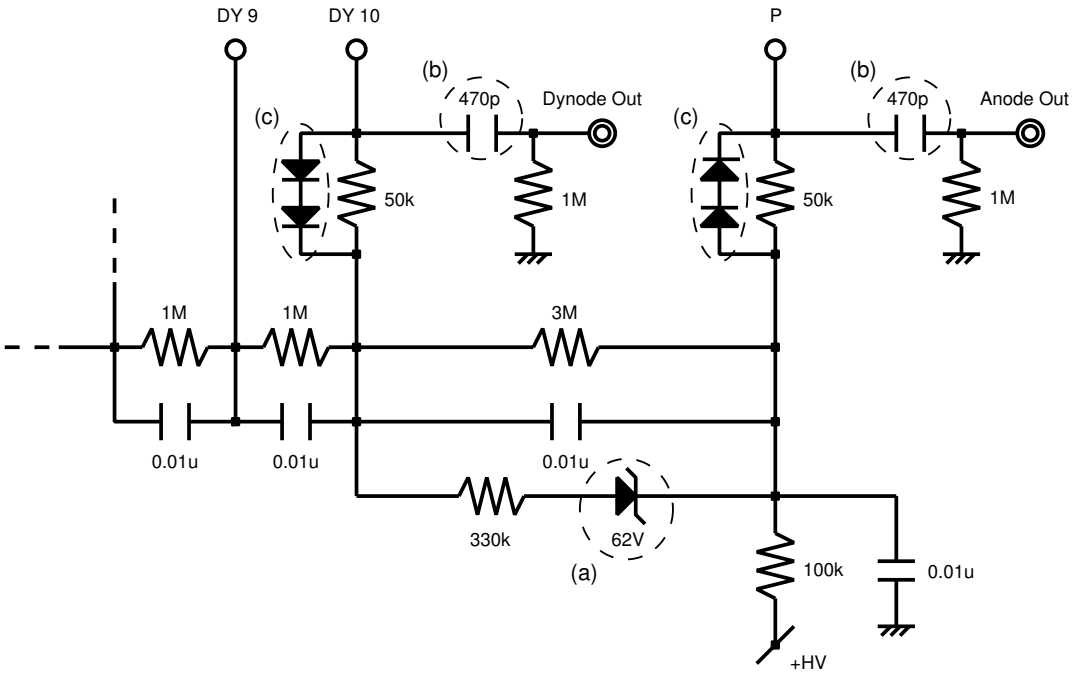

Figure 3.3: The measures to the large signal current in the last stages of the bleeder. (a) A zener diode as a voltage stabilizer, (b) small capacitance of the coupling condensers and (c) cramping diodes.

Figure 3.3 shows the last part of the divider circuit. A zener diode (a) stabilizes the applied voltage between DY 9 and DY 10 and realizes a smaller shift of the total gain even under the large anode current. However, a zener diode commonly makes large white noises. A serial resistor and a parallel capacitor compose a filter for the noise, the resistance value is optimized to minimize the noise. Though AC coupling capacitors (b) is essential to work the cathode-grounded type PMTs, they make the large time constant in the recovery from the large pulses. Since the resistances are fixed with 1 MΩ, we use the capacitance as small as possible. In addition, cramping diodes (c) are mounted in parallel with resistors which prevent a signal current escaping to the resistor ladder. The diodes let charges flow into the ladder when the voltage drop with the 50 kΩ resistance becomes larger than 1.4 V. This corresponds to the energy deposit of 2.7 MeV in the fast scintillator if we assume the light yield is 0.5 p.e./keV and the gain of the PMT is 3×10^6.

These features make our PMTs very suitable for our experiments.

3.2 Preparation experiments concerning a warm-up

Before the acceptance test, we found the noise of the PMTs continuously decreasing with time after the high voltage was supplied [58]. In general, a warm-up for several tens of minutes is recommended when the stability of a few percent is needed [46]. Thus we first measured how long does it take for the noise to settle.

A flight-model PMT-ASSY was placed in a thermostatic bath which kept the temperature at +25°C. No scintillator was mounted on the PMT. The PMT was in the thermostatic bath, or extremely dark environment, over a day before the measurement. Therefore, the fluorescent light from the glass of the PMT was negligible.

The DAQ system is shown in figure 3.4. The PMT anode output was amplified by a current amplifier by 30 times and fed into a discriminator with a lower threshold level of ~ 0.7 photoelectrons. Signals of interrupt register, gate and sample hold were created from the discriminator output. The interrupt resister signal triggered the system, and a Linux machine subsequently read the ADC (Clear Pulse 1113A) via VME. Next signal was inhibited until a DAQ cycle ended. The Linux machine added a time information to each events. The dead time was measured with the coincidence of the veto signals and 1 MHz clock signals. The number of the clocks and the coincidence signals were monitored with a visual scaler. The last dynode output of the PMT was fed into a CSA (Clear Pulse 595H) with the feedback capacitance and resistance of 50 pF and 100 kΩ, respectively. The CSA output was fed into a shaping amplifier (ORTEC 571) with a time constant of 0.5 μs, then its output was read by the ADC.

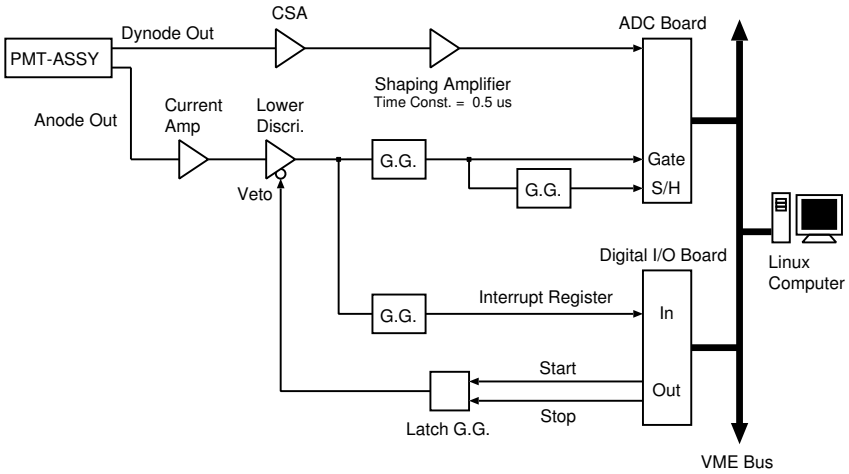

Figure 3.4: The DAQ system used in the preparation experiment. 'G.G.' is a gate generator and 'S/H' means the input of the sample hold signals.

We performed four set of 2-hour measurements with having 1-hour rests between each measurements. The high voltage was increased from zero to +1100 V in 1 minute before each measurements started. We turned off the high voltage during the rests.

We counted the number of events in the region of 2−9 p.e. as the noise for each measurements. We examined the changes of the dead-time-corrected event rate with time in the region. The results are shown in figure 3.5. The dashed lines represent the averages of the event rates in 60−120 min as the supposed constant levels. Clear decreasing trends of the noise can be seen in all of the measurements. These results clarified that the PMTs have to be warmed up at least 60 min before delicate experiments, especially the spectroscopy of a few p.e. level. We also confirmed the output waveforms after the 60-min warm-up did not change those during the warm-up. Thus the warm-up is not necessary when we only observe waveforms.

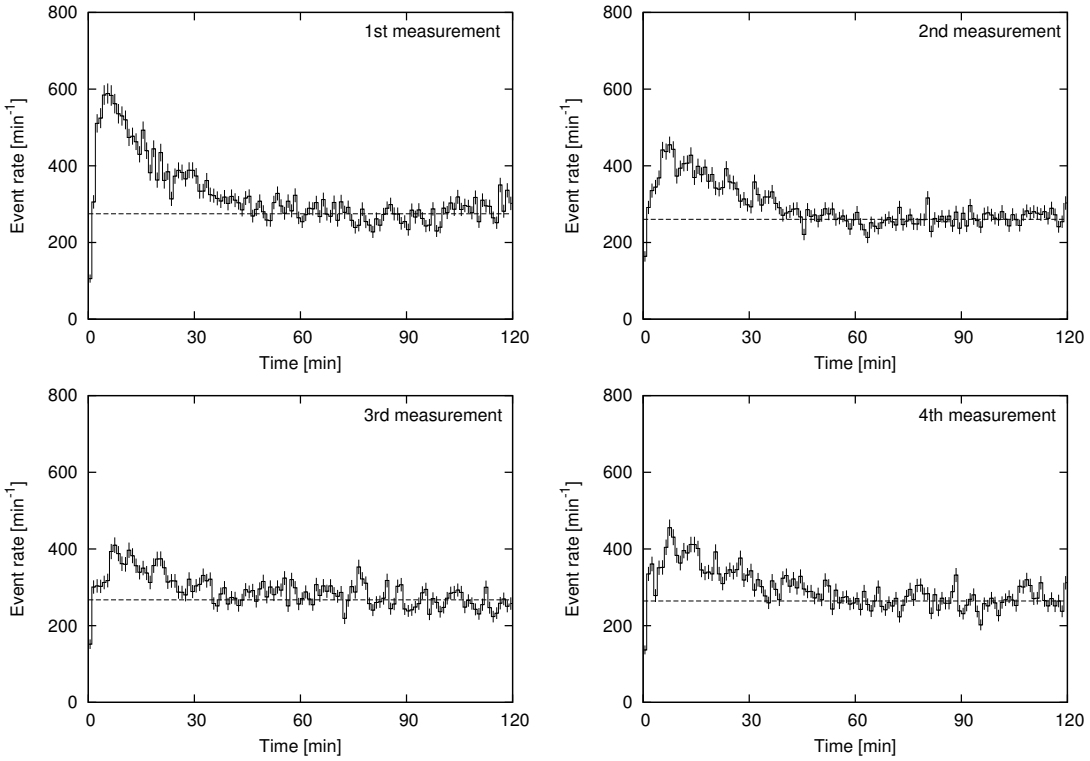

Figure 3.5: Changes of the noise with time in the region of 2−9 photoelectrons. The dashed lines represent the averages of the event rates in 60−120 min as the supposed constant levels. We can see clear decreasing trends and the noise seems to settle within 60 minutes.

3.3 Experiments

All PMTs have to be checked by ourselves. However, our time is limited, the PMTs are too many to be examined about all kinds of the test items we can do. Therefore, we should efficiently perform several tests including crucial ones as the acceptance tests. Some part of the PMTs will be examined in detail on the items omitted in the acceptance tests.

The crucial items which essentially concern the proper operation are the noise, the diode cramp and the tolerance to the low temperature. We also need the information on the bias voltage dependency on the gain for the calibration. In addition, we considered other items we were able to check along the items listed above with a small loss of time. They are the power consumption, the tolerance to the temperature changing.

In order to perform the measurements efficiently in parallel, similar measurements are gathered. We composed three measurement procedures as below.

- **Checking waveforms.** We examine the waveforms of the noise and the diode cramping in this test. Apply a bias voltage of +1100 V. Monitor one p.e. signals from the anode and the last dynode output with an oscilloscope and record typical waveforms. Feed the anode and the last dynode output into a CSA (Clear Pulse 506E with a 50 pF feedback capacitance and a 100 kΩ feedback resistance). Monitor its output waveforms corresponding to one p.e. signals and record typical ones. In addition, irradiate the PMT with a green LED ($\lambda \sim 525$ nm). Its electronics are shown in figure 3.6. Record the anode and last dynode output and the waveforms fed into the LED, without attenuation at first. Repeat it with an input signal attenuated by 13 dB.

- **Bias voltage dependence.** Acquire ^{55}Fe spectra and record power consumptions with various bias voltages, from +1250 V to +800 V with 50 V steps. Figure 3.7 shows the DAQ system. Mount a cylindrical plastic scintillator (1 inch diameter and 2 cm thick) on the PMT with some optical grease. Apply a bias voltage of +1250 V for more than an hour before the first measurement. Acquire a spectrum with a 200 s exposure. After that, record the power consumption. Since most of the current passes on the +12 V line of the high voltage module, we only have to take care of the output current in the +12 V line from the external power supply. Repeat the same measurements at the lower bias voltages.

- **One p.e. spectrum.** We examine the operation with the low temperatures, tolerance to the temperature changing and the noise level. Acquire one p.e. spectra under low temperatures and spectra of one p.e. with test pulses at +30°C. The

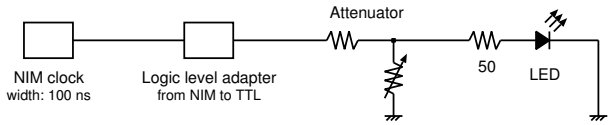

Figure 3.6: The electronics illuminating the LED. The width of the output pulse from the NIM clock generator is 100 ns. The NIM signals are converted to the TTL level, and attenuated.

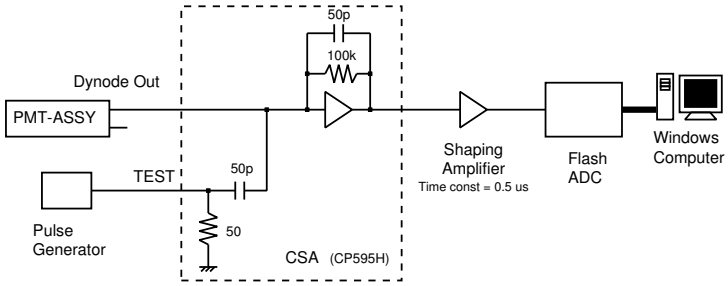

Figure 3.7: The DAQ system for the spectroscopy of ^{55}Fe and one p.e. with test pulses. A high-pass filter at the TEST input of the CSA differentiates rectangular waves from a pulse generator. Test pulses are not generated for the ^{55}Fe measurements. We do not use the anode output of the PMT in this setup.

DAQ system is same as that of figure 3.7. Because it takes whole a day to perform this experiment, deal with five PMTs at a time. Put the PMTs in a thermostatic bath. Apply a bias voltage of +1100 V. Start the thermostatic bath and check if the vibration noise makes the electrical noise on the PMT readout. Change the temperature as shown in figure 3.8. The temperature changing rate of ± 0.5°C/min is generally allowed for PMTs although we do not know whether this is sufficient or not for the balloon flight. Acquire one p.e. spectra of each PMTs at $-30, -15$ and 0 °C with 300 s exposures. Since it takes about an hour for the heat to diffuse over the PMT, wait for an hour before the measurements. Acquire a spectrum of one p.e. with the test pulses with a 300 s exposure at +30°C. Take the PMTs from the thermostatic bath and check if the PMTs do not crack.

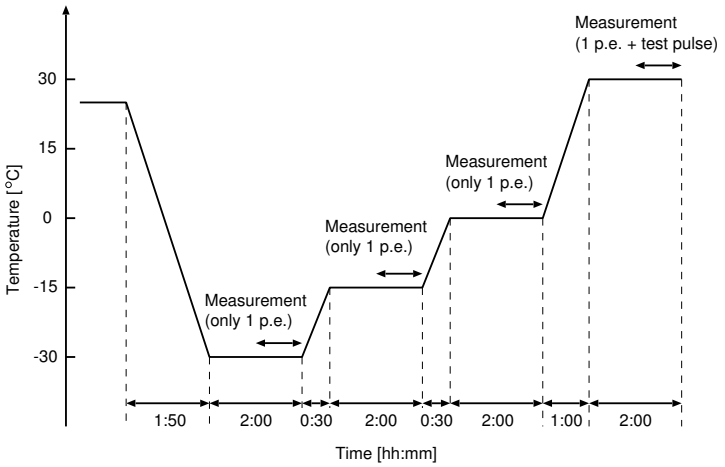

Figure 3.8: The setup of the thermostatic bath for the temperature test. Since it takes about an hour for the heat to diffuse over the PMT, we wait for an hour before the measurements. The temperature changing rate is ± 0.5°C/min, which is generally allowed for PMTs.

3.4 Results and discussions

We have already tested 53 PMTs. Among them, four irregular or problematic ones were found. We show the specs of the normal PMTs at first, then describe the problems.

3.4.1 Specs of the normal photomultiplier tube assemblies

Bias voltage dependency on the gain

The photo-ionization peaks of 5.9 keV X-rays were fitted with equation 2.3 for each measurements. The peak ADC channels were corrected with the gain of the shaper. Spectra with two PMTs (ZL5959 and ZL6451) were not be able to be fitted well, we show their problems later. Figure 3.9 shows examples of the bias voltage dependency on the gain. The value of the vertical axis is the corrected peak ADC channel. The dependence generally can be expressed by power-law function (equation 2.1). The lines in figure 3.9 represent the fitted functions. We used data points between +950 V and +1250 V for the fitting because there were systematic deviations for the points of the lowest voltages as clearly shown in figure 3.9.

Figure 3.10 left shows the distributions of the relative gain of the last dynode at +1100 V. They are normalized with the mean of the peak ADC channels. The distribution is within a factor of ~ 3. The distribution of the index number of the bias voltages are shown in figure 3.10 right. A concentration around the mean value of 7.63 appears. This concentration makes the gain controlling easy. For example, when the bias voltage is

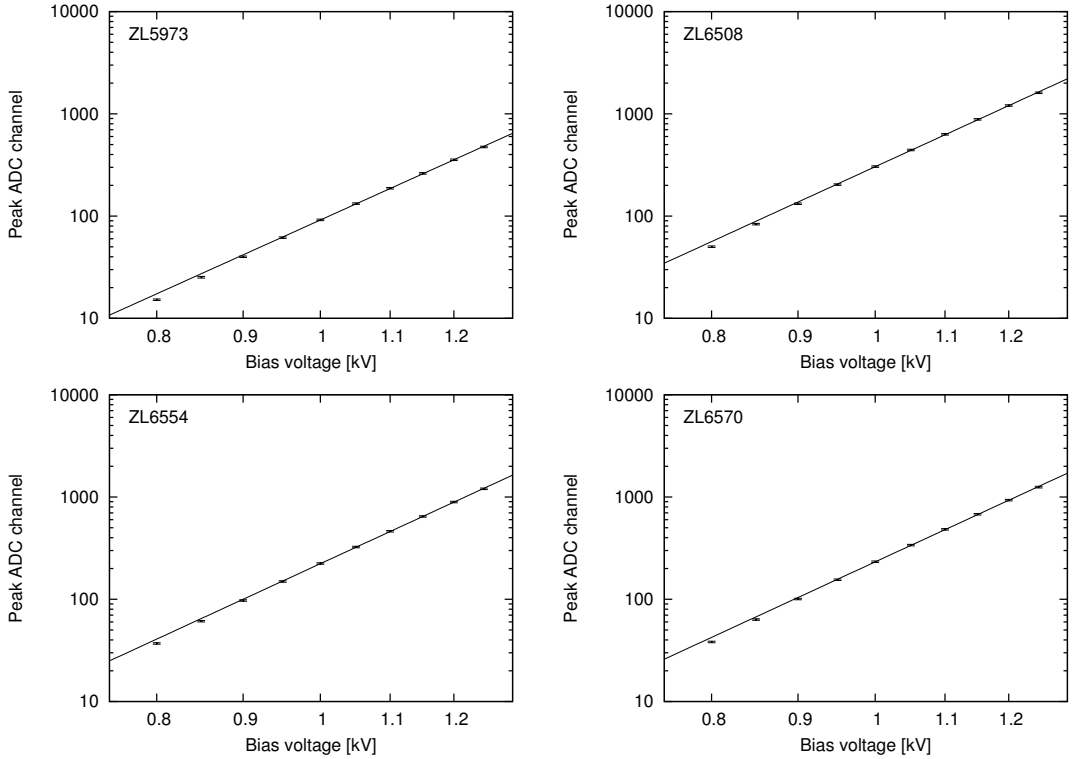

Figure 3.9: Examples of the bias voltage dependency on the gain. Voltages between +950 V and +1250 V are used for the fitting.

changed from +1100 V to +1250 V, the ratio of the gain differs by only 2.5 % between the cases with the index number of 7.8 and 7.6.[1]

We discuss whether the variety of the gain can be canceled out or not by the bias voltages. We assume +1100 V is the standard bias voltage and all of the index numbers of the bias voltage are 7.63. When we want to lower the relative gain by half (from 2.0 to 1.0 in figure 3.10 left), the bias voltage is derived as

$$\left(\frac{V}{1100}\right)^{7.63} = \frac{1}{2}, \quad V = 1004\text{V}.$$

On the other hand,

$$\left(\frac{V}{1100}\right)^{7.63} = 3, \quad V = 1270\text{V}$$

is required for increasing the gain by 3 times. Though we cannot apply the voltage above +1250 V, this is acceptable because it is not necessary that the difference of the gain is completely canceled out.

The gain is proportional to the value of S_p / S_k × S_{kb}, where S_p is an anode lumen sensitivity, S_k is a cathode lumen sensitivity, and S_{kb} is a cathode sensitivity index to

[1] $(1250/1100)^{7.8-7.6} = 1.025$

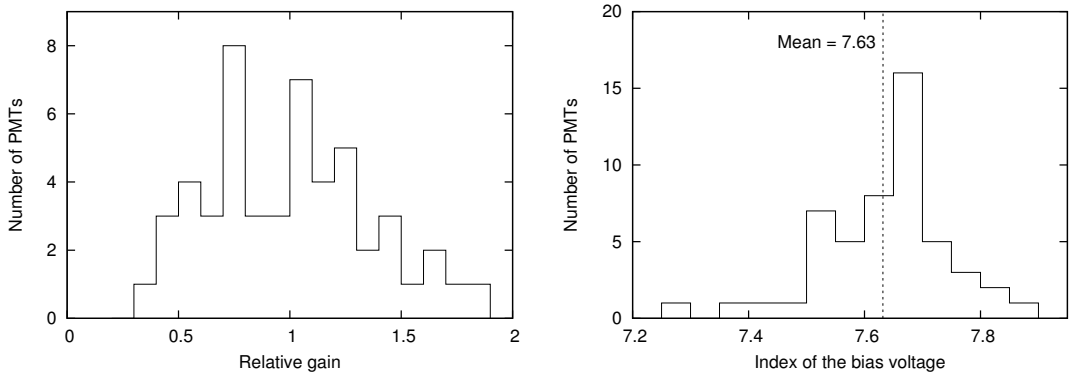

Figure 3.10: Left: The distribution of the relative gain of the last dynode at +1100 V for 51 PMTs. The relative gain is normalized with the mean of the peak ADC channels. Right: The distribution of the index number of the bias voltage for 51 PMTs. The mean is 7.63.

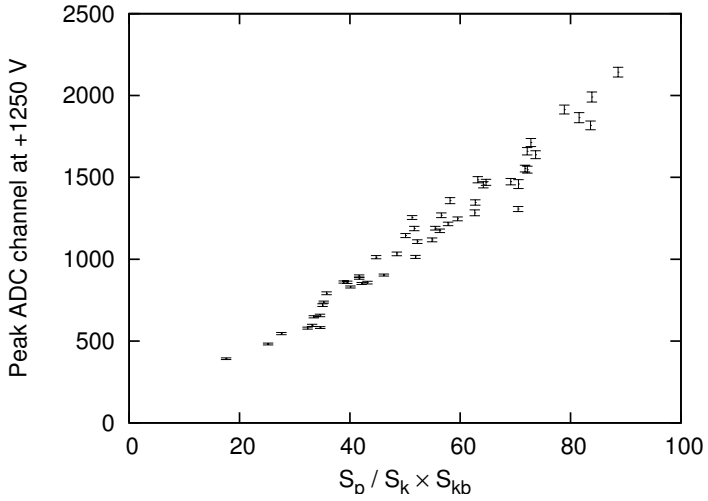

Figure 3.11: The relationship between S_p / S_k × S_{kb} and the peak ADC channel of the last dynode at +1250 V. A strong correlation shows that the measured gain can be reproduced by the values on the spec sheet.

the blue light. They appear in the spec sheets. Since S_{kb} is represented in the arbitrary unit, we cannot derive the gain from these values directly. We examined the relationship between S_p / S_k × S_{kb} and the relative gain of the last dynode. The resultant plot in figure 3.11 shows a strong correlation, which represents that the measured gains can be reproduced from the values in the spec sheets. Thus there is no defective.

Power consumption

Figure 3.12 shows the distribution of the power consumption at the bias voltage of +1100 V. Most of the PMTs fall into 246−270 mW, only 5 PMTs have larger power

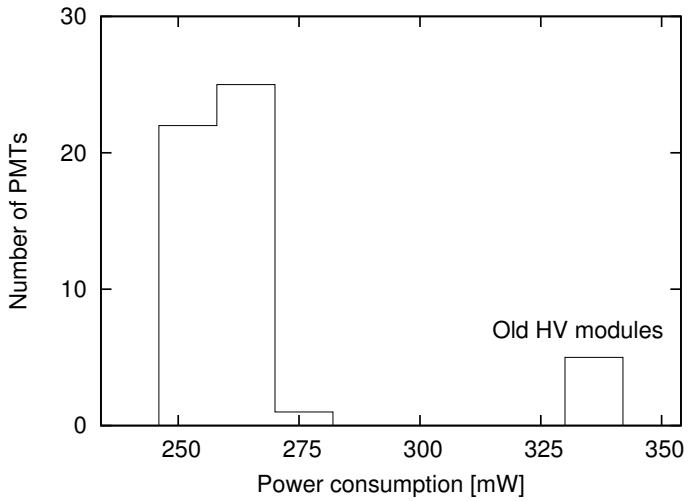

Figure 3.12: The distribution of the power consumption at the bias voltage of +1100 V for 53 PMT-ASSYs. Most of the PMT-ASSYs fall into 246−270 mW, but only 5 PMT-ASSYs have larger power consumption, $\sim$ 336 mW. They have old high voltage modules.

consumption, $\sim$ 336 mW. They are the first products which are assembled with the high voltage modules of the earlier version. All of the newer PMT-ASSYs have the power consumption between 246−270 mW, there seems to be no defectives. The total power consumption will be 70 W with 271 PMTs if we assume that all PMTs use the modified high voltage modules and be operated with the bias voltage of +1100 V.

Diode cramp

Figure 3.13 shows examples of the waveforms fed into the LED and the output waveforms from the PMTs. The output current is cramped quickly for the LED input without attenuation. When the input light gets fainter, it takes longer for the output current to be cramped. Since all PMTs behave like this way, we have no PMT-ASSYs with problematic bleeder circuits.

In this experiment, we examined only whether the diode cramp worked or not in this experiment. A detailed study on the response to the large input signals is described in chapter 5.

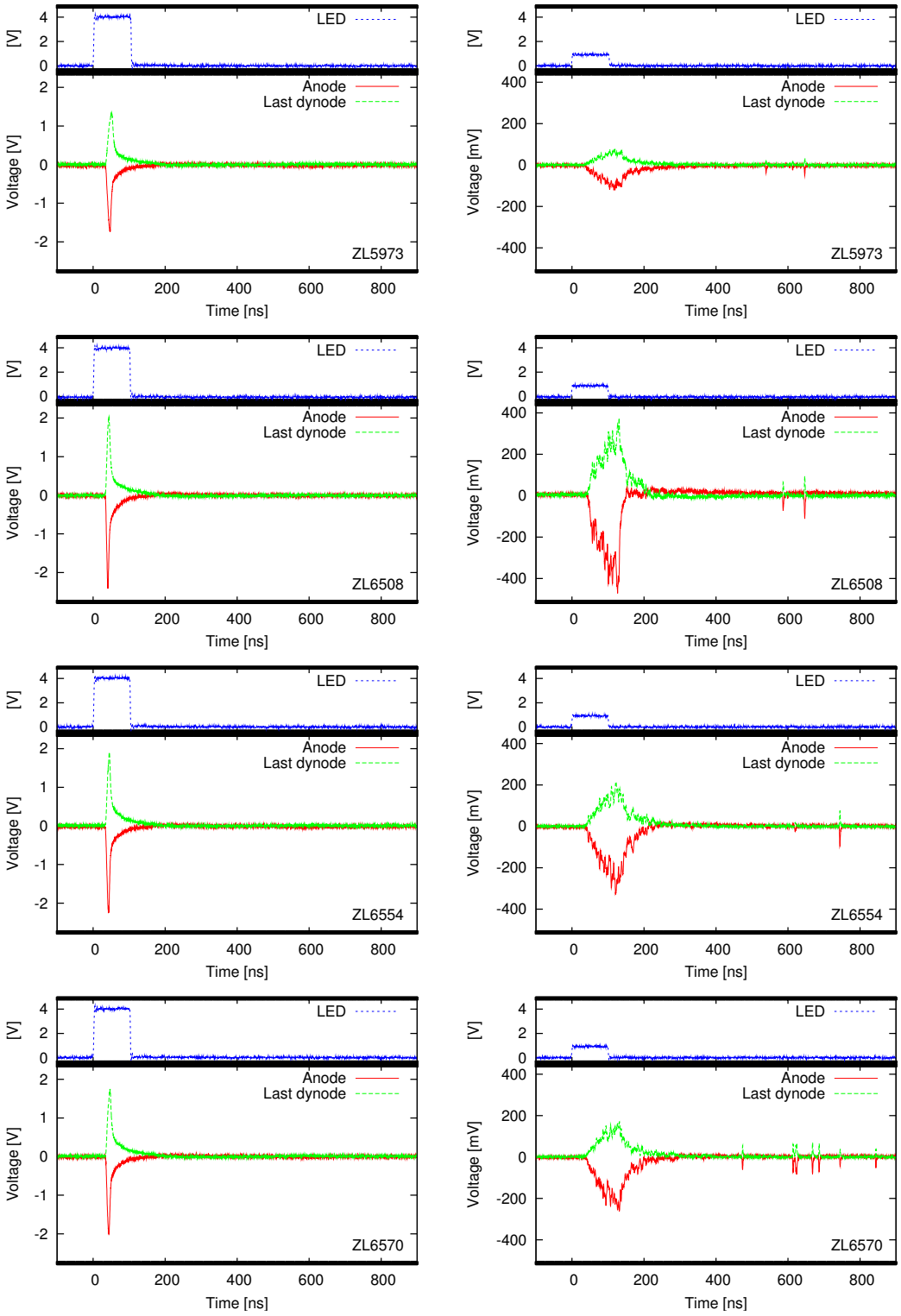

Figure 3.13: Examples of the waveforms fed into the LED (blue) and the output waveforms from the PMTs (red and green). The diode cramp works quickly for the LED input without attenuation (left column). When the LED light is fainter, the output current is cramped only slightly (right column).

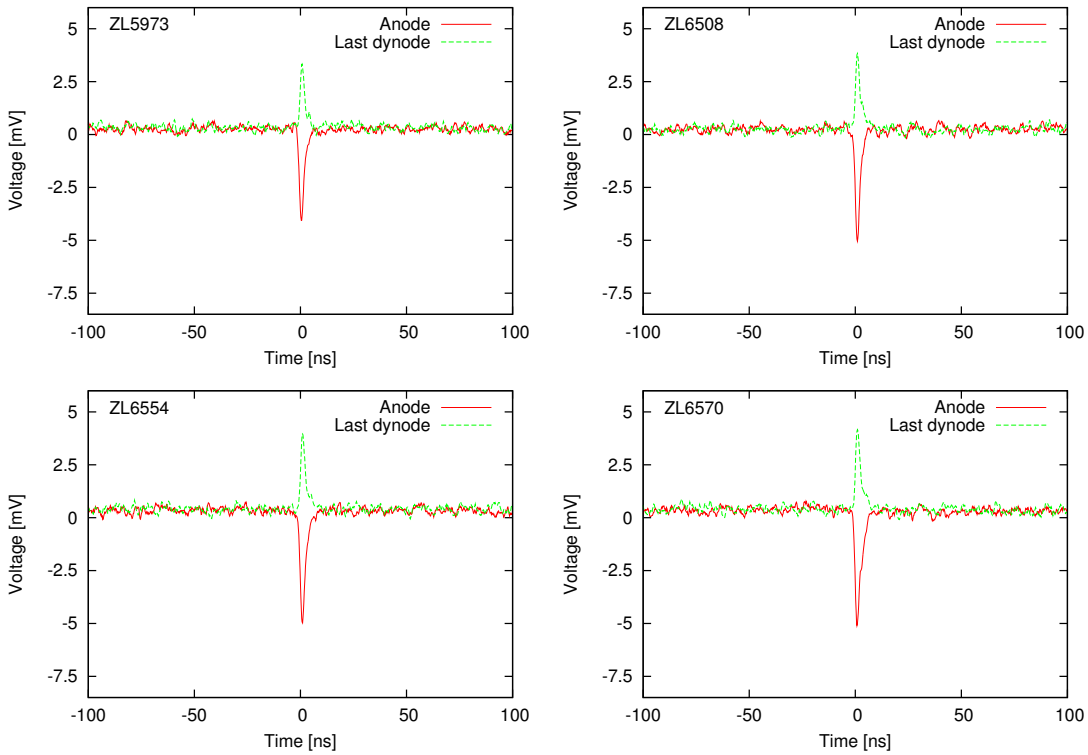

Figure 3.14: Examples of the one p.e. waveforms from the PMTs' anode and last dynode with the bias voltages of +1100 V. Noise level is $V_{\text{p-p}} < 1$ mV, which is much lower than the one p.e. signals.

Noise

The noise is smaller than the one p.e. signals in the waveform checking. Figures 3.14 and 3.15 show examples of the one p.e. waveforms from the PMTs and from the CSA, respectively, with the bias voltage of +1100 V. Also in the spectra, the one p.e. events can be distinguished from the noise. Examples of the one p.e. and test pulse spectra are shown in figure 3.16.

The width of the test pulse peak in the spectrum represents the baseline fluctuation, that is, the noise level. We made a histogram of the FWHM (full width at half maximum) of the test pulse peaks as shown in figure 3.17. The width was measured with the eye because the peaks were not always able to be be fitted with Gaussian functions. As a guide, the width of 6.5 corresponds to 0.025 p.e. for the PMT with the typical gain while the width does not depend on the PMT's gain. All PMTs have so small noise that the one p.e. signals can be read. We find out the PMTs with the older high voltage modules have slightly large noise, which are shown with a thick line in figure 3.17. We suppose these modules should be replaced.

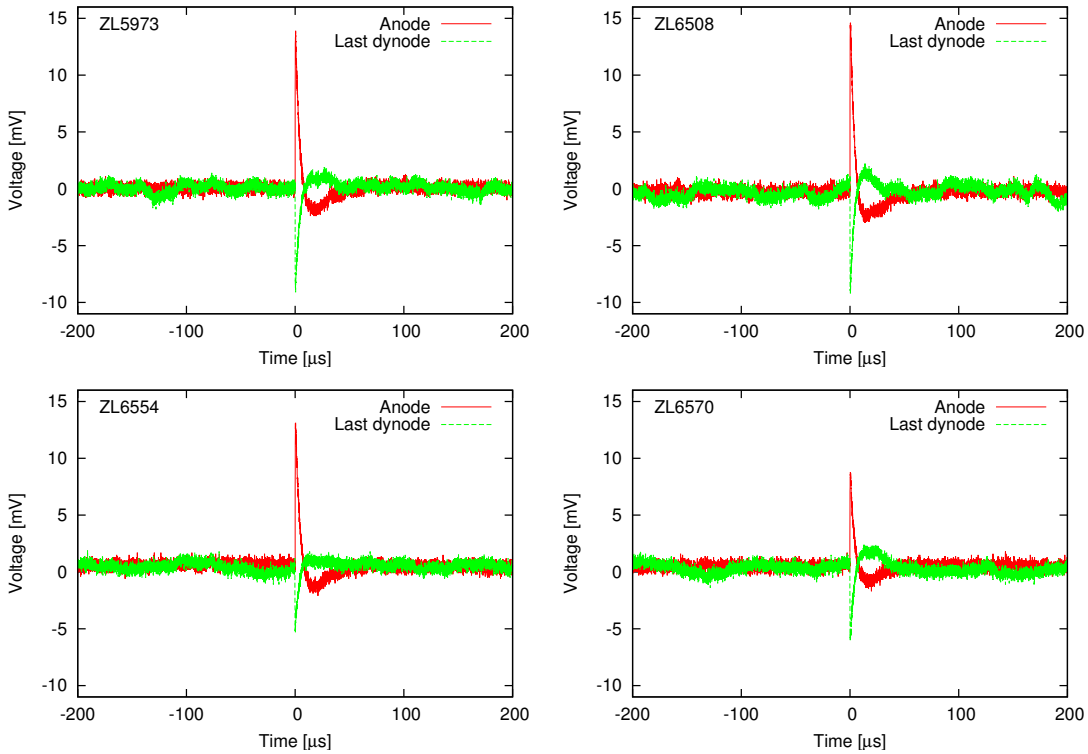

Figure 3.15: Examples of the one p.e. waveforms from the CSA with the bias voltage of +1100 V. Different events are recorded for the anode and last dynode system because the CSA has only one input. Noise level is $V_{\text{p-p}} < 2$ mV for the last dynode.

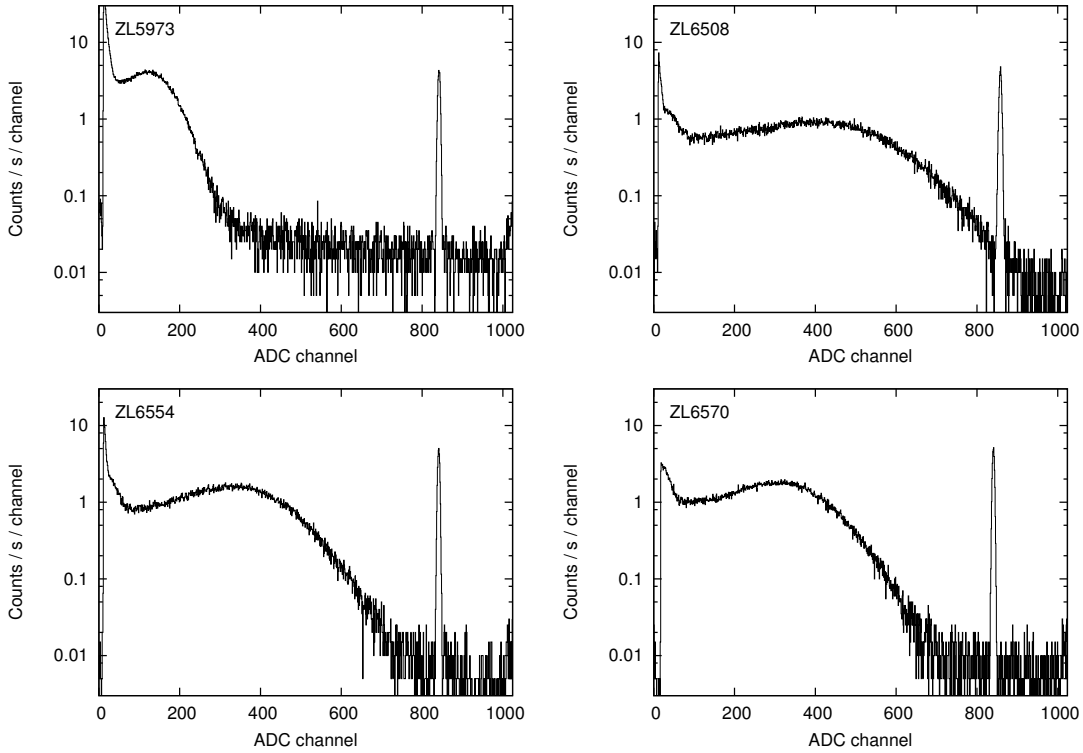

Figure 3.16: Examples of the one p.e. and test pulse spectra with the bias voltages of +1100 V. Exposure time is 200 s. The rightmost narrow peak corresponds to the test pulse signals, and the broad bump on the left side is one p.e. events. We can see the one p.e. signals can be separated from the noise.

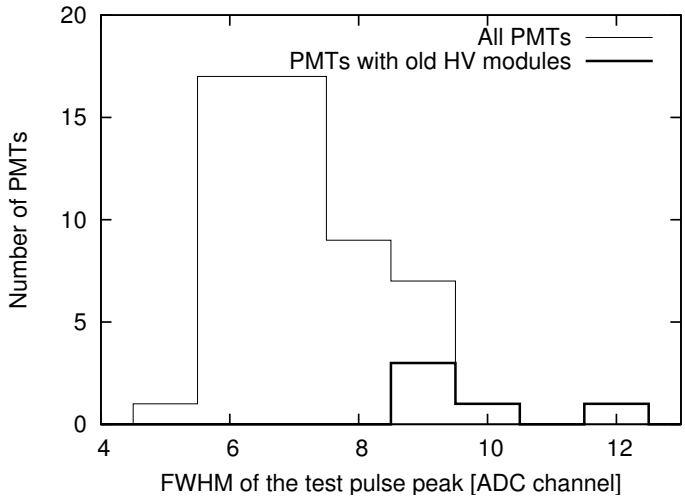

Figure 3.17: The distribution of the FWHM of the test pulse peak. The width of 6.5 corresponds to 0.025 p.e. for the PMT with the typical gain. The PMT with the old high voltage module tends to have large noise.

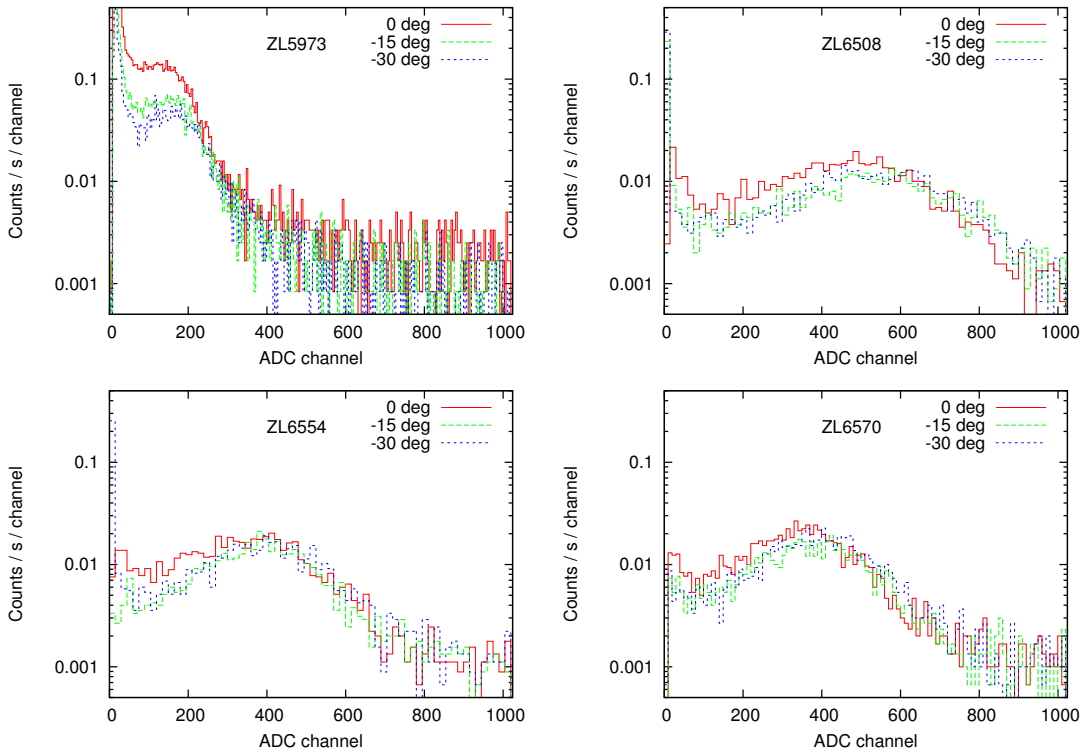

Figure 3.18: Examples of the one p.e. spectra with low temperatures from −30 to 0°C with the bias voltages of +1100 V. Exposure time is 300 s. We can see clear one p.e. peaks with almost same shapes as those at +30°C, which show the PMTs work properly. The one p.e. events significantly reduce to $\sim 1/100$.

Temperature test

All PMTs did not crack when the temperature was changed within ±30°C at the rate of ±0.5°C/min. Most of the PMTs worked with the low temperatures down to −30°C. Figure 3.18 shows examples of the one p.e. spectra. We can see the rate of the one p.e. events decreases by $\sim 1/100$ when the PMT is cooled. This is because the one p.e. events are thermally induced. However, there were two PMTs (ZL5978 and ZL6503) which did not work as expected. Their behaviors are shown later.

3.4.2 Behaviors of the problematic photomultiplier tube assemblies

We show the behaviors of four problematic PMTs. The problems seem to fall into two categories, to have a high-rate noise, and to make a larger noise as the temperature decreases. Though we do not know the reason why they do not work properly, these results will help in the future acceptance tests. The problems are so simple that we can

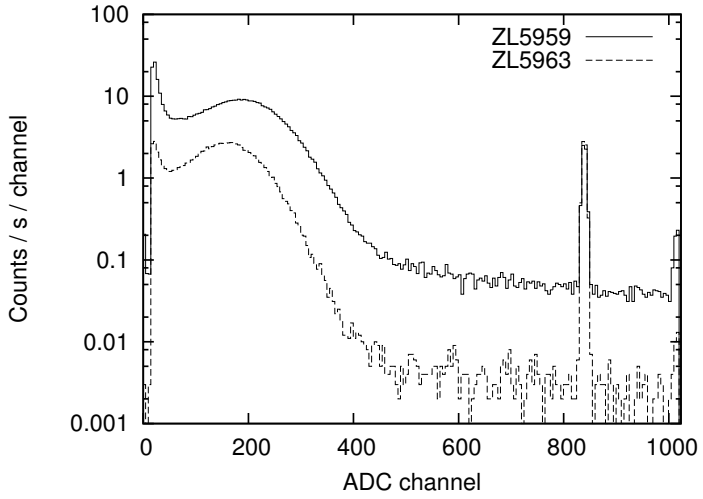

Figure 3.19: The one p.e. and test pulse spectrum of the PMT ZL5959. The spectrum of ZL5963 is simultaneously shown for comparison. The rate of the noise above one p.e. for ZL5959 is ~ 10 times larger than that for ZL5963 while the one p.e. rate is larger by ~ 5 times.

find either in the standard analysis processes or in the DAQ.

ZL5959

ZL5959 has a high-rate noise. Figure 3.19 shows the one p.e. spectra of ZL5959 and ZL5963. ZL5963, which has the nearest gain of ZL5959, is for comparison. The rate of the noise above one p.e. of ZL5959 is ~ 10 times larger than that of ZL5963, and the one p.e. rate is larger by ~ 5 times. The ^{55}Fe spectra was not be able to be acquired clearly due to this large noise.

ZL5978

ZL5978 has a large noise with the low temperatures. Figure 3.20 shows the one p.e. spectra with various temperatures. The spectrum for -30°C shows the largest count rate, which is inconsistent with the feature of the thermal noise. Furthermore, there are a number of events in the region above the one p.e. peak. The rate of the one p.e. events for -30°C is comparable to that for $+30$°C, and the noise rate above one p.e. for -30°C is about an order of magnitude larger than that for $+30$°C.

ZL6451

ZL6451 has a large noise which systematically affects the ^{55}Fe spectra when the higher bias voltage is applied. Figure 3.21 shows the ^{55}Fe spectra with ZL6451 at the bias voltage of $+1250$ V and $+950$ V. We can know the noise level comparing between the obtained spectra and the fitted Poisson distribution. Obviously the noise of $+1250$ V is larger than that of $+950$ V.

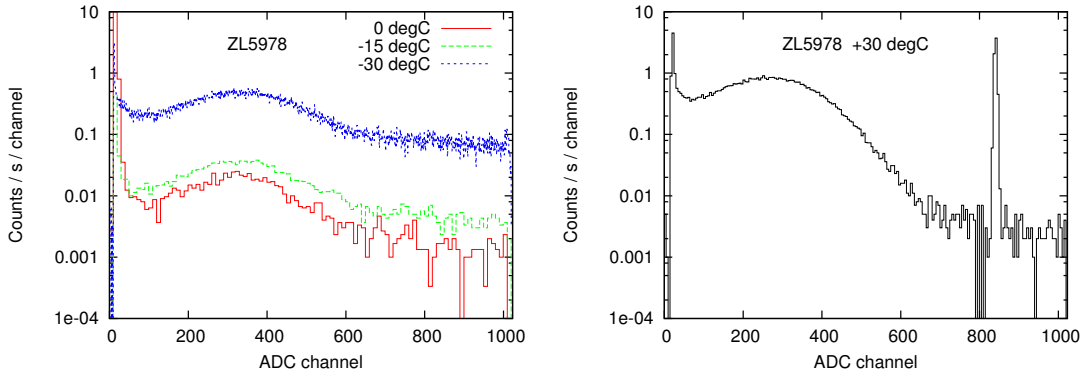

Figure 3.20: Left: the one p.e. spectra with low temperatures for the PMT ZL5978. Right: the one p.e. spectrum of ZL5978 at +30°C for comparison. The spectrum of −30°C shows the largest count rate.

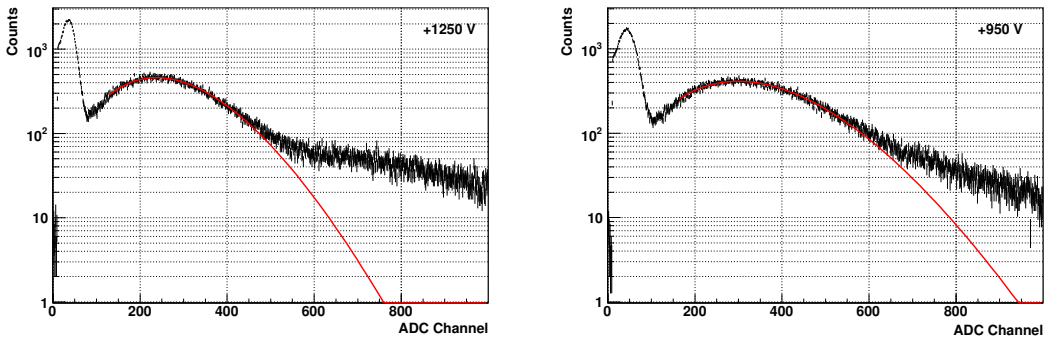

Figure 3.21: The ^{55}Fe spectra of the PMT ZL6451 with the bias voltages of +1250 V (left) and +950 V (right). The red lines show the extrapolated fit models of the Poisson distributions. Obviously the noise with +1250 V is larger than that with +950 V.

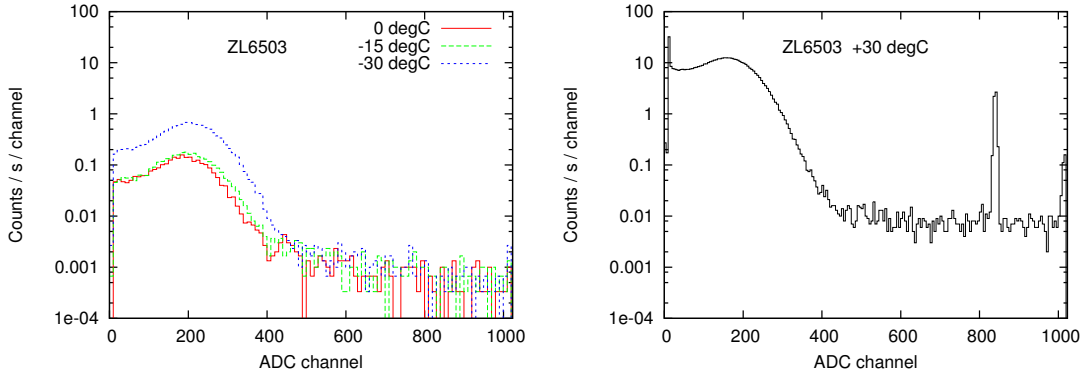

Figure 3.22: Left: the one p.e. spectra with low temperatures for the PMT ZL6503. Like ZL5978, the spectrum of -30°C shows the largest count rate. But the noise rates with the larger pulse height are consistent. Right: the one p.e. spectrum of ZL6503 at $+30$°C for comparison. The event rate is larger than that for the lower temperatures all over the spectrum.

ZL6503

ZL6503 is similar to ZL5978, having the large noise with the low temperatures as shown in figure 3.22. The spectrum with -30°C shows the largest count rate. However, the noise rate with the larger pulse height is almost same as that with -15 and 0°C. Furthermore, the event rate is smaller then that with $+30$°C. This is not the case in ZL5978.

3.5 Summary

We developed the flight-model PMT-ASSYs suitable for PoGOLite. The efficient procedure of the acceptance tests was considered and actually the tests were performed for 53 PMT-ASSYs. We confirmed most of them except for 4 PMTs worked properly. The results for each check items were obtained as below.

- **Bias voltage dependency on the gain.** A power law function describes well the bias voltage dependency between +950 V and +1250 V. The variations of the gain and the index number of the power law function are so small that the variation of the gain can be canceled out with the bias voltage.

- **Power consumption.** When the bias voltage of +1100 V is applied, the power consumption is $\sim$ 260 mW per PMT-ASSY on average. The total power consumption for the 271 PMTs is estimated as $\sim$ 70 70 W.

- **Diode cramp.** A large output signal current with a light from a LED is cramped properly with all of the PMTs. A further study on the response to the large signals is described in chapter 5.

- **Noise.** One p.e. signals can be distinguished from the noise. The fluctuation of the baseline due to the noise is typically 0.025 photoelectrons. The noise level is slightly large for the PMT-ASSYs with the earlier version high voltage modules.

- **Temperature test.** No PMTs crack when the ambient temperature changes between ± 30°C with the rate of ± 0.5°C/min. Most of the PMTs work with the low temperatures between -30°C and 0°C.

Though we do not know what causes of the problems with the irregular 4 PMTs, they are categorized into the two kinds; to have a high-rate noise intrinsically or to make a larger noise with the lower temperatures.

Chapter 4

Polarized photon beam test of a 7-unit prototype polarimeter

We constructed a 7-unit prototype polarimeter with a full PDC, and tested it with a polarized photon beam. The test results were quantitatively compared to Monte Carlo simulation.

4.1 Previous beam tests and objectives of the present test

Prior to the present beam test, we had completed two rounds of prototyping and testing on polarized gamma-ray beams. The first beam test was performed in 2003 at the Advanced Photon Source Facility of the Argonne National Laboratory.[1] The prototype detector was made of 7 plastic scintillation counters spaced wider than the flight model design. The azimuth modulation was measured at beam energies of 60, 73 and 83 keV. The analysis led to finding errors in the treatment of photon polarization in Compton/Rayleigh scattering in Geant4 [51]. In 2004, a second experiment was conducted at the Photon Factory of High Energy Accelerator Research Organization (KEK-PF) in Japan.[2] In this experiment, 7 fast scintillators for PoGOLite were laid out identical to the flight model design. The test covered the lower energy range (30, 50 and 70 keV) [52].

The goals of the present beam test are:

- measure the modulation factor and the detection efficiency accurately with a flight model phoswich detector cell in the lower energies;

[1] http://www.aps.anl.gov/

[2] http://pfwww.kek.jp/index.html

- establish effective background filtering procedure;
- make a quantitative comparison between the measured detector performance and the Geant4 simulation.

4.2 Experiments

The prototype PoGOLite detector used in the test is constructed with 7 units, with one flight model PDC at the center [45]. This was tested at KEK-PF during December 5−12, 2005.

During this experiment, backgrounds were not created artificially. Thus the slow and BGO scintillators were used to only reduce environmental radiation events. Polarization measurement under a high background, which may be made by radioactive sources, is scheduled in the next experiment at KEK-PF in March 2007.

The prototype detector in the present test is shown in figure 4.1. The center unit is the first flight-model PDC. The surrounding 6 units are made of the fast scintillator rods of the flight-model design but do not have the slow scintillator well nor the bottom BGO. The fast and slow scintillators were wrapped in VM2000 sheets manufactured by 3M. The same reflective sheet was inserted inside the slow scintillator well to reflect back fast scintillator light yield. The slow scintillator was then wrapped with a thin tin foil and a thin lead foil (50 μm thick). The BGO scintillator was coated with a reflective layer of $BaSO_4$. The entire assembly was covered by a shrink tube to secure the metal foils and reflective sheets in place. For the surrounding 6 units, the fast scintillators of the surrounding 6 units were wrapped with VM2000 and BGO crystals were substituted with acrylic light guides. The light guides were covered by polytetrafluoroethylene tape. Each unit was attached to a flight-model PMT-ASSY.

The experiment was carried out at station A of beam line 14 (BL14A). The setup is shown in figure 4.2. The BL14A can deliver a vertically plane-polarized beam via two monochromator Si(553) crystals between 30 keV and 80 keV. Data were taken at beam energies of 30, 50 and 70 keV. Although the detectable energy of PoGOLite goes down to 25 keV, we were not able to take a data of 25 keV. The intensity of the beam was reduced $\sim$ 5000 times with metal attenuators made of tungsten and lead in order to prevent pile-up. The beam was collimated to a cross-sectional size of 1 mm squared by thick tantalum plates. The central PDC unit of the detector array was irradiated, and thereby acted as an active scatterer with the six peripheral units absorbing the scattered photons. The numbering scheme of the units and orientation of the polarization plane ('0 degree') are shown in figure 4.3. The instrument was rotated around the center of Ch.1 at 15°

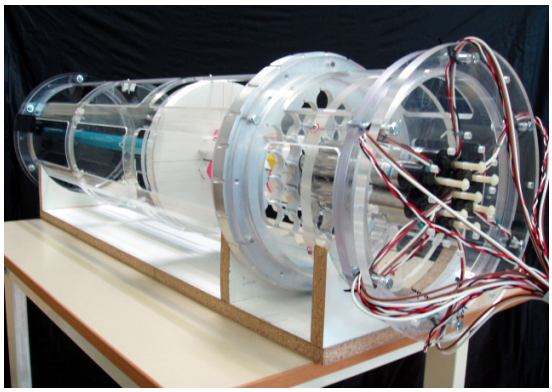

Figure 4.1: A photograph of the PoGOLite prototype detector used in the December 2005 KEK-PF experiment.

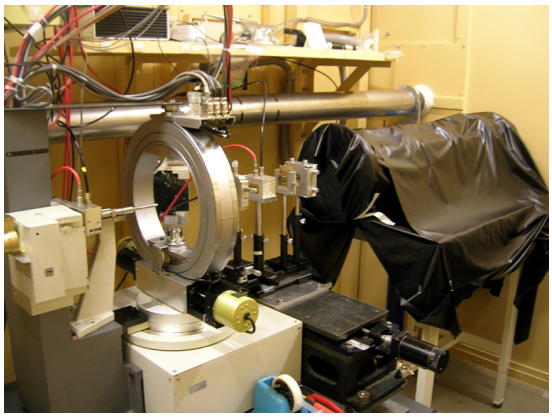

Figure 4.2: A photograph of the setup in the BL14A experimental hutch at KEK-PF. The instrument covered with a black sheet is attached to the experiment table on the right-hand side.

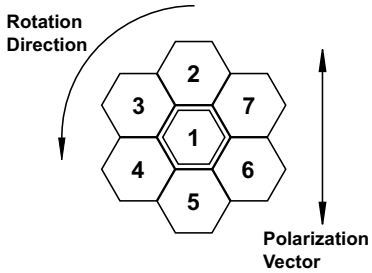

Figure 4.3: The layout and numbering scheme of the prototype detector array at 0°, viewed from the beam origin. The central one (Ch.1) is the PDC unit.

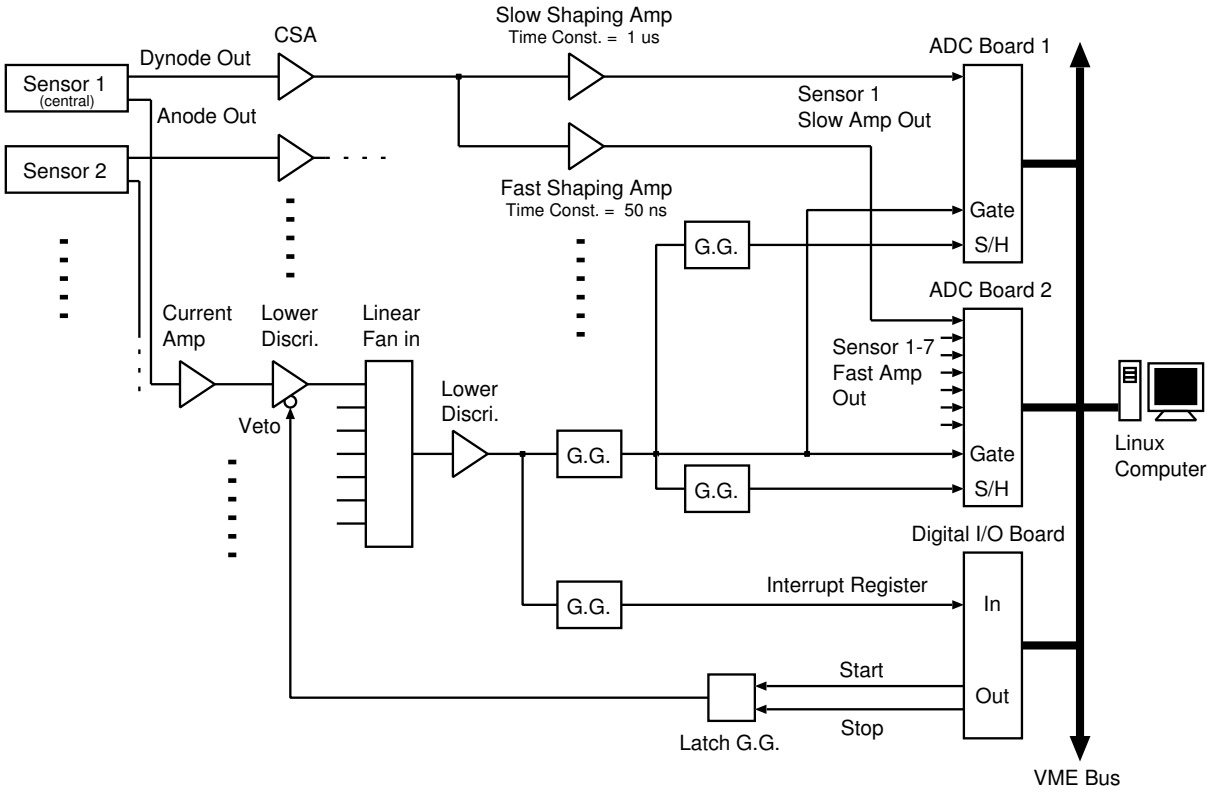

Figure 4.4: The DAQ system of the beam test at KEK-PF. 'G.G.' means a gate generator and 'S/H' means a sample hold input.

steps in the anti-clockwise direction covering the whole azimuthal angle. The count rates measured in each peripheral unit were modulated depending on the rotation angle. Since photons tend to be scattered in the direction perpendicular to the polarization vector, the count rates of Ch.2 and Ch.5 are predicted to be minimum at 0° and 180° and to be maximum at 90° and 270°.

The DAQ system used in the beam test is shown in figure 4.4. The signals from the PMT anodes were used to trigger the DAQ. They were first amplified by a factor of 10 with current amplifiers. The outputs of the amplifiers were fed into the discriminators. Their threshold levels were ~ 0.3 p.e. and the width of the output signal was 50 ns. The outputs of discriminators were fed into a linear fan-in module and a discriminator (N.I.M. standard) to allow a hardware coincidence to be formed. The discriminator threshold voltage was set to -1 V. When at least two sensors fired, a DAQ cycle was initiated. Using this system, the coincidence of any combination of the units was be able to be studied. The output from the last discriminator was widened (and delayed) with gate generators ('G.G.' in figure 4.4), and fed into a digital I/O board (Clear Pulse 2610) which acted as an interrupt register, and into gate and sample hold (S/H) inputs of the

ADC boards (Clear Pulse 1113A, peak hold type). When a signal is sent to the interrupt register, a Linux computer started to read out the ADCs via a VME bus, and a veto signal for the discriminators was asserted. The veto signal was cleared when DAQ cycle ended. The dead time was monitored by a 1 MHz clock and a scaler and used to correct the count rates off-line. The measured dead time per event was $\sim 130\mu$s.

The PMT signals from the last dynode were used for the analog system. For PSD of the fast scintillator hits from those in the slow scintillator and the BGO in the central PDC. The signals were fed to a CSA (Clear Pulse 557), with a fanned-out output. The output of CSA was fed into two kinds of shaping amplifiers which had different time constants, 50 ns ('fast amp', Clear Pulse 4056) and 1 μs ('slow amp', Clear Pulse 4066). Since the fluorescent decay times of the BGO ($\sim$ 300 ns) and the slow scintillator ($\sim$ 285 ns) were longer than the time constant of the fast amp, only the first portion of the charge was integrated for the BGO and slow scintillators, while the fast scintillator signal was fully integrated by the fast amp. On the other hand in the slow amp, almost all of the charge was integrated for all scintillators. Therefore for the slow signals, the ratio of the fast shaping output to the slow shaping output was smaller than that for the fast signals. This is referred to as a double integration method of PSD [15, 16, 17, 22, 23, 24, 25, 26, 27, 28, 29]. For the peripheral 6 units, we installed only fast shaping amplifiers.

Knowledge of the number of incident photons is needed to estimate the detection efficiency. Since we were not able to attach another detector due to space constraints in the beam line, the beam intensity was estimated by the photo-absorption rate at Ch.1. Therefore, a 10 minute run with Ch.1 trigger was inserted before each coincidence trigger run at an azimuth angle. The setup of Ch.1 trigger was realized by skipping the linear fan in and the subsequent discriminator. The number of incident photons was estimated by a combination of a simulation and the photo-absorption rate at Ch.1 (see §4.4). The background data were obtained after the 345°-run for each beam energy, once per a full azimuth rotation.

The polarization degree of the beam is essential in evaluating detector modulation factor. We calibrated it with another polarization monitor. The measured polarization was 0.91 ± 0.01, 0.92 ± 0.01 and 0.91 ± 0.01 for 30, 50 and 70 keV, respectively. A summary of the experiment is described in appendix A.

4.3 Results

Selection of clean events hitting the fast scintillator was done on the two-dimensional distribution of the two pulse-heights, one from the fast integrator and the other from

the slow integrator. The two-dimensional distribution for signals from Ch.1 taken in the 50 keV coincidence run is shown in the left panel of figure 4.5. Clean hits in the fast scintillator are separated from hits in the slow/BGO scintillator. The events with entries in the 'fast branch' (the dashed region in figure 4.5 left) include Compton-scattered events. Spectra for the unfiltered and filtered events are shown by thick and thin solid line, respectively in the right panel of figure 4.5. Events in the high energy range, corresponding to ambient background, were significantly reduced.

The energy was calibrated by using the 50 keV photo-ionization peak in the filtered events. The ADC pedestal were obtained using test pulses.

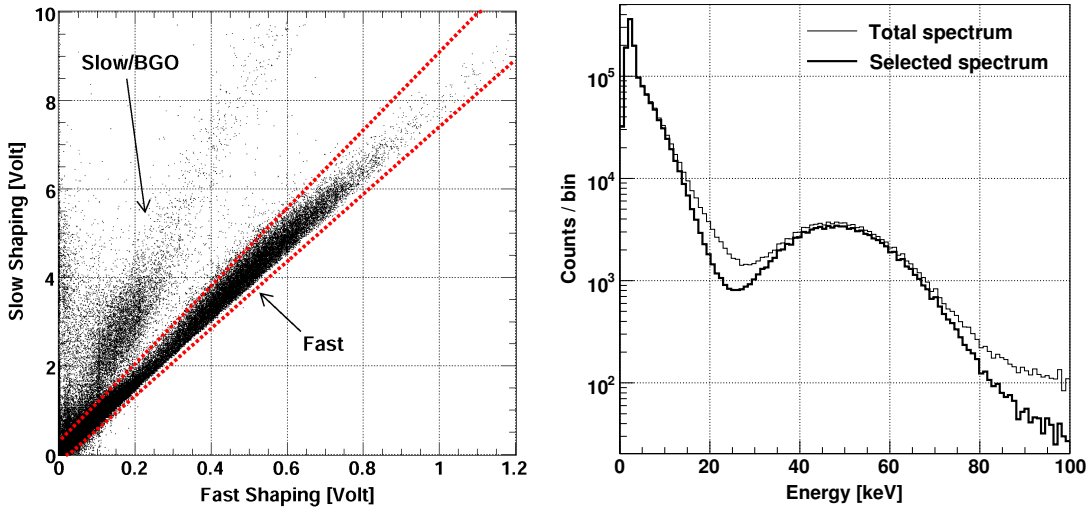

Figure 4.5: Left: relation between the output of fast shaping amplifier and that of slow shaping amplifier for Ch.1 taken in the 50 keV coincidence run. The dashed region shows the 'fast branch' where the events from the fast scintillator entry. Right: total (thin line) and selected (thick line) spectra for the 50 keV beam. Events in the high energy range, which were room background and cosmic-rays, were significantly reduced after the selection. Saturated in the slow shaping, these events do not appear in the left-hand figure.

The second step of data analysis is to select events with a photo-absorption site and a Compton scattering site. In the present setup, the Compton scattering site is Ch.1. This selection is done by examining the energy deposits in Ch.1 (E_1) and the sum of the energy deposit in Ch.1 and the photo-absorption site, one of Ch.2−7 ($E_{\rm tot}$). Distribution of the two energies for coincidence events are shown in the left panels of figures 4.6−4.8.

The region surrounded by the dashed line contains events where incident gamma-rays were scattered in Ch.1 and photo-absorbed in Ch.2−7, 'valid Compton scattering events.' The coincidence condition was applied as a part of off-line data analysis: the selection

criteria were set to maximize the number of Compton scattering events, while reducing background events (photo-absorption in Ch.1, accidental coincidence between the beam and the room background). The criteria were:

- 30 keV run: 1 keV $\leq E_1 \leq$ 12 keV, 15 keV $\leq E_{\rm tot} \leq$ 55 keV and $E_{\rm tot} \geq 1.65E_1$.
- 50 keV run: 1 keV $\leq E_1 \leq$ 25 keV, 30 keV $\leq E_{\rm tot} \leq$ 80 keV and $E_{\rm tot} \geq 1.65E_1$.
- 70 keV run: 1 keV $\leq E_1 \leq$ 35 keV, 45 keV $\leq E_{\rm tot} \leq$ 100 keV and $E_{\rm tot} \geq 1.65E_1$.

This procedure corresponds to the Compton kinematics filtering. The same criteria were applied to the background runs and the background were subtracted from the beam data, after the dead time correction. The background events accounted for $\sim 5\%$ for 30 and 50 keV and $\sim 15\%$ for 70 keV.

The numbers of signal events for each coincidence combination for 3 coplanar pairs, Ch.2 and Ch.5, Ch.3 and Ch.6 and Ch.4 and Ch.7 were plotted as a function of azimuthal angle settings in the right panels of the figures 4.6−4.8. The curves show the best-fit cosine functions. The modulation factor, $M_{\rm obs}$, is defined on the maximum and the minimum ratios ($R_{\rm max}$ and $R_{\rm min}$, respectively) as,

$$M_{\rm obs} = \frac{R_{\rm max} - R_{\rm min}}{R_{\rm max} + R_{\rm min}}.$$

The expected modulation factor for 100% polarized gamma-rays, M_{100}, is defined as $M_{100} = M_{\rm obs}/P$, where P is the degree of polarization of the beam. We obtained M_{100} to be 0.344 ± 0.004, 0.358 ± 0.012 and 0.372 ± 0.011 for 30, 50 and 70 keV, respectively.[3] These results clearly show that polarization can be determined using the flight model PDC.

More detailed analysis of this experiment was performed by Ylinen. See his master thesis [54].

4.4 Comparison to a Monte Carlo simulation

In this section, the experimental results are compared to simulated data. The simulation was performed with using the Geant4 Monte Carlo package. The treatment of the polarization vector of the Compton/Rayleigh scattered photons was modified [51]. The components in the geometry model of the detector model is shown in table 4.1. The

[3] The same Compton kinematics filtering described above was applied for the data-sets acquired with the Ch.1 single trigger. Modulation factors were obtained as 0.346 ± 0.008, 0.360 ± 0.008 and 0.380 ± 0.009 for 30, 50 and 70 keV, respectively. They were consistent with the results of the coincidence trigger run.

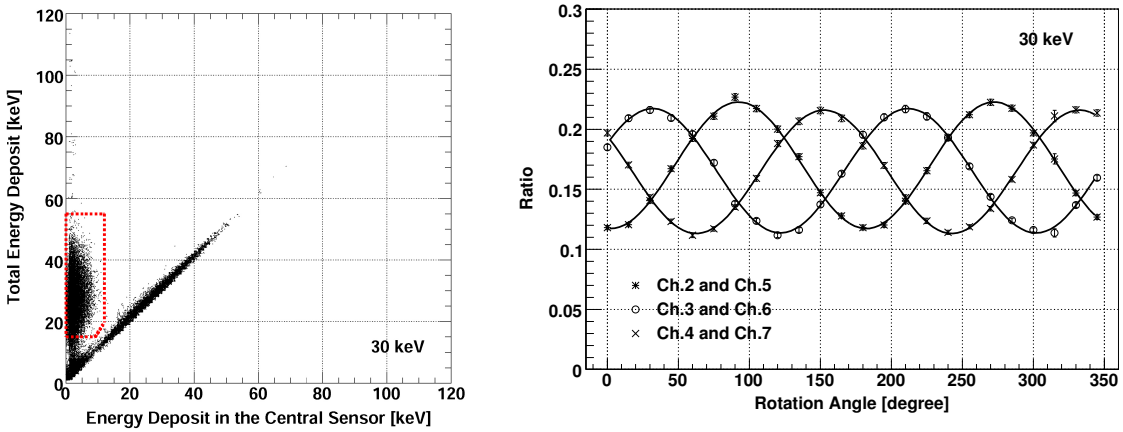

Figure 4.6: Left: relation between energy deposit in the central sensor and the sum of the energy deposit in Ch.1 and in one of Ch.2−7 for the 30 keV beam. Right: modulation of the rates as the function of the rotation angle for the 30 keV beam.

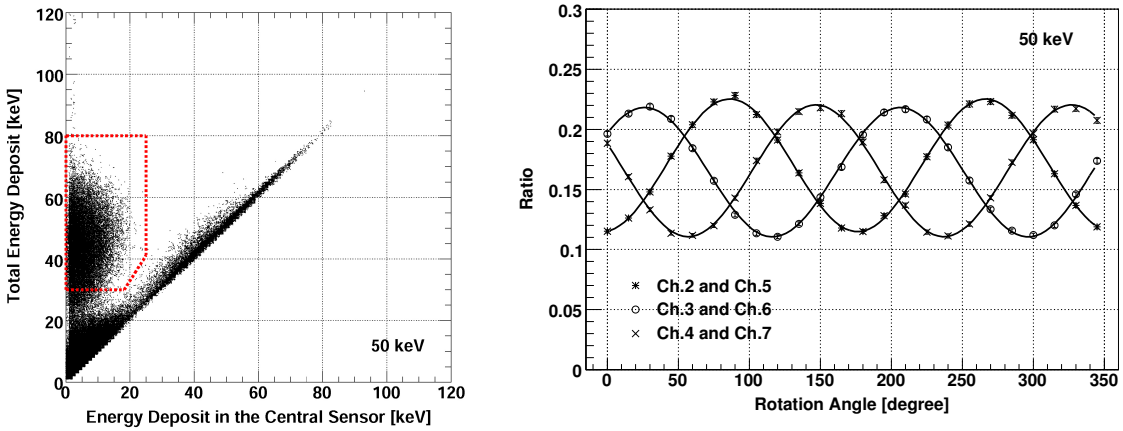

Figure 4.7: Same as figure 4.6, but for the 50 keV beam.

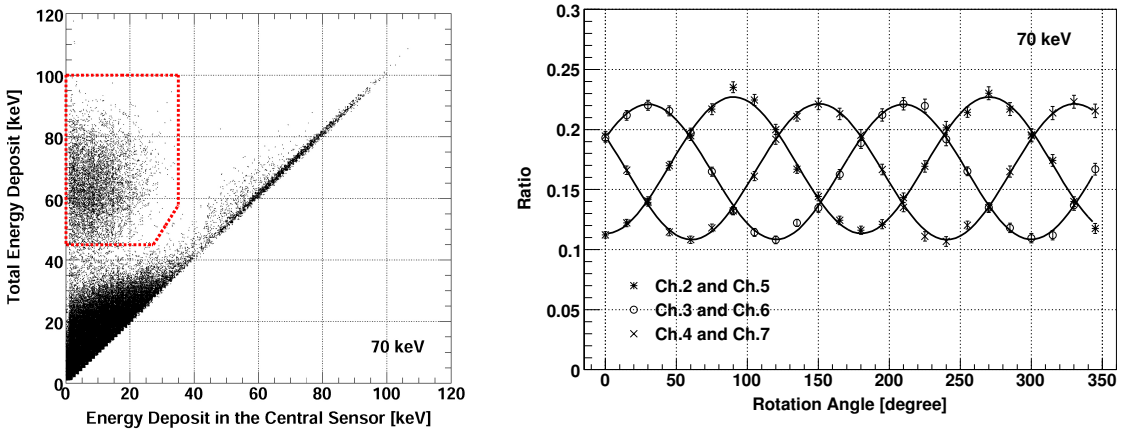

Figure 4.8: Same as figure 4.6, but for the 70 keV beam.

Table 4.1: The components included in the geometry model for the Monte Carlo simulation. Their sizes and positions are same as the actual detector. We can be aware of the energy deposition in the 'active materials,' and cannot for the 'passive materials.'

	Active materials	Passive materials
Central unit (PDC)	Slow scintillator	Tin foil
	Fast scintillator	Lead foil
	BGO scintillator	$BaSO_4$
Peripheral units	Fast scintillator	Acrylic light guide
Others		Acrylic support plate

detector was rotated to cover whole azimuthal angle with 15° steps. We injected the fully polarized photons to the center of the central PDC. The number of the incident photons was 10^6 at each rotation angle. The detector response was convolved to the output data from the Geant4 with ROOT. The actual values were used for the light yield of the fast scintillators, 0.48 p.e./keV for the central PDC and 1.02 p.e./keV for the peripheral units. Following the simulation by Arimoto [53], we assumed that PSD was not able to rule out the events with energy depositions of 15 keV in the BGO scintillator and 30 keV in the slow scintillator. The results with the simulation are given in table 4.2, together with the corresponding measurement at various energy bands. These results agree with the experimental results to an accuracy of $\sim 10\%$.

Detection efficiencies were calculated. The total number of the incident photons in the experiment, N_0, are estimated by $N_0 = N_{\rm abs}/p$, where $N_{\rm abs}$ is the number of the photo-absorption events in Ch.1 corrected with dead time, and p is the simulated fraction that photo-absorption occurs in Ch.1. The detection efficiency is defined by the total number of the 'valid Compton scattering events' divided by N_0. The resulting values are given in Table 4.2. The detection efficiencies agree within 10% between the experiment and the simulation. Figure 4.9 shows the energy dependence of the detection efficiency derived from the experiment and the simulation.

The small differences between experiment and simulation for both of the modulation factors and the detection efficiencies could be due to the misalignment, uncertainties in the background subtraction, the uncertainty of the simulation and the complex light output response of the plastic scintillator (quenching effect, position dependency and so on).

We conclude the Geant4 simulation with the modification by Mizuno et al. [51] reproduced the experimental modulation factor and the detection efficiency within $\sim 10\%$ (relative). The prototype phoswich polarimeter performs in line with the expectations derived from the Geant4 simulation. Some differences remained, however, and will be the

Table 4.2: The comparison of the experimental results to the simulated values of the modulation factor and the detection efficiency. Errors include both statistical and systematic errors.

Energy [keV]	Modulation factor		Detection efficiency [%]	
	experiment	simulation	experiment	simulation
30	0.344 ± 0.004	0.388 ± 0.003	3.69 ± 0.12	3.974 ± 0.005
50	0.358 ± 0.012	0.403 ± 0.005	2.86 ± 0.07	2.610 ± 0.004
70	0.372 ± 0.011	0.409 ± 0.009	1.38 ± 0.09	1.341 ± 0.002

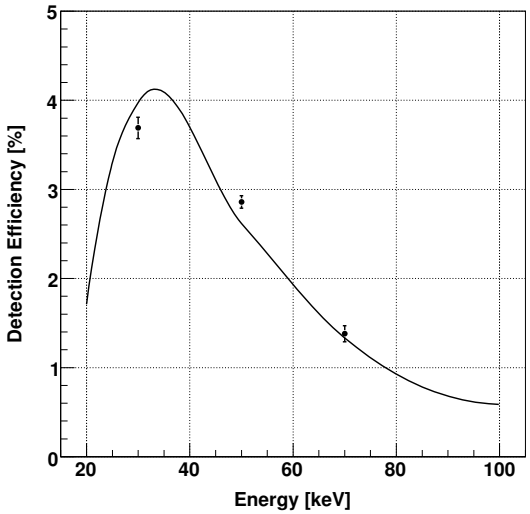

Figure 4.9: Energy dependence on the detection efficiency of the prototype model. The dots show the experimental value, while the line is the result of the simulation.

subject of further careful examination.

4.5 Summary

We constructed a 7-unit prototype polarimeter including a full PDC at the center. In order to measure modulation factor and detection efficiency of the prototype and to compare the polarimeter's performance to a Monte Carlo simulation, a beam test was performed at a synchrotron radiation facility, KEK Photon Factory. The central PDC was irradiated by a highly polarized photon beam. The energy of the beam was 30, 50 and 70 keV. We verified that the PDC can detect recoil electrons and select valid Compton scattering events down to 30 keV from background. A polarization signal was clearly identified. The measured azimuthal modulation factors are 34.4 %, 35.8 % and 37.2 % at 30, 50, and 70 keV, respectively. They were compared to those derived from a simulation using the

Geant4 package. They agreed with the results of the simulation within $\sim 10\%$ accuracy. The detection efficiency of Compton scattered events was also determined. These values were reproduced by the simulation to < 10 %. These results confirm that the prototype phoswich polarimeter design adopted by PoGOLite performs in line with expectations from simulations. Some differences remained, however, and will be the subject of further careful examination.

Chapter 5

Proton beam test of a Phoswich Detector Cell

We performed a proton beam test using a full sensor unit consisting of a PDC (Phoswich Detector Cell), a flight-model PMT and prototype readout electronics. Spectra of ^{241}Am were compared under various background proton rates expected in flight.

5.1 Objectives of this test

The first objective was to examine a response of a PMT with divider system to large input signals. As noted in chapter 3, PoGOLite PMTs utilize diodes to cramp large signal current. Prior to this beam test, the large signal response of the PMTs had been examined to have no problem with LED irradiation that mimicked the high energy deposition. The actual response to a bright scintillation light was not known. In this experiment, a realistic simulation of background particles in a balloon flight was performed.

The second objective was to make a quantitative comparison of various readout electronics. Figure 5.1 shows output waveforms from two CSAs, which differ significantly. The response of the detector can depend on analog electronics. Thus the 'total' response must be examined. We used for the first time prototype analog electronics which was specifically designed for PoGOLite. Therefore, the result of this experiment can provide important feed back for the future design of the flight-model electronics. Study of the DAQ system was also needed. We had often used the double integration method for PSD (pulse shaping discrimination) but this requires two shaping amplifiers for each readout channels as we have shown in chapter 4. If PSD can be made directly with the waveform of a CSA output, we can remove both the fast and slow shapers. This leads to the simpler electronics. On the other hand, this new method may have unpredictable demerits and

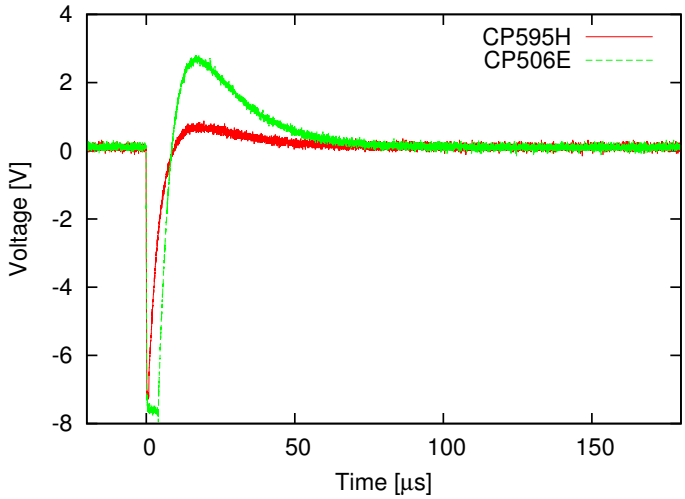

Figure 5.1: Output waveforms of two CSAs (Clear Pulse 595H and Clear Pulse 506E) when a PoGOLite flight-model PMT was irradiated by a LED. Although the time constants of the CSAs were same (5 μs), their recovery waveforms are clearly different. The input signal was $\sim$ 14000 p.e., which corresponded to the energy deposit of $\sim$ 28 MeV in the fast scintillator where 0.5 p.e./keV is assumed.

problems. We wanted to find them in this experiment. We can also give feedbacks to the flight-model DAQ design based on the results of this experiment.

5.2 Experiments

The experiment was conducted at the cyclotron facility of the Research Center of Nuclear Physics in Osaka University.[1] The AVF (Azimuthally Varying Field) cyclotron and the ring cyclotron produce $<$ 400 MeV protons and heavy particles of $<$ 70 MeV/nucleon in the facility. We used a beam line named ES Course. This course features a diffuse and weak beam, which satisfies our required experimental conditions.

We used the same PDC provided in the photon beam test described in chapter 4 and a flight-model PMT. Bottom BGO and PMT were optically connected with a piece of silicon rubber (1.4 mm thick) and some optical grease.

[1] http://www.rcnp.osaka-u.ac.jp/Divisions/np1-a/index.html

5.2.1 Estimation of the deposited energies by background cosmic-ray particles in a balloon flight

At first, we estimate the deposited energies by background cosmic-ray particles in a balloon flight, which is necessary to perform a conservative experiment.

Our previous simulation [59] showed the hit rate of the particle background (primary protons and secondary protons, electrons and positrons) per PDC in flight will be ~ 350 Hz. Now we estimate their energy deposit very roughly as below based on the flux model (figure 5.2) though a computer simulation is required for an accurate estimation.

- Protons: Most primary protons are relativistic (maximum at a few GeV). The minimum ionization loss of relativistic protons is 2 MeV cm^2 g^{-1}, thus the energy deposit for protons is typically < 100 MeV, which is expected when a proton passes both of the fast scintillator (1.0 g cm^{-3}, 20 cm tall) and the BGO scintillator (7.1 g cm^{-3}, 4 cm tall).

- Electrons and positrons: The energy distribution has a peak at 100 MeV and low-energy (< 100 MeV) electrons and positrons are dominant. They deposit almost all of the initial energy when they penetrate the BGO scintillator. The average energy deposit is obviously less than 100 MeV.

Hence, energy deposit of 100 MeV at 350 Hz is sufficient for a realistic simulation.

In our experiment, we fixed the beam energy at 392 MeV. Energy deposit of 392 MeV protons is 2 MeV cm^2 g^{-1}, which is coincidentally almost same as relativistic protons' minimum ionization losses. Therefore we were able to perform a conservative simulation of the realistic charged particle background if the PDC was irradiated with protons longitudinally from the top of the slow scintillator at ~ 350 Hz.

5.2.2 Electronics setups

We prepared three electronics setups for comparison. They are shown in figures 5.3 and 5.4.

In the first and second ones (figure 5.3), we used a waveform analyzer. We used 'PoGOLite version 1 board' (hereafter 'v1 board') and a ready-made simple CSA, Clear Pulse 595H (CP595H), were used as the CSAs. We intended to compare the amplifiers with different responses. For the two CSAs, feedback capacitance and resistance were 10 pF and 200 kΩ, respectively.

The waveform analyzer ADLINK PCI-9810 is a PCI card with four channel analog inputs working with the sampling rates of up to 20 M samples per second (MS/s). We

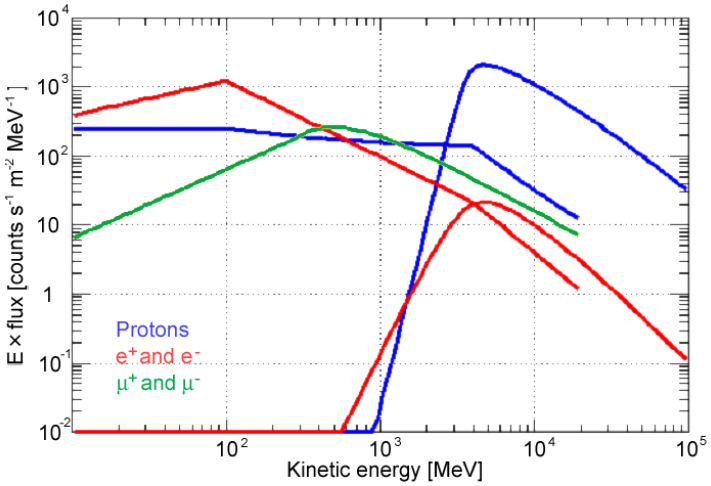

Figure 5.2: Energy spectra of cosmic-ray protons, electrons, positrons and muons at the altitude of the balloon flight. This is for the Balloon Flight Engineering Model of GLAST satellite launched at Palestine, Texas [33]. Protons, electrons and positrons are dominant components. The protons' spectrum has a peak at a few GeV and most of electrons and positrons are below 100 MeV. Although the relativistic electrons and positrons exist, their flux is negligible.

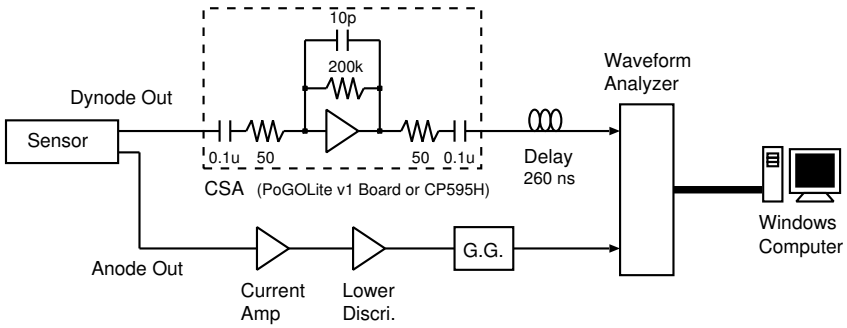

Figure 5.3: DAQ system with the waveform analyzer. Output waveforms from CSAs for each events are recorded by the waveform analyzer.

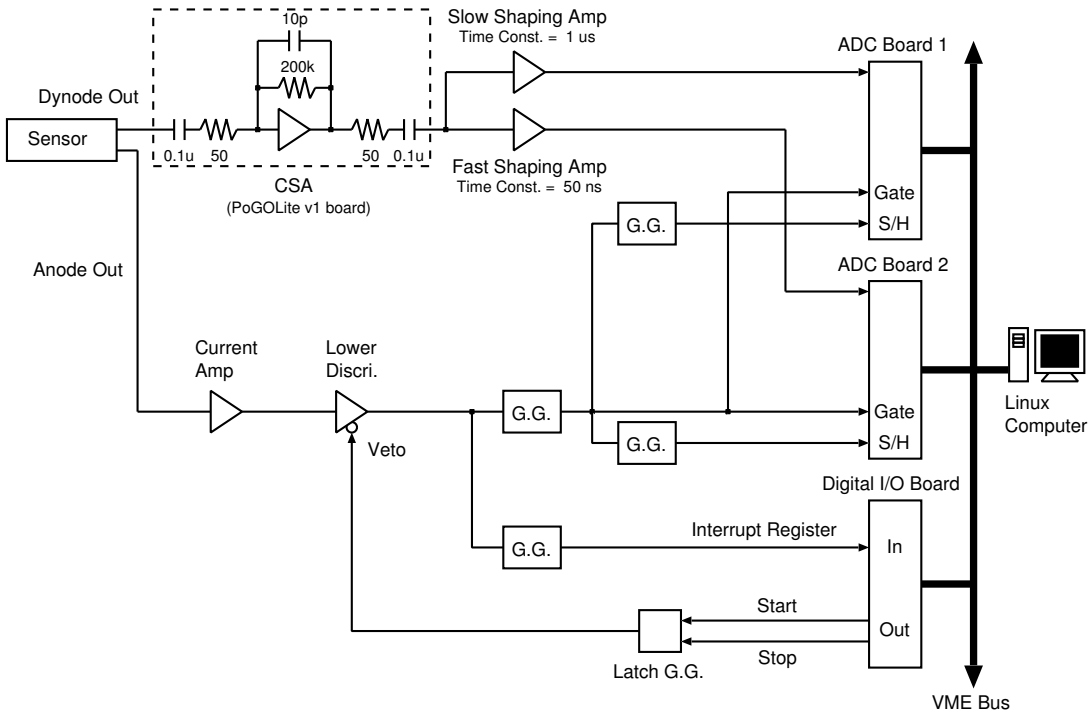

Figure 5.4: DAQ system with the two shaping amplifiers and the VME ADCs. Peak voltages of the output of the shaping amplifiers are read by the sample hold ADCs. 'G.G.' is a gate generator and 'S/H' means input of sample hold signals. Only one type of CSA (v1 board) was used.

used this card with 20 MS/s and 30 samples per event. Although the input analog signals themselves can be used as a trigger source, we used an external trigger source for the stable operation of the waveform analyzer. We created NIM level trigger signals from the PMT anode output. The anode output was amplified with a current amplifier by 30 times, and fed into a discriminator with a threshold of 0.3 photoelectrons. The discriminator output was fed into a NIM gate generator to be widened to 5 μs. This gate signal was fed into the waveform analyzer. The analog signals were delayed by 260 ns before being fed into the waveform analyzer to allow the whole rising portion to be recorded. Since the dead time cannot be measured with this card, we did not apply dead time correction and background subtraction in this experiment.[2]

The third setup (figure 5.4) consisted of the v1 board, fast and slow shaping amplifiers and VME ADCs. The digital electronics including timing of logic signals was same as the one for the photon beam test (figure 4.4), except for the coincidence module. This setup was used to compare the 'classical' double integration method and the new waveform method.

Bias voltage of the PMT was set to +1250 V when used with the waveform analyzer, and it was set to +1100 V when used with the VME ADCs, in order to make effective use of the dynamic range. In both systems, the PMT's last dynode output was fed into a CSA. Data were analyzed in off-line. Any on-line event selection except for the LD trigger was not applied.

5.2.3 Irradiation configurations

We irradiated ^{241}Am at the center of the PDC with the proton beam. We expanded the beam profile as large as possible with an aluminum plate placed in the beam pipe, and we roughly examined the beam profile with the emission of ZnS scintillator coated on a ruled paper in front of the ejection window. The obtained image is shown in figure 5.5 left for the beam current of $\sim$ 50 pA, corresponding to a proton flux of 3×10^8 Hz. We found from the image only that the beam spread over $\sim$ 5 cm $\times$ 5 cm peaking at the center. It is known that the intensity decreases by half at the edge [55]. Its schematic picture is shown in figure 5.5 right.

We placed the PDC with respective to the proton beam with three configurations as shown in figure 5.6. Hereafter the configurations are denoted by the numbers in the figure. Since injection position and angle differed, the energy deposition of protons changed significantly. The energy deposit is 40, 1 and 100 MeV for configuration (1), (2) and (3),

[2] The flight electronics for PoGOLite will be able to measure dead time.

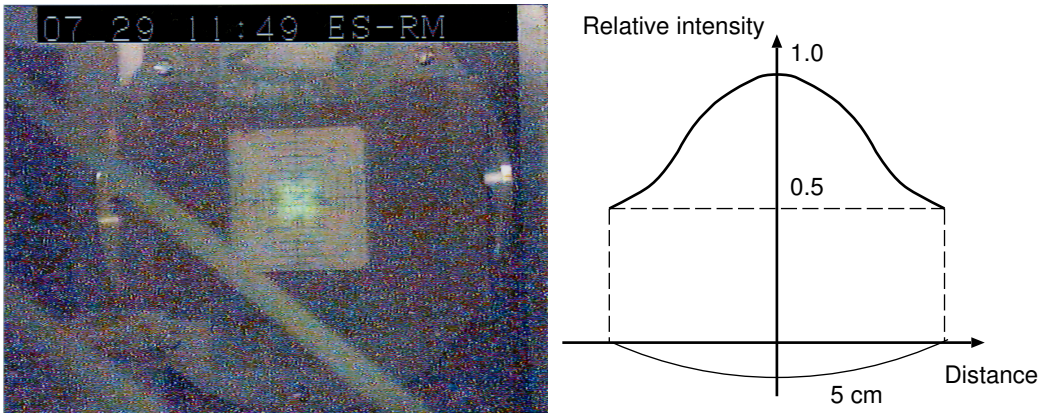

Figure 5.5: Left: image of the proton beam profile spreading over $\sim$ 5 cm $\times$ 5 cm. A ruled paper coated with ZnS scintillator was placed in front of the ejection window. Right: schematic picture of the proton beam profile [55].

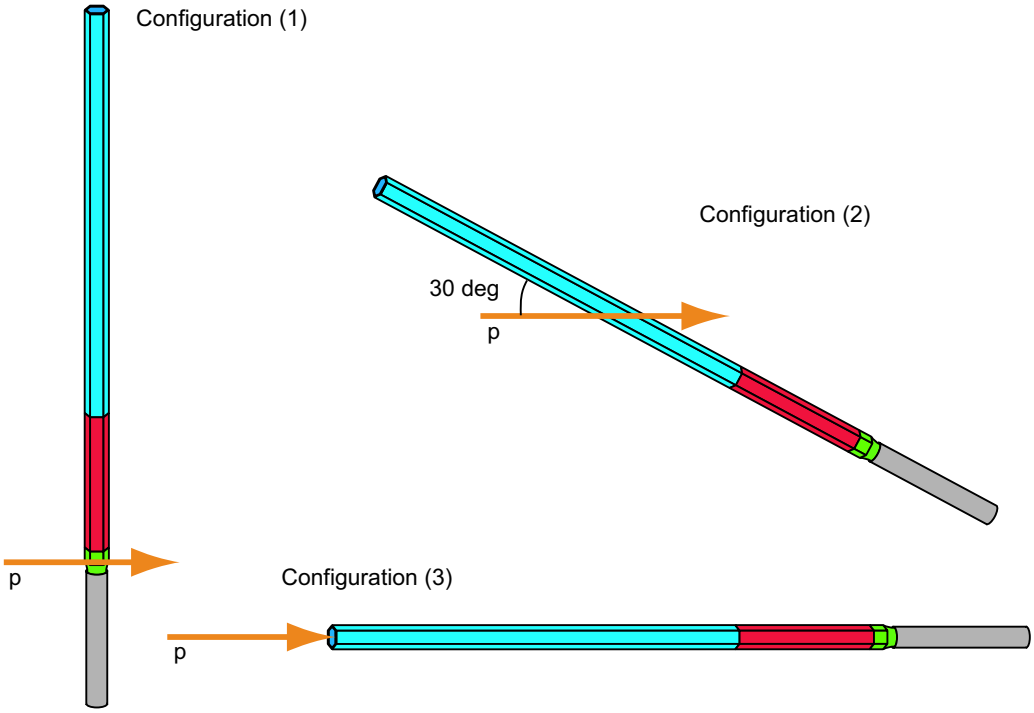

Figure 5.6: Three irradiation configurations in the proton beam test. In configuration (1) and (2), only BGO scintillator and only slow scintillator was irradiated, respectively. The fast and BGO scintillators were irradiated in configuration (3). The energy deposits are 40, 1 and 100 MeV for configuration (1), (2) and (3), respectively.

respectively. In the course of the experiment, the PDC was accidentally disconnected after the measurement with the configuration (2), causing slightly different optical coupling condition for the configuration (3).

The incoming beam rate was monitored by the coincidence of the PDC and a plastic

Table 5.1: Summary of the measurement conditions in the proton beam test. Double integration method was used only for configuration (3).

Irradiation configuration	Electronics setup	Proton rate (Hz)	Exposure (s)
Configuration (1)	v1 board + waveform analyzer	$0, 10^2, 10^3, 10^4$	600
	CP595H + waveform analyzer	$0, 10^3$	600
Configuration (2)	v1 board + waveform analyzer	$0, 10^2, 10^3, 10^4$	600
	CP595H + waveform analyzer	$0, 10^3$	600
Configuration (3)	v1 board + waveform analyzer	$0, 10^2, 10^3, 10^4$	600
	CP595H + waveform analyzer	$0, 10^3$	600
	v1 board + shaping amplifiers + VME ADCs	$0, 10^3$	300

scintillator set in front of the beam ejection window. The size of the plastic scintillator was 4 cm $\times$ 4 cm $\times$ 1cm, and it was mounted on a PMT (Hamamatsu R7195) via an acrylic light guide. Threshold level of the plastic scintillator was set to 1 MeV, while 392 MeV protons deposited 2 MeV when they penetrated the scintillator along the normal to the 4 cm $\times$ 4 cm face. The width of the discriminator output signal was 50 ns. We took a coincidence of this signal and the PDC discriminator output, and counted the number of protons by a visual scaler. The measured rate always underestimated the true value because the plastic scintillator was smaller than the spread of the beam. We estimated that it was $\sim 15\%$ less than the true injection rate with the beam profile.

We were able to change the beam rate only roughly, to an accuracy of factor of ~ 3. We set the injection rate of the order of 10^2, 10^3 and 10^4 Hz as measured by the coincidence signal rate, for each detector configuration. We confirmed that the activation background was negligible at these proton rates.

We used the system with CP595H and the waveform analyzer for the beam-off and $\sim 10^3$ Hz irradiation measurements. Readout by the VME ADCs was used only for beam off and $\sim 10^3$ Hz irradiation of configuration (3). Exposure time of each run was 600 s for the waveform analyzer, and 300 s for VME. The measurement conditions are summarized in table 5.1. To record whole waveform of each signals, we also had 1 min runs for each $\sim 10^3$ Hz irradiation, using the waveform analyzer with 2500 samples.

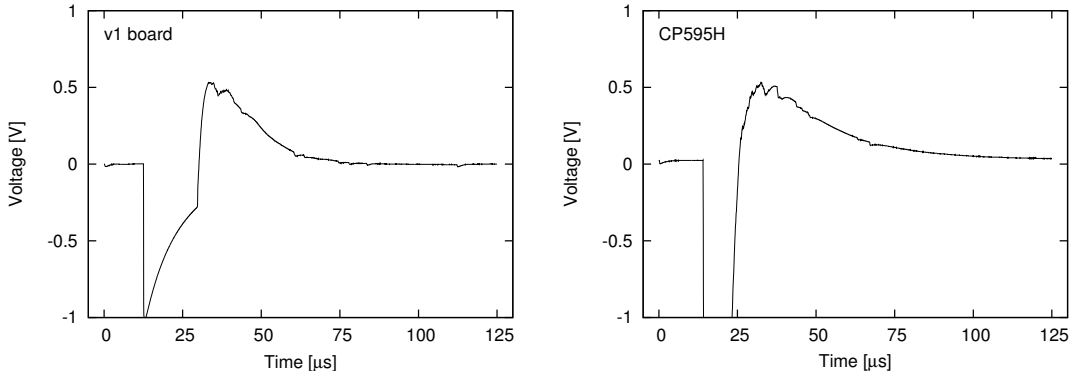

Figure 5.7: Examples of the output waveforms from the CSAs for a proton event in configuration (3) (left: v1 board, right: CP595H). The waveform analyzer was saturated at -1.0 V. The signals recovered in 100 μs with both CSAs.

5.3 Results and discussions

5.3.1 Waveform of large output signals

At first, we examined the recovery time from large signals of protons. Configuration (3) is best suited for the check because the PDC suffers the largest energy deposit. Thus we examined waveforms of proton events in configuration (3).

Figure 5.7 shows the obtained typical waveforms of proton events. The signals recovered in 100 μs with both CSAs, so we confirmed that the experiment using a LED well traced the energy deposit caused by high energy particles.

5.3.2 Pulse shape discrimination method utilizing waveforms

To perform PSD, differences of the rise times of the CSA output signals have to be found out by using proper algorithm. Though there are numerous methods of PSD and we have compared several ones, we show only the best one comprehensively in this report. Our principles were to apply simple logic and not to discard any events detected by the fast scintillator (hereafter 'fast events') buried in the slow or BGO scintillator events (hereafter 'slow events'). The 'fast events' have short rise time and the 'slow events' have long rise time. They become more difficult to discriminate as the pulse heights get smaller in principle. Ultimately, the one p.e. signals never be able to discriminate.

As a viable method, we focused on the analysis of the differential waveforms created by subtracts the waveforms delayed by certain clocks from the original waveforms. The differential waveform can be very different for the fast and slow signals as shown in figure 5.8. Here the delays of 2 and 14 clocks are chosen based on our quick-look analysis, and

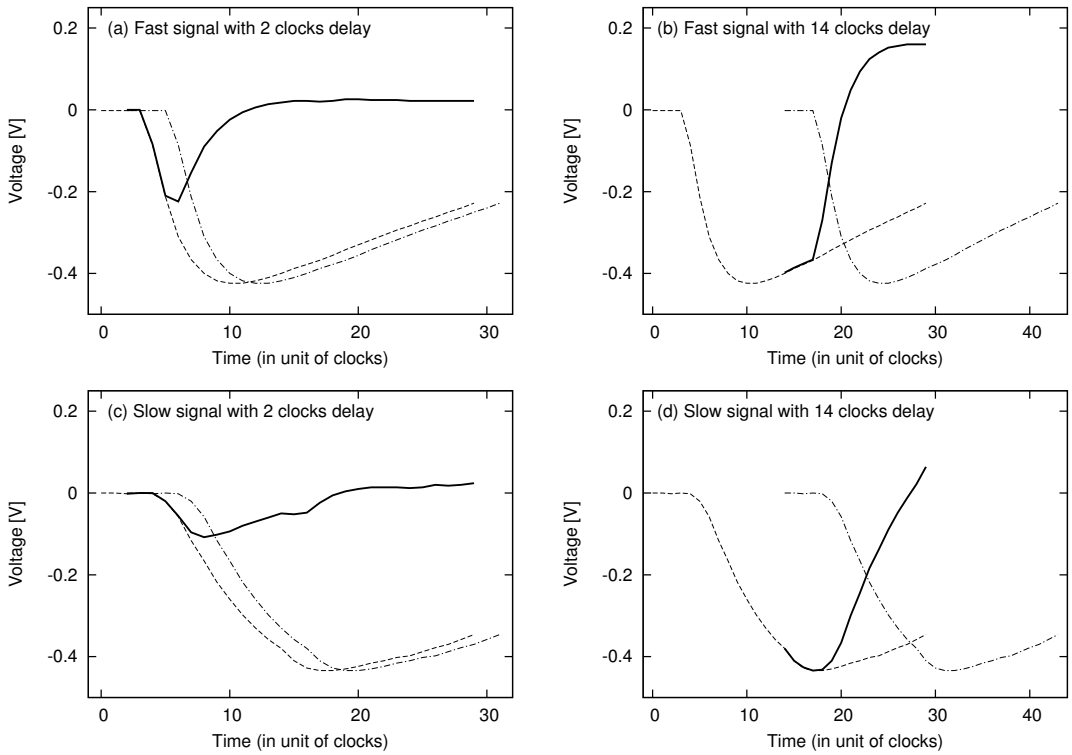

Figure 5.8: An example of the differential waveforms for the fast and slow events. Dashed lines, dash-dotted lines and thick solid lines correspond to the original, delayed and differential (original − delayed) waveforms. (a) fast event with a 2-clock delay, (b) fast event with a 14-clock delay, (c) slow event with a 2-clock delay, (d) slow event with a 14-clock delay. The differential waveforms significantly differ while the original pulse height is almost same.

are not necessarily optimized. The optimization is described later in §5.3.5. Let us define the minimum voltages[3] of the differential waveforms for 2 clocks and 14 clocks delay (thick solid lines) as V_2 and V_{14}. The ratios of V_{14}/V_2 differ significantly between the fast and slow events. In the case of figure 5.8, the ratio is $(-0.398)/(-0.224) = 1.78$ for the fast event and $(-0.434)/(-0.108) = 4.02$ for the slow event while the pulse heights of the original waveforms were almost same. The fast and slow events can be discriminated by the relation between V_2 and V_{14} as above.

As a demonstration we drew a two-dimensional histogram with the horizontal axis of $-V_2$ and the vertical axis of $-V_{14}$ to discriminate fast and slow events. We also derived spectra of selected fast events. We adopted the following algorithm. Figure 5.9 shows examples of the waveforms obtained for each steps.

1. Subtract the 2-clock-delayed waveform from the original waveform and derive offset

[3] Note that the signal polarity was negative.

voltage of the differential waveform as the average of the first two points. Search a minimum voltage (V_2) of the offset-subtracted differential waveform.

2. Repeat the same calculation of the second step to derive V_{14}. Offset voltage is increased by $14/2 = 7$ times at this time (the reason is described in appendix B.1).

3. Subtract the 'baseline' from the original waveform (see the caption of figure 5.9). A pulse height is defined as the minimum voltage of the baseline-subtracted waveform.

4. Make a two-dimensional histogram on V_2 and V_14, and select a region where the fast events are distributed ('fast branch'). Then we obtain three spectra of all events without the selection, fast events and the other events not included in the fast branch.

Figures 5.10 and 5.11 are drawn for the datasets of configuration (3) with the v1 board. Though figure 5.10 resembles to the two-dimensional shown in figure 4.5, axes are different from theirs (peak voltages of the output of fast and slow shaping amplifiers). There are some branches in figure 5.10. A branch surrounded by the dashed lines corresponds to the fast events and the one on the left side of the fast events corresponds to the slow events. This was confirmed by the relationship between V_2 and V_{14} for the fast and slow signals described above. The events on the upper edge are saturated events, and their distribution changes with proton rates. The leftmost events, which cannot be seen in the beam-off data, and the rightmost events, which can be seen clearly only in 78.6 kHz irradiation, are not identified but they seem to be associated with the proton rates. We will examine these events in §5.3.3.

Figure 5.11 shows the spectra of all events without selection, the fast events and the other events not included in the fast spectrum. The 'fast events' are selected from the dashed region in figure 5.10. We identified the peaks at ~ 0.35 V were the photo-ionization peaks of 59.5 keV gamma-rays, which was not present in the 78.6 kHz irradiation data, based on the PMT output charge. The leftmost peaks are consistent with one p.e. peaks, in comparison with the voltage of the 59.5 keV photo-ionization peaks.

The above scheme of PSD basically does not seem to have serious problems except for the unidentified event clusters in the two-dimensional histograms.

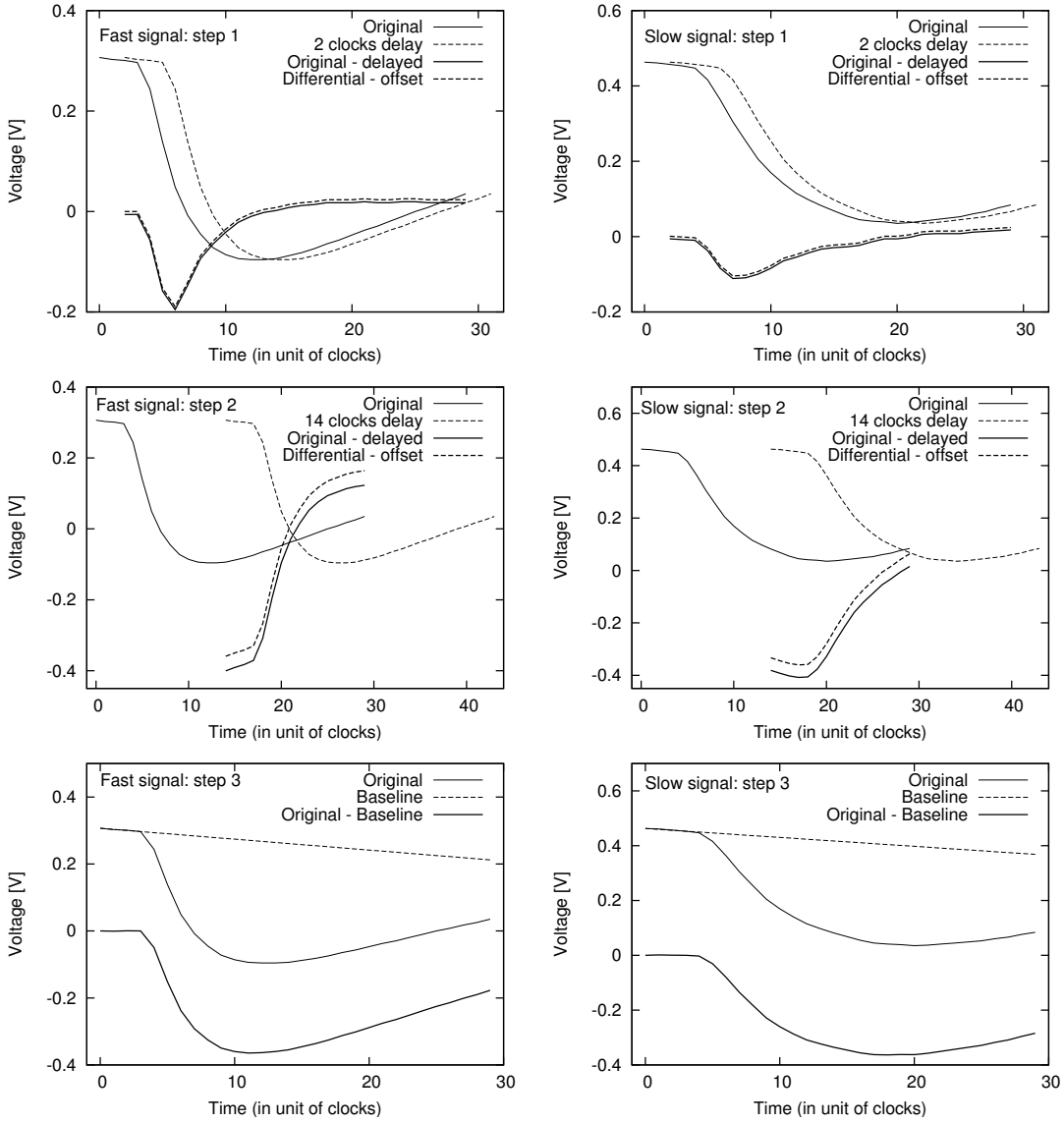

Figure 5.9: Examples of the obtained waveforms for each steps in the PSD algorithm (Top row: step 1, middle row: step 2, bottom row: step 3). Left column is for a fast signal and right column is for a slow signal. In the baseline subtraction, the original waveform lies on a slowly decreasing component. For the 'baseline subtraction' in the step 3, the baseline is approximated by a linear function (dashed line) which passes two points of the zeroth clock and the third clock.

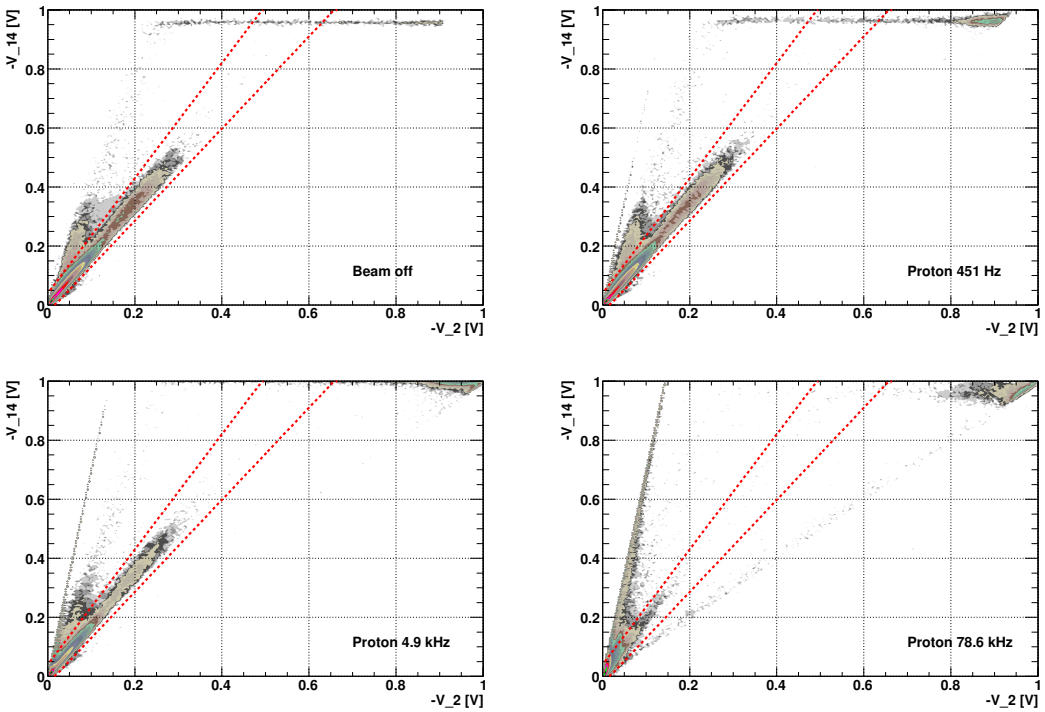

Figure 5.10: Two-dimensional histograms for each proton injection rates in configuration (3). Events surrounded by the red dashed lines are the fast events. There are slow events on the left side of the fast events. Saturated events appear on the upper edge of each panels. See the main text concerning the other events.

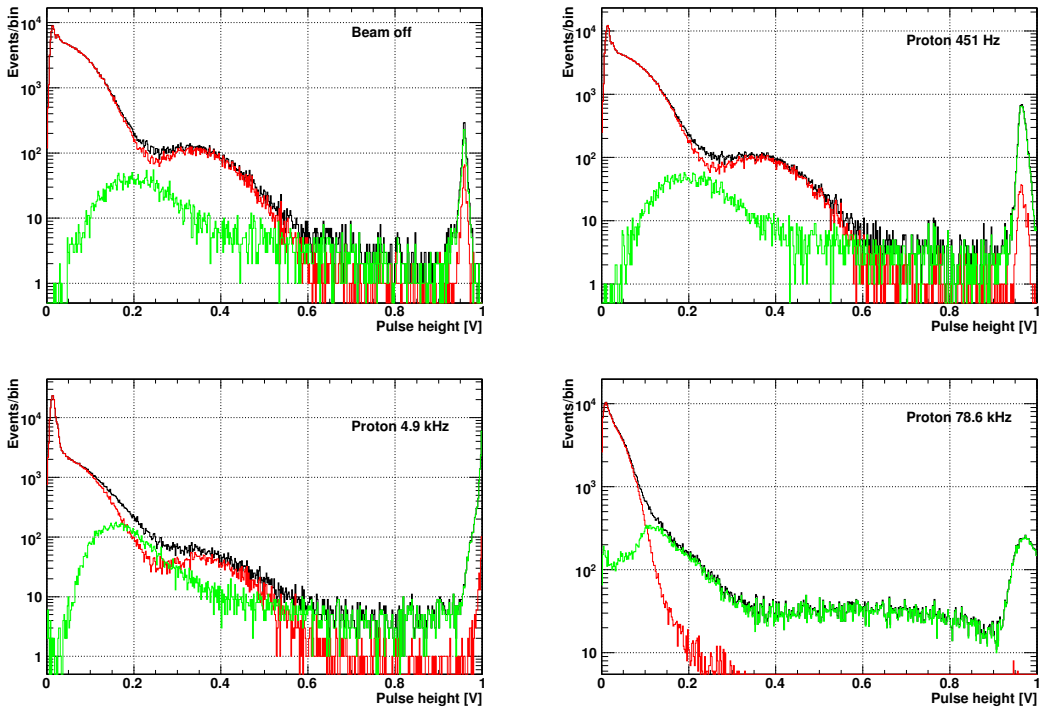

Figure 5.11: Spectra of all events without the selection (black), the fast events (red) and the other events not included in the fast branch (green), for each proton injection rates with configuration (3). Peaks at around 0.35 V are photo-ionization peaks of 59.5 keV gamma-rays, except for the 78.6 kHz irradiation. Hereinafter we take the absolute values of the pulse heights in making spectra.

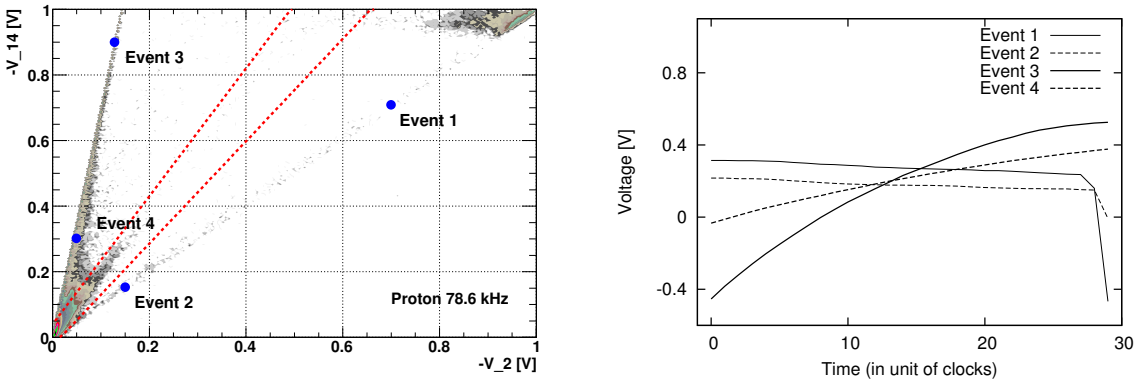

Figure 5.12: Sampled loci in the two-dimensional histogram for the unidentified events (left), and the typical waveforms for each samples (right). The events 1 and 2 seem to rise in the last one or two clocks, while the events 3 and 4 seem to be recovering.

5.3.3 Examination of the unidentified event clusters

We picked up a number of events from the unidentified event clusters in the two-dimensional histograms and checked their waveforms. Figure 5.12 shows the loci of the sampled events on the histograms and the typical waveforms for each loci, for the dataset of 78.6 kHz irradiation. All of them were not triggered as we expected. The events 1 and 2 seemed to rise in the last one or two clocks, while the events 3 and 4 seemed to be recovering. Waveforms of the other events we examined are very similar to each other.

Although the trigger source of these events are not identified, the similarity of the waveforms of a number of events suggests that accidental triggers such as these caused by a single p.e. are not responsible. We also note these 'unexpected events' naturally will not appear in the signal processing of flight electronics, which will be triggered by the input analog signals (CSA output) themselves rather than external logic signals generated by anode outputs of PMTs. Only in this analysis, we apply another criterion to remove the unexpected events.

We found out a criterion for the rejection of the unexpected events. Figure 5.13 shows the waveforms subtracted their baseline followed by the procedure described in the caption of figure 5.9. All of them have minimum voltages at the last (29th) clock. Thus we added a condition of histogramming that a baseline-subtracted waveform does not have minimum at the 29th clock. The revised two-dimensional histograms and spectra are shown in figure 5.14 and 5.15. The clusters of the unexpected events disappear in the two-dimensional histograms. On the other hand, the spectra of the fast events do not change significantly except for 78.6 kHz irradiation. Therefore we concluded the additional condition worked only on the unexpected events.

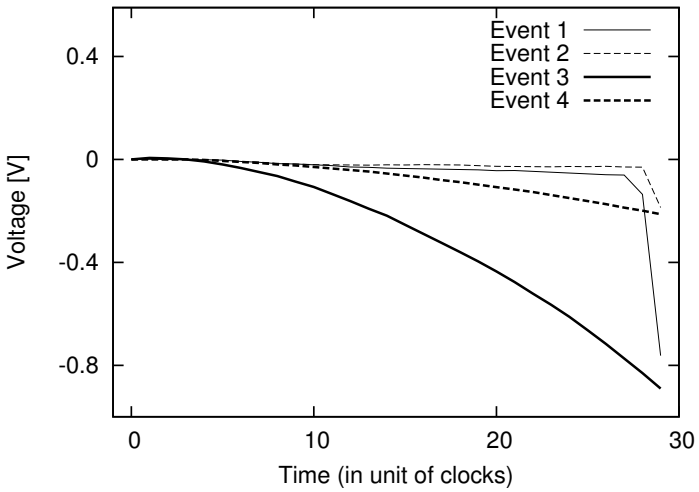

Figure 5.13: Baseline-subtracted waveforms of four events in figure 5.12. All of them have minimum voltages at the last (29th) clock.

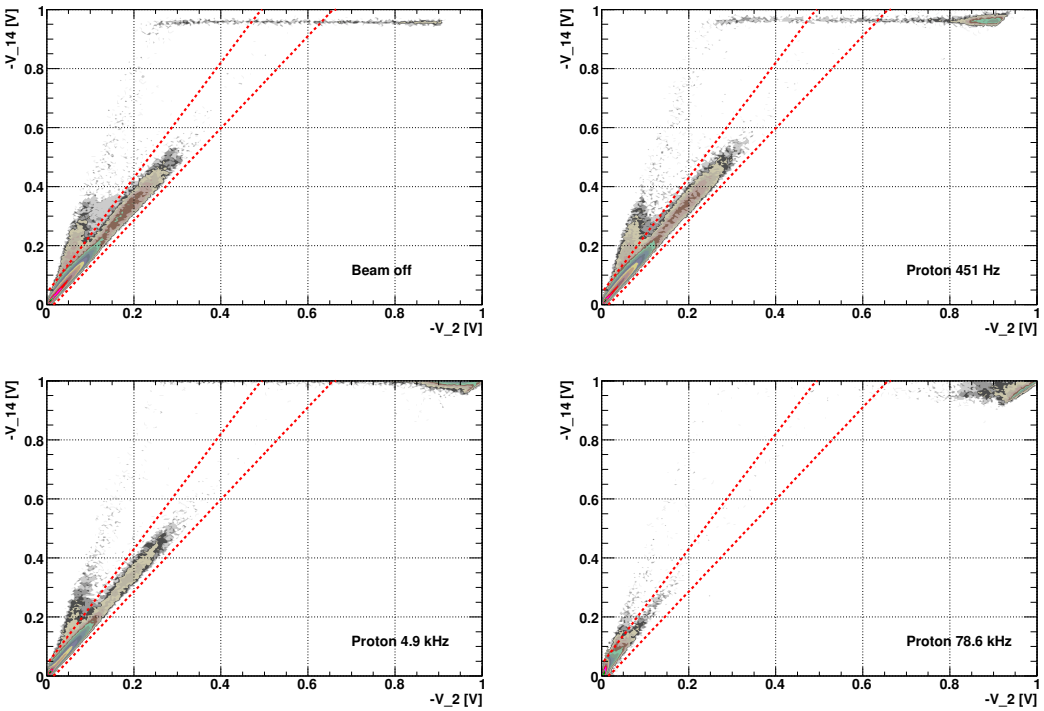

Figure 5.14: The revised two-dimensional histograms. The clusters of the unexpected events have disappeared.

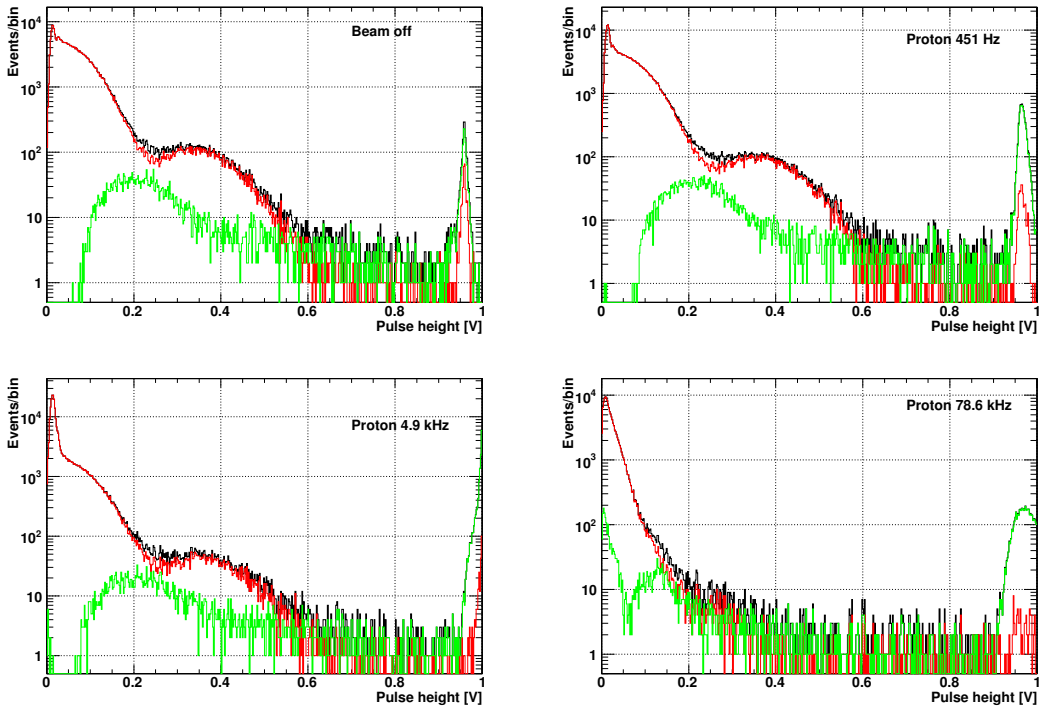

Figure 5.15: The revised spectra. There are no significant changes on the fast events spectra except for 78.6 kHz irradiation.

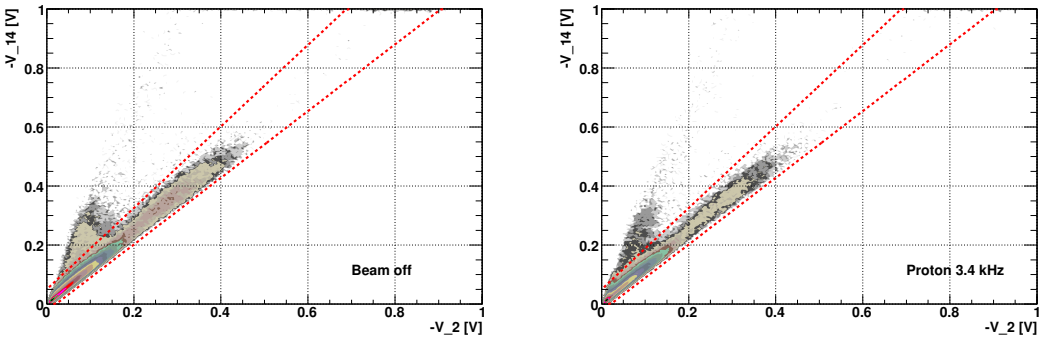

Figure 5.16: Two-dimensional histograms for the data obtained with CP595H. There is no unexpected clusters seen in figure 5.10. Distributions of the fast events differ from those of the v1 board (figure 5.14).

5.3.4 Analysis of data obtained with the setup using CP595H

We applied the same analysis scheme discussed above on the data obtained with CP595H. Figures 5.16 and 5.17 show the two-dimensional histograms and spectra, respectively, for the datasets of beam off and 3.4 kHz beam in configuration (3).

In figure 5.16, we can see fast, slow and saturated events clusters and no unexpected events seen in figure 5.10 are found. On the other hand, distributions of the fast events

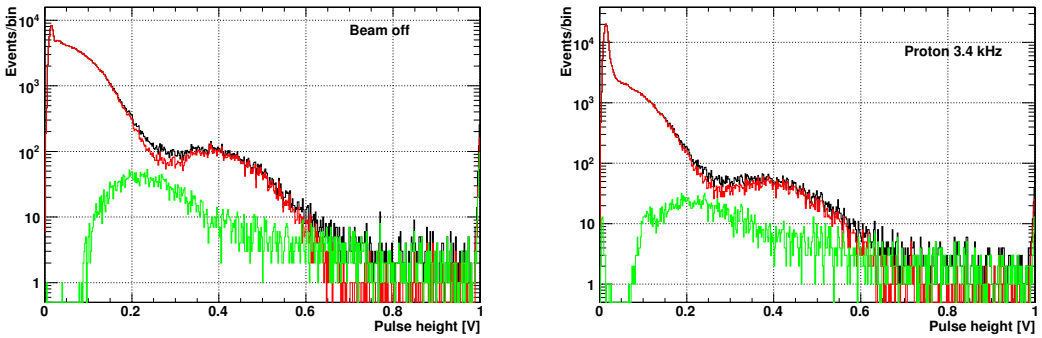

Figure 5.17: Spectra for the data obtained with CP595H. Peaks at around 0.4 V are photo-ionization peaks of 59.5 keV gamma-rays.

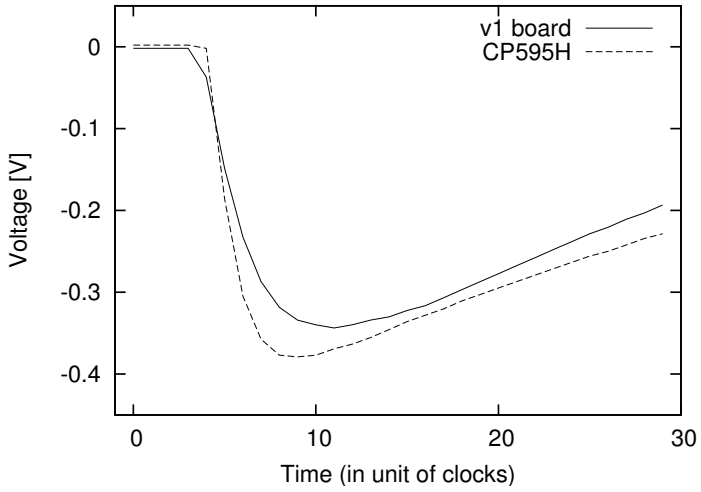

Figure 5.18: Comparison between the waveforms obtained with the v1 board and CP595H. The waveform of CP595H rises more rapidly. This difference affects the distribution of the fast events in the two-dimensional histogram.

clearly differ from those of the v1 board data with smaller inclination. This is explained by the difference of the rise times between v1 board and CP595H. Figure 5.18 compares typical waveforms of 59.5 keV gamma-ray events obtained with v1 board and CP595H. We can see the waveform of CP595H rises more rapidly. The ratios of V_{14}/V_2 are 1.68 and 1.21 for the v1 board and CP595H, respectively, which well agree with the gradient of the fast events clusters in the two-dimensional histograms. Since fall times of the waveforms and the applied analysis algorithm are same, this difference purely reflects the rise time.

In the spectra (figure 5.17), 59.5 keV gamma-rays photo-ionization peaks are clearly seen. The pulse heights are slightly ($\sim +10\%$) larger than those of v1 board. This may be due to an uncertainty of a feedback capacitance in the CSA, which often amounts to $\pm 10\%$.

With the above analysis, CP595H seems to have better separation of the fast events from the slow events. Thus the next tasks are evaluating quantitatively the separation between two kinds of events and optimizing the delay clocks, adopting 2 and 14 in above temporarily.

5.3.5 Optimizing the delay clocks

The optimal values of delay clocks for PSD, which minimize the contamination of the slow signals in the fast signals, are nontrivial. We used 2 and 14 clocks in the above analysis, but they lacked quantitative bases. Thus we tried to optimize the delay clocks before discussion on ^{241}Am spectra.

At first, we made a number of histograms to get indications of the region to search the optimal values of the delay clocks. Let us define a 'fast delay' f as the smaller delay clock among the two clock values, and a 'slow delay' s as the larger one, hence the above analysis adopted $f = 2$ and $s = 14$. We made histograms of V_s/V_f (the 'gradient' in the two-dimensional histograms) with various pairs of f and s, where V_s and V_f are minimum voltages of the differential waveforms with s and f, respectively. Room background data were used in this analysis because the data with Am irradiation had fewer slow signals. We used the energy band of 15−20 keV. Figure 5.19 is an example of the histograms drawn with the v1 board and $f = 2$ clocks. All of the histograms are shown in appendix B.2. We determined the search region as $f = 1$−3 and $s = 8$−28 based on those histograms.

Next, we evaluated the contamination. The distributions in the V_s/V_f space are modeled by two Gaussian functions

$$f(x) = N_f F_{G,f}(x, \mu_f, \sigma_f) + N_s F_{G,s}(x, \mu_s, \sigma_s),$$

where $x = V_s/V_f$, $F_G(x, \mu, \sigma)$ is a normalized Gaussian distribution with a mean μ and a standard deviation σ, and N is a normalization factor. The contamination ratio, R, is defined by

$$R = \int_{\mu_f - 3\sigma_f}^{\mu_f + 3\sigma_f} F_{G,s}(x, \mu_s, \sigma_s).$$

In addition to the 15−20 keV band, we also dealt with the 20−30 keV band in order to examine whether changes of contamination ratios differ with the energies or not. We used bins with ≥ 20 events in fitting, where the histograms were binned with $\Delta(V_s/V_f) = 0.1$ for $f = 1$ and $\Delta(V_s/V_f) = 0.05$ for $f = 2$ and 3.

The result of the calculation is shown in figure 5.20. Contaminations with $f = 2$ is smaller than or same as those with $f = 1$ or 3 in all situations. It looks like $s = 16$ and $s = 18$ are best for the 15−20 keV and 20−30 keV bands, respectively, when $f = 2$. We

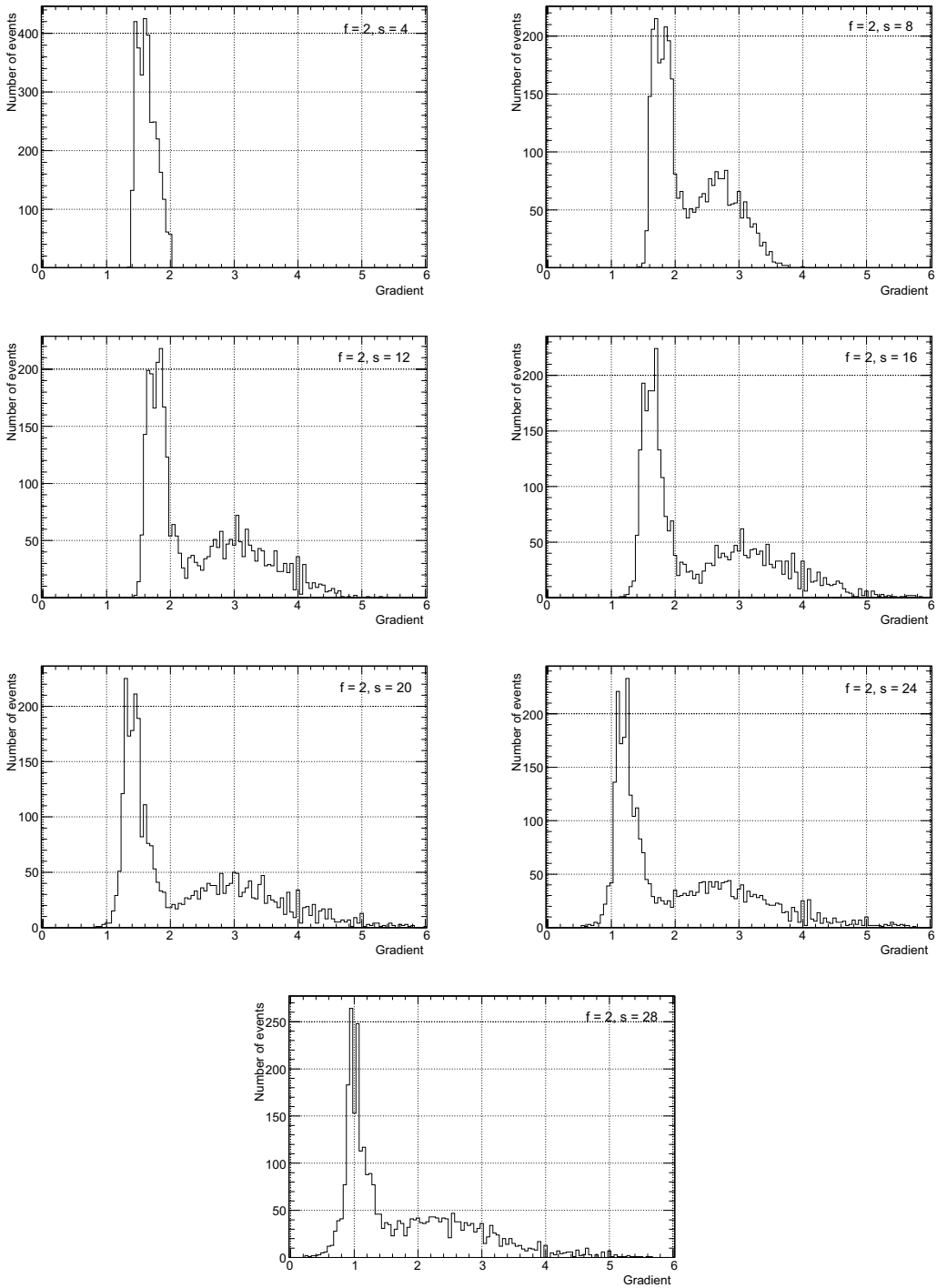

Figure 5.19: An example of the distributions of the fast and slow signals in the 15−20 keV band on the V_s/V_f ('gradient') space with the dataset of the v1 board when $f = 2$. The sharp peaks on the left side are the fast events and the wide peaks on the right side are the slow events. They merge completely when $s = 4$. We can see the optimal s may be ~ 16.

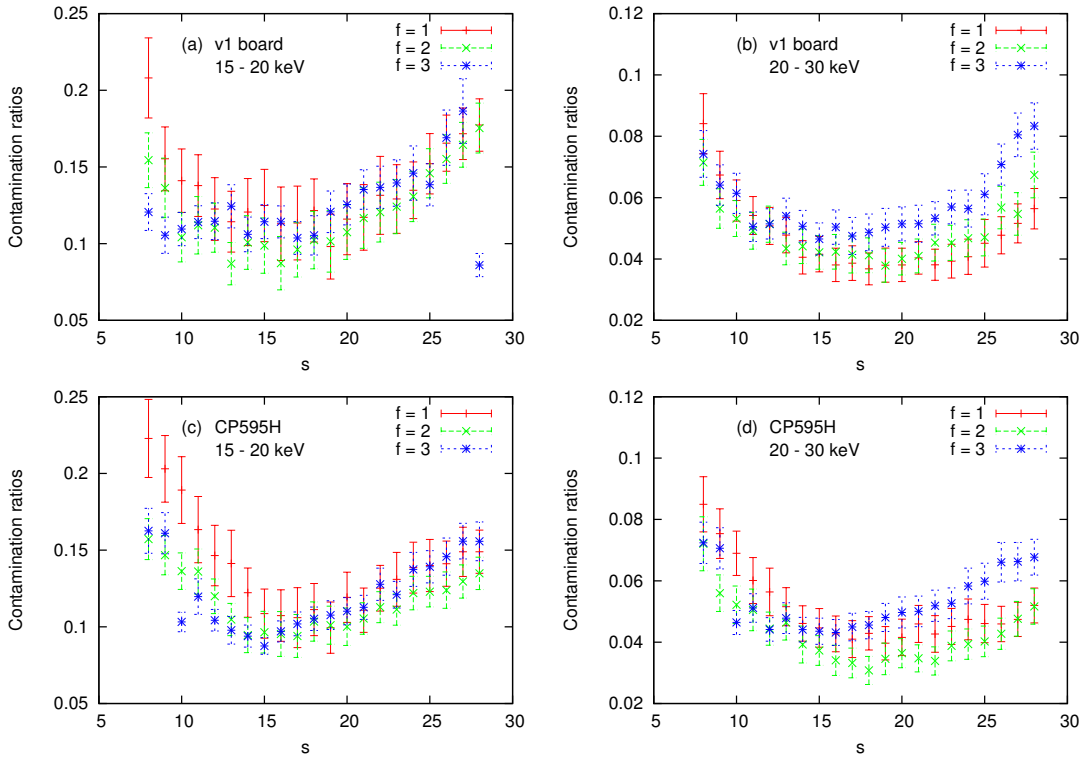

Figure 5.20: Changes of contamination ratios with f and s. (a) v1 board in the 15−20 keV band, (b) v1 board in the 20−30 keV band, (c) CP595H in the 15−20 keV band, (d) CP595H in the 20−30 keV band. The optimum is $f = 2$ for all cases. Contaminations with $f = 2$ is smaller than or same as those with $f = 1$ and 3 in all cases. $s = 16$ and $s = 18$ are best for 15−20 keV and 20−30 keV, respectively, when $f = 2$.

suppose $s = 16$ is better for use because it makes less contamination in the lower energy region. Since the contamination ratios change slowly with s around the optimal values, the condition of the optimization will not affect PSD significantly.

The minimum contamination ratios are compared for the v1 board and CP595H. They are obviously consistent in the 15−20 keV band while in the 20−30 keV band CP595H seems to be slightly better than the v1 board. We found the systematic difference of the contamination ratios of the v1 board and CP595H to be $(9 \pm 4) \times 10^{-3}$, which was evaluated as the residual of the mean of the values at $s = 15, 16$ and 17. This suggests the shorter rise time of CP595H provides the better separation of fast and slow signals. The rise times of fast signals with both the v1 board and CP595H ($\sim$ 200 ns) is much longer than the timescale of the PMT output signals of fast events ($\sim$ 20 ns). We suppose the rise time is limited by the circuit's response, mainly its slew rate. We are planning to introduce faster CSA system and evaluate the contamination of slow signals.

We considered what determines these optimal values. Though there is a complicated

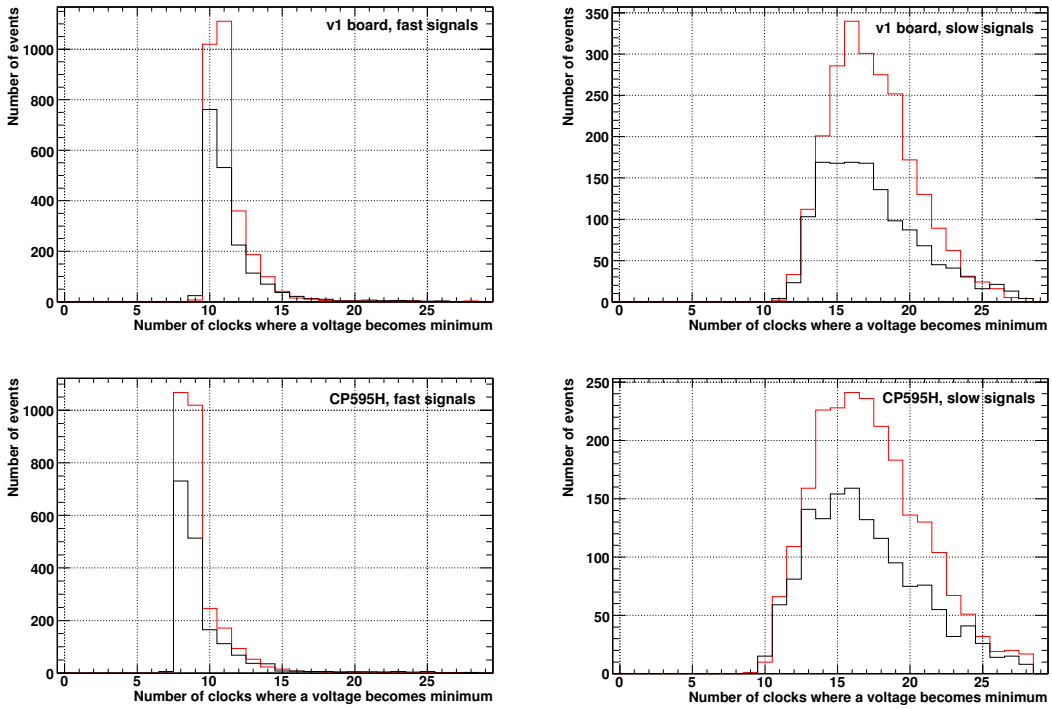

Figure 5.21: The distributions of the number of clocks where a voltage becomes minimum, for the fast and slow signals. Black and red histograms are for 15−20 keV and 20−30 keV band, respectively. The optimal $s = 16$ and 18 may reflect almost directly this peak positions. On the other hand, we cannot find any relations between the optimal f and the peak positions of fast signals.

origin, we suppose it is related with the peak position of the waveform. Figure 5.21 shows the distributions of the number of clocks where a voltage becomes minimum. The distributions of slow signals have peaks at the 16th clocks. The optimal $s = 16$ and 18 may reflect almost directly this peak positions. On the other hand, we cannot find any relations between the optimal f and the peak positions of fast signals.

We tried to reproduce the trend of the changes of contamination ratios presented in figure 5.20 using the fast and slow signals shown in figure 5.8. We adopt the value of

$$\frac{1}{(V_s/V_f)_{\rm slow} - (V_s/V_f)_{\rm fast}} \quad \left(= \frac{1}{\rm residual}\right)$$

as the proxy for a contamination ratio. Figure 5.22 shows changes of V_s/V_f with f under fixed $s = 18$ and with s under fixed $f = 2$. Changes of this proxy contamination ratios with f and s are shown in figure 5.23. The s dependency is similar to the trend of figure 5.20. The f dependency is inconsistent with the experimental result of the optimum $f = 2$. However, this is a very simple simulation using only one pair of the fast and slow waveforms, and other factors like fluctuations of rise times would affect the contamination.

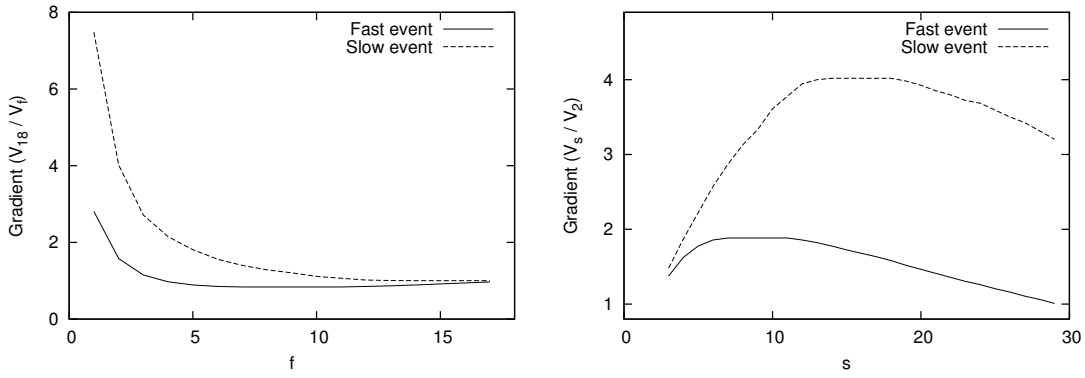

Figure 5.22: The change of V_s/V_f with f under fixed $s = 18$ (left) and that with s under fixed $f = 2$ (right), for the fast and slow signals shown in figure 5.8.

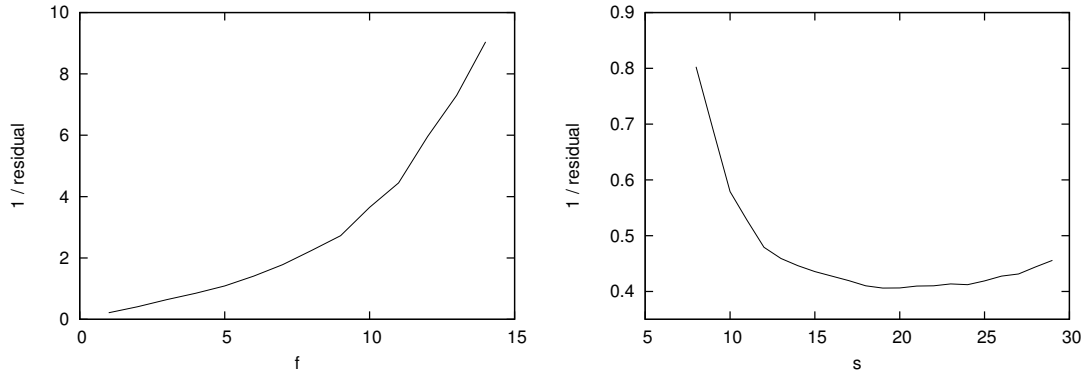

Figure 5.23: The change of the proxy contamination ratios with f under fixed $s = 18$ (left) and that with s under fixed $f = 2$ (right), for the fast and slow signals shown in figure 5.8. The s dependency is similar to the trend of figure 5.20. The f dependency is inconsistent with the experimental result of the optimum $f = 2$.

5.3.6 Variations of the gain and the energy resolution with the proton rates

We examine how the gain and energy resolution of the photo-ionization peak at 59.5 keV vary with the incident proton flux. We fitted 59.5 keV photo-ionization peaks by a function of Gaussian and a background continuum, $C_1 \exp[-C_2/(x - C_3)]$, where every C is a constant. The peak voltages were iteratively derived since the energy of the fitting region, 31−84 keV in this analysis, was calibrated only with the 59.5 keV photo-ionization peak. Data of $\sim$ 10 kHz proton irradiation was not be able to be fitted because there were no photo-ionization peaks as shown in 5.15 (bottom right panel). The results, changes of gain and energy resolution at 59.5 keV with the proton rate, are shown in figure 5.24. Relative gain is defined as a ratio of the 59.5 keV peak voltage to that for the beam off data.

The gain for the v1 board increased by $\leq 6\%$ and that of CP595H fluctuated within $\sim \pm 1\%$. Because both of the energy deposit and the light yield are different for the three irradiation configurations, the gain dependence on the proton flux rate were not the same. We therefore plotted the measured gain as a function of the anode current as shown in figure 5.25. We assumed the light yield of the fast, BGO ans slow scintillators were 0.40, 0.24 and 0.04 p.e./keV,[4] respectively, and the anode gain of the PMT was 3.3×10^6. In this figure, we can see a clear correlation between the gain shift and the anode current for the v1 board. The gain of CP595H, however, does not have large deviation from unity for all of the points. The reason for this difference between the current dependencies is not clear. The particle background level in PoGOLite experiment corresponds to the anode current of < 5.5 μA. A gain variation of $< 6\%$ is expected in such a background level, based on this experimental result. Furthermore we confirmed that the gain variation is no larger even with the background anode current higher by a factor of 10. Since the gain variation is significantly smaller than the energy resolution at 59.5 keV, this effect is not important in a flight experiment.

We also evaluated the variation of the energy resolution due to the change in the proton rate in figure 5.24. We did not find significant gain variation due to the proton rate, although there is a sign of poorer resolution at high proton fluxes in a few cases.

[4] The value for the fast scintillator was derived from the data of this experiment. For BGO and slow scintillators, the value was scaled with previous results [56].

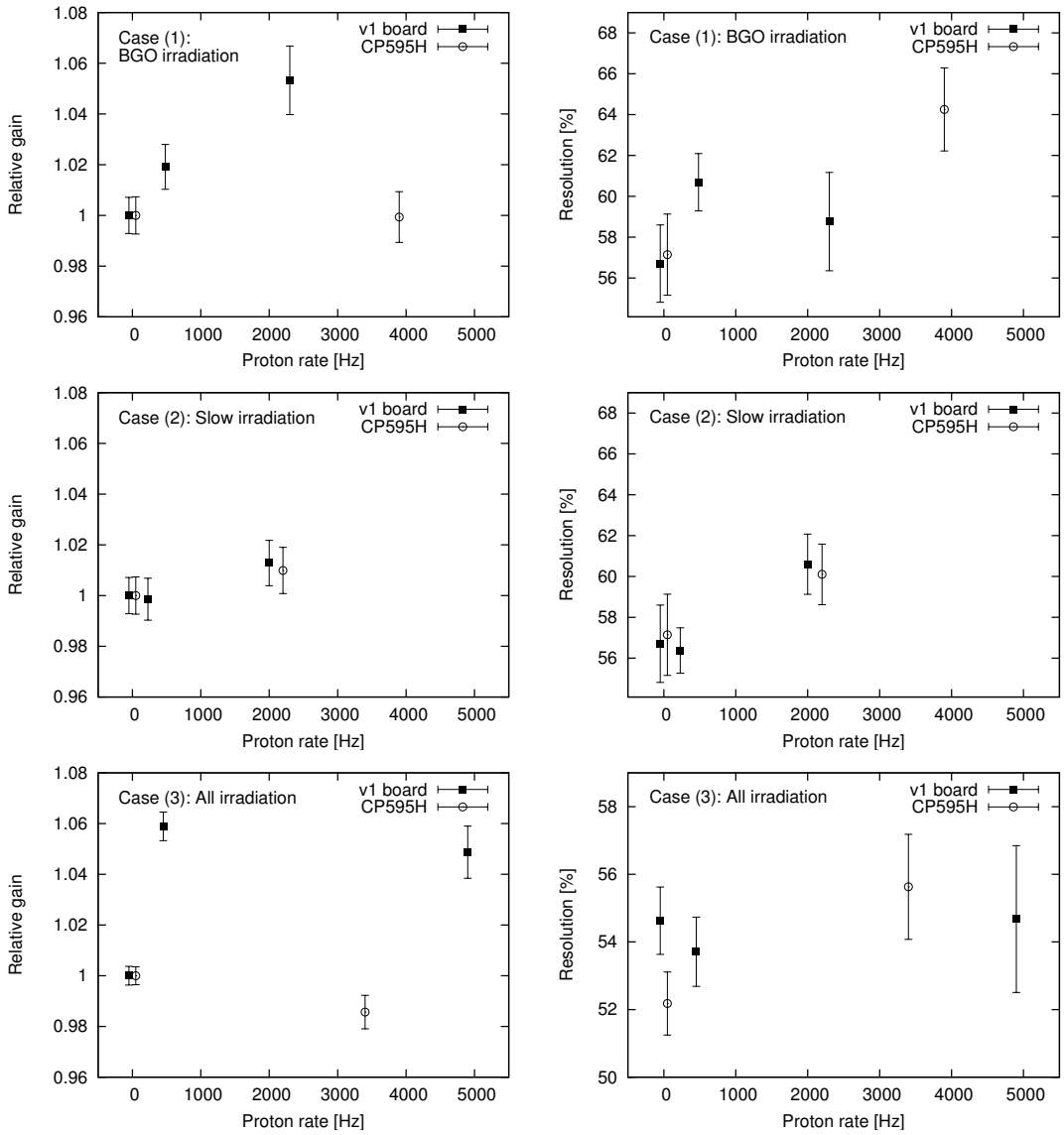

Figure 5.24: Changes of gain (left) and energy resolution at 59.5 keV (right) with the proton rate for three irradiation configurations, configuration (1) (top), (2) (middle) and (3) (bottom). The points of 0 Hz are slightly shifted to prevent the overlap of the data points of the v1 board and CP595H. Energy resolutions cannot be compared between configurations (1)/(2) and (3) because the conditions of the optical connection between PDC and the PMT differ. The gain increased by $\leq 6\%$ for the v1 board and fluctuated between $\sim \pm 1\%$ for CP595H. There is no significant variation of the energy resolution.

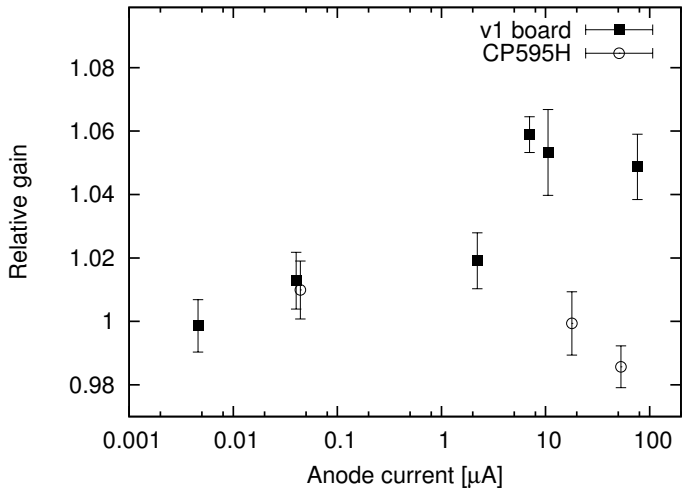

Figure 5.25: A gain shift with an anode current. A positive correlation is seen for the v1 board but not for CP595H. The particle background level in a flight corresponds to the anode current of < 5.5 μA with the condition of this experiment. A gain variation of $\leq 6\%$ is expected in such a background level.

5.3.7 Comparison between the two pulse shape discrimination methods

Finally, we analyzed the data obtained with the double integration method. We have already shown the way of analysis in §4.2.

First, we drew two-dimensional histograms with the axes of the output voltages of the fast shaper and the slow shaper (figure 5.26). Since there were pile-up events of 59.5 keV gamma-rays in figure 5.26, the fast regions were taken widely although the region should be as narrow as that shown in figure 4.5. Next, the 'fast events' (the events detected in the fast scintillator) were selected and spectra of total, fast and the other events were drawn as figure 5.27. The spectral energy distributions are similar to those obtained with the waveform analyzer (figure 5.15).

Changes of the gain and the energy resolution were compared to the results with the waveform analyzer. The new data point obtained with the VME DAQ system (figure 5.4) is plotted in figure 5.28 left together with the data obtained with the waveform analyzer shown in figure 5.25. The increase of gain measured with the VME DAQ system is 10%, which is higher by a factor of two than the data taken with the waveform analyzer. The behavior of these three electronics systems are significantly different. A further study is needed to understand this difference. Nevertheless, the energy resolution obtained with the VME DAQ is stable and the mean value is consistent with that obtained with the setup of the v1 board and the waveform analyzer.

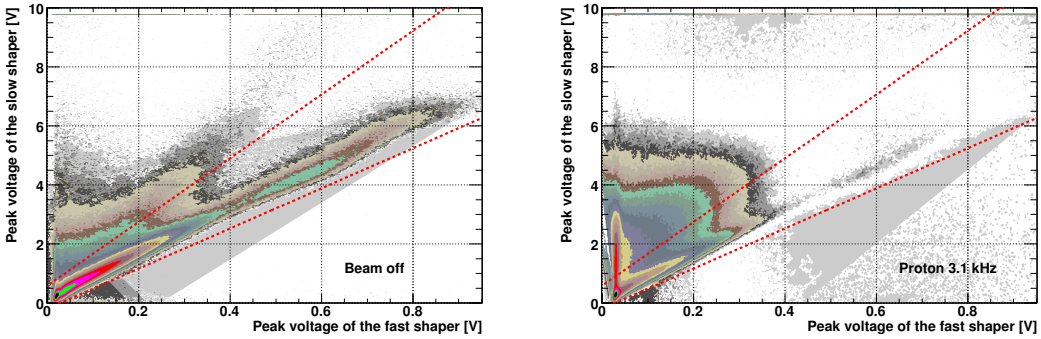

Figure 5.26: Two-dimensional histograms obtained with VME DAQ in configuration (3) for beam off and on. Dashed regions represent fast branches. Clusters with the centers at around (0.6, 4.5) are 59.5 keV gamma-ray events and their pile-up events spread longitudinally upward from the clusters. Geometric patterns (triangles and stripes) are artifacts created in binning with ROOT.

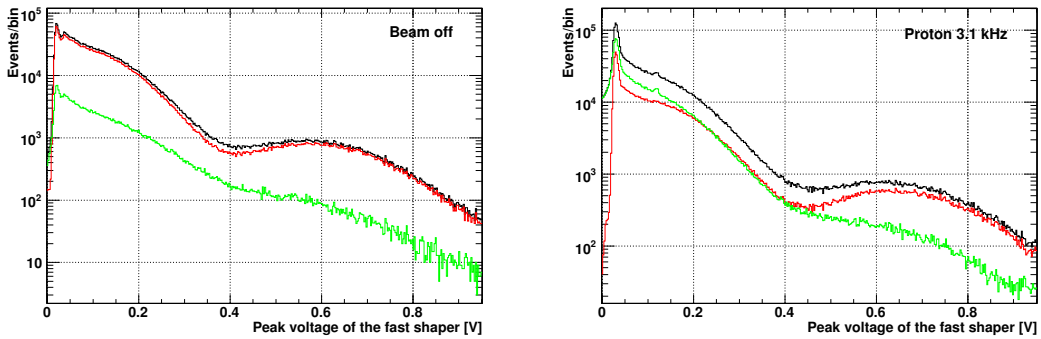

Figure 5.27: Spectra of all events (black), fast events (red) and the other events not included in the fast spectrum (green) obtained with the VME DAQ in configuration (3) for beam off and on. Peaks at around 0.6 V are photo-ionization peaks of 59.5 keV gamma-rays.

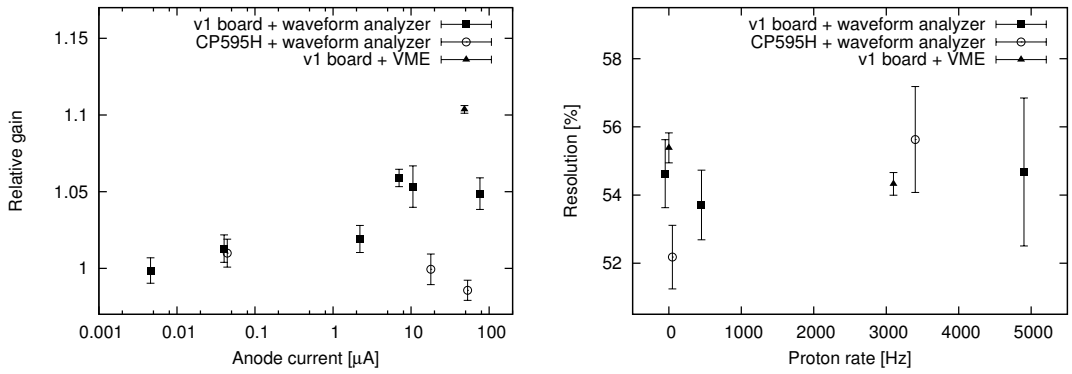

Figure 5.28: Comparison between the data obtained with the VME DAQ and with the waveform analyzer. Changes of a gain with an anode current (left) and an energy resolution for only configuration (3) (right) are shown.

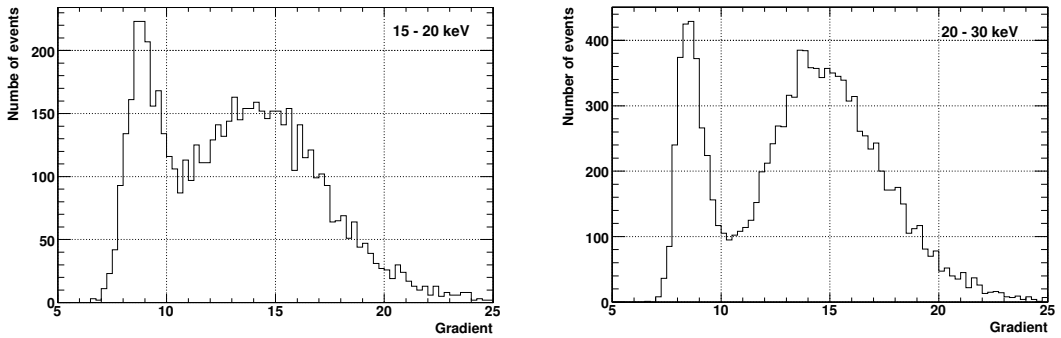

Figure 5.29: The distributions of the fast and slow signals in the energy range of 15−20 keV (left) and 20−30 keV (right) on the gradient space with the data obtained with the VME DAQ. The sharp peaks on the left side are fast events and the wide peaks on the right side are slow events.

Contaminations of the slow signals to the fast signals are compared to those of the waveform analyzer using the room background data. The evaluation method is same as that used for the data obtained with the waveform analyzer. We selected the energy bands of 15−20 and 20−30 keV with the output voltages of the fast shaper, and fitted distributions of the 'gradient' on two-dimensional histograms (output voltage of the slow shaper divided by that of the fast shaper, in this case) with two Gaussian functions. The derived contamination ratios are shown in table 5.2. The value for 15−20 keV is significantly larger than that obtained with the waveform analyzer, while consistent for 20−30 keV. This result shows the PSD method with the waveform analyzer provides better separation between the fast and slow events than that with the double integration method.

Table 5.2: The comparison of the contamination ratios between two electronic setups using the v1 board as a CSA. The values for the readout by the waveform analyzer is for the delay clocks of $f = 2$ and $s = 16$.

Energy [keV]	Contamination ratio	
	waveform analyzer	shaping amplifiers + ADCs
15−20	0.09 ± 0.02	0.16 ± 0.01
20−30	0.042 ± 0.006	0.048 ± 0.003

5.4 Summary

We performed a proton beam test of a PDC and a flight-model PMT with three electronics setups, a waveform analyzer with our PoGOLite version 1 board (v1 board) or a ready-made CSA CP595H, and VME ADCs with the v1 board. Results of this experiment are summarized as below.

1. Both CSAs recover within 100 μs from large output signals of proton events depositing $\sim$ 100 MeV.

2. A viable PSD method using differences of the rise times of the CSA output has been proposed. It works well for both CSAs.

3. After optimizing the condition of PSD, contaminations of the 'slow events' in the 'fast events' have been evaluated. CP595H has less contamination in the 20−30 keV band. This suggests a faster amplifier provides smaller contamination.

4. Changes of gains of a PMT and energy resolution at 59.5 keV with proton rates have been examined. The gain increased by $< 6\%$ with the v1 board and varied within $\pm 1\%$ with CP595H. Energy resolution tended to get worse as the proton rate increased. The fractional gain shift is smaller than the energy resolution by $\sim 1/10$ even with the anode current due to background events an order of magnitude larger than that expected in a balloon flight. Our PDCs and PMTs will work properly in the radiation environment of a balloon experiment.

5. The gain shift due to the anode current with VME ADCs was $\sim +10\%$ while the energy resolution did not change and was consistent with the value obtained with the setup of the waveform analyzer. Contamination of the slow events is larger than that for the waveform analyzer in 15−20 keV band. The waveform analyzer method for PSD is advantageous for our experiment for two reasons: the electronics simplicity and the more efficient separation of fast events from slow events.

Chapter 6

Conclusions

In this thesis we have conducted three experiments; acceptance tests of the photomultiplier tube assemblies (PMT-ASSYs) we developed, a polarized photon beam test of a 7-unit prototype polarimeter using a first flight-model Phoswich Detector Cell (PDC) and a proton beam test of a PDC.

We have developed efficient procedures for the acceptance test and also performed the tests for 53 PMT-ASSYs. Most of them except for 4 PMT-ASSYs, which have a high noise level, work properly. First, the bias voltage dependency on the gain is expressed by a power-law function between +950 V and +1250 V. Variations of the gains and the index numbers of the power-law are so small that the gain variation can be canceled out with the bias voltage. Secondly, the power consumption is 260 mW per PMT-ASSY on average with the bias voltage of +1100 V. The whole PoGOLite polarimeter will consume $\sim$ 70 W. Thirdly, the diode cramping, which is one of the measures to large output current, works properly for a bright LED emission. Fourth, the noise is typically 0.025 photoelectrons, which is so low to allow single photoelectron signals to be read out. Fifth, concerning the temperature environment, most of the PMT-ASSYs work with the temperatures of between -30°C and +30°C, and do not crack. We will continue the acceptance tests.

In the photon beam test, the count rate with each peripheral units have modulated with the azimuth rotation angle clearly. The derived modulation factors for a full polarization is 34.4%, 35.8% and 37.2% for the incident 30, 50 and 70 keV beam, respectively. These values are consistent within a $\sim$ 10% accuracy with those obtained with a Monte Carlo simulation using the Geant4. In addition, the measured detection efficiencies agree with the simulation within a 10% accuracy. Difference between the experiment and the simulation is a subject to be studied.

In the proton beam test, we have irradiated a PDC with a 392 MeV proton beam at the rate expected in a balloon flight. First, a large output signal due to a 100 MeV

energy deposit can recover to the baseline level within 100μs using the bleeder circuit we developed. Next, we have proposed a new pulse shape discrimination (PSD) method using a rising waveform of a charge sensitive amplifier (CSA) output. We also have confirmed a faster CSA creates a better separation of 'fast events' (the events detected in the fast scintillator) from 'slow events' (the events detected in the active shield detectors). Furthermore an well-established PSD method using two kinds of shaping amplifiers results in worse separation between them. This result as well as the electronic simplicity makes the waveform PSD method suitable for on-board signal processing. Finally, the fractional gain shift of the PMT due to the background signals is smaller than the energy resolution when the proton flux simulates the background event rate in flight. However, the gain shift with the proton rate differs among the readout electronics systems. A further study is necessary.

Appendix A

Calibration of the beam polarization at KEK-PF BL14A

We briefly describe the measurement and the simulation for calibrating the beam polarization. Reports by Yamamoto [60] and Mizuno [61] are summarized.

We used a polarization monitor consisted of a small cylindrical plastic scintillator (2.5 cm ϕ and 2 cm thick) glued to a PoGOLite PMT (Hamamatsu R7899EGKNP) and a small CdTe (cadmium telluride) detector ($1.8 \times 2.0 \times 2.0$ mm crystal, Clear Pulse 181820). The monitor is shown in figure A.1. The plastic scintillator and the CdTe detector were mounted on a turntable. The rotation axis of the table was aligned with the beam axis. The plastic scintillator was placed at the center of the table, and the CdTe detector was placed 4 cm away from the plastic scintillator. When the table was rotated, the CdTe detector moved around the plastic scintillator scatterer in an azimuthal range of 180° with 15° steps. The DAQ system for this measurement is shown in figure A.2. The system was triggered by the coincidence signals of the PMT and the CdTe detector.

We examined the modulations of the Compton-scattered event rate normalized by the beam injection rate with the rotation angles. $M_{\rm obs}$ of 0.795 ± 0.006, 0.816 ± 0.006 and 0.816 ± 0.005 were derived for 30, 50 and 70 keV, respectively. We simulated the modulation factor for the polarization monitor with Geant4. The derived M_{100} were 0.878 ± 0.004, 0.887 ± 0.004 and 0.893 ± 0.004 for 30, 50 and 70 keV, respectively. Thus the beam polarization P was derived as 0.91 ± 0.01, 0.92 ± 0.01 and 0.91 ± 0.01 for 30, 50 and 70 keV, respectively.

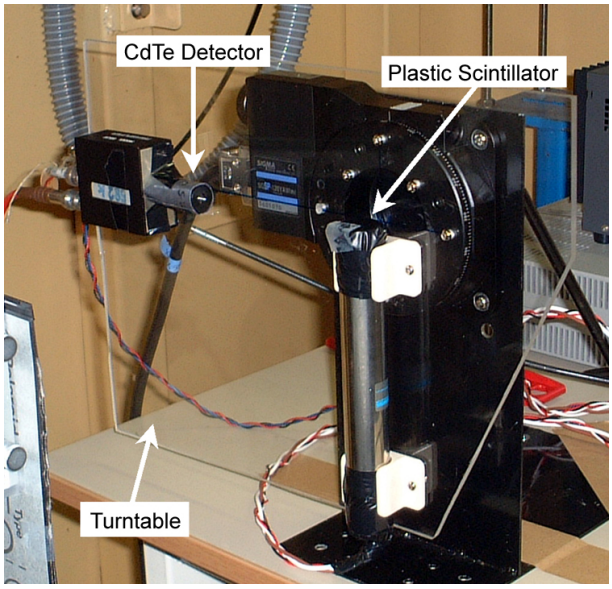

Figure A.1: A photograph of the calibration polarimeter. To shorten the measurement time, the CdTe detector was closer to the plastic scintillator (4 cm away) during the measurement.

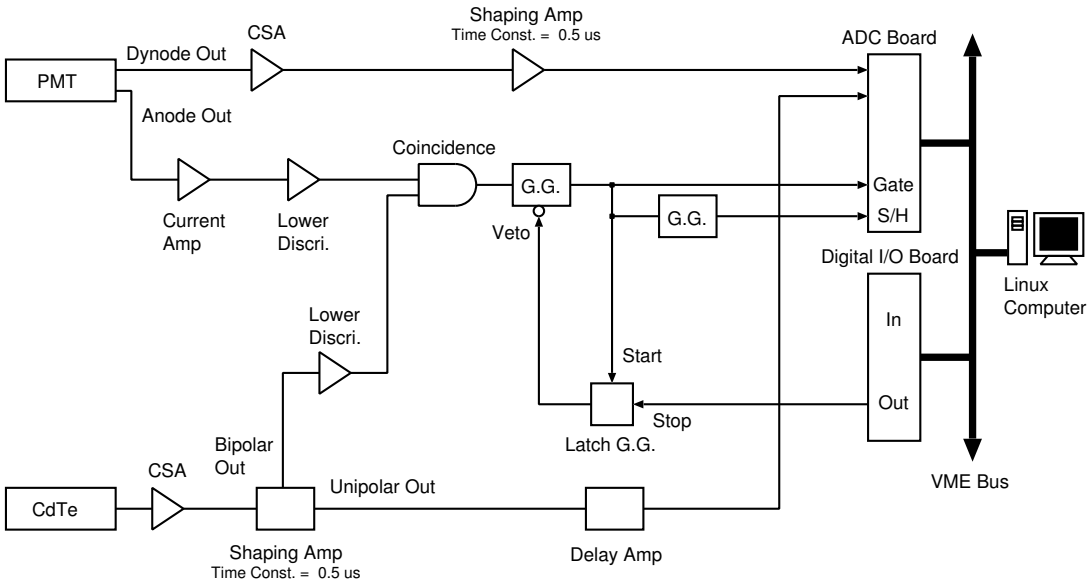

Figure A.2: The DAQ system for the calibration polarimeter. 'G.G.' means a gate generator and 'S/H' means a sample hold input.

Appendix B

Supplements for pulse shape discrimination utilizing waveforms

B.1 Baseline subtraction

We show a model of a baseline subtraction in the PSD method using the waveforms (§5.3.2). If we assume the total output waveform $f(x)$ is the addition of a signal $h(x)$ and a linear baseline $(ax + b)$, where x is the number of the clocks and a and b are constant values. The subtraction of the 2-clock-delayed waveform from the original waveform is described as

$$f(x) - f(x-2) \;=\; [h(x) + ax + b] - [h(x-2) + a(x-2) + b] \;=\; h(x) - h(x-2) + \underline{2a}$$

and that for the 14-clock-delayed waveform is

$$f(x) - f(x-14) \;=\; [h(x) + ax + b] - [h(x-14) + a(x-14) + b] \;=\; h(x) - h(x-14) + \underline{14a}.$$

Thus the offset voltage for the 14 clocks delay is $14/2 = 7$ times larger than that for the 2 clocks delay.

B.2 Separation between fast and slow events

All histograms made for the optimization of the delay clocks in §5.3.5 are shown here. We drew these histograms for the data obtained with the two setups using the v1 board and CP595H. The delay clocks is changed in $f = 1-3$ and $s = 4-28$. The optimal s seems to be ~ 16 for each setups and for each f. The separation do not vary with f significantly and the fast and slow signals merge completely for $s = 4$ regardless of a f. Therefore, we determined the search region as $f = 1-3$ and $s = 8-28$ based on these histograms.

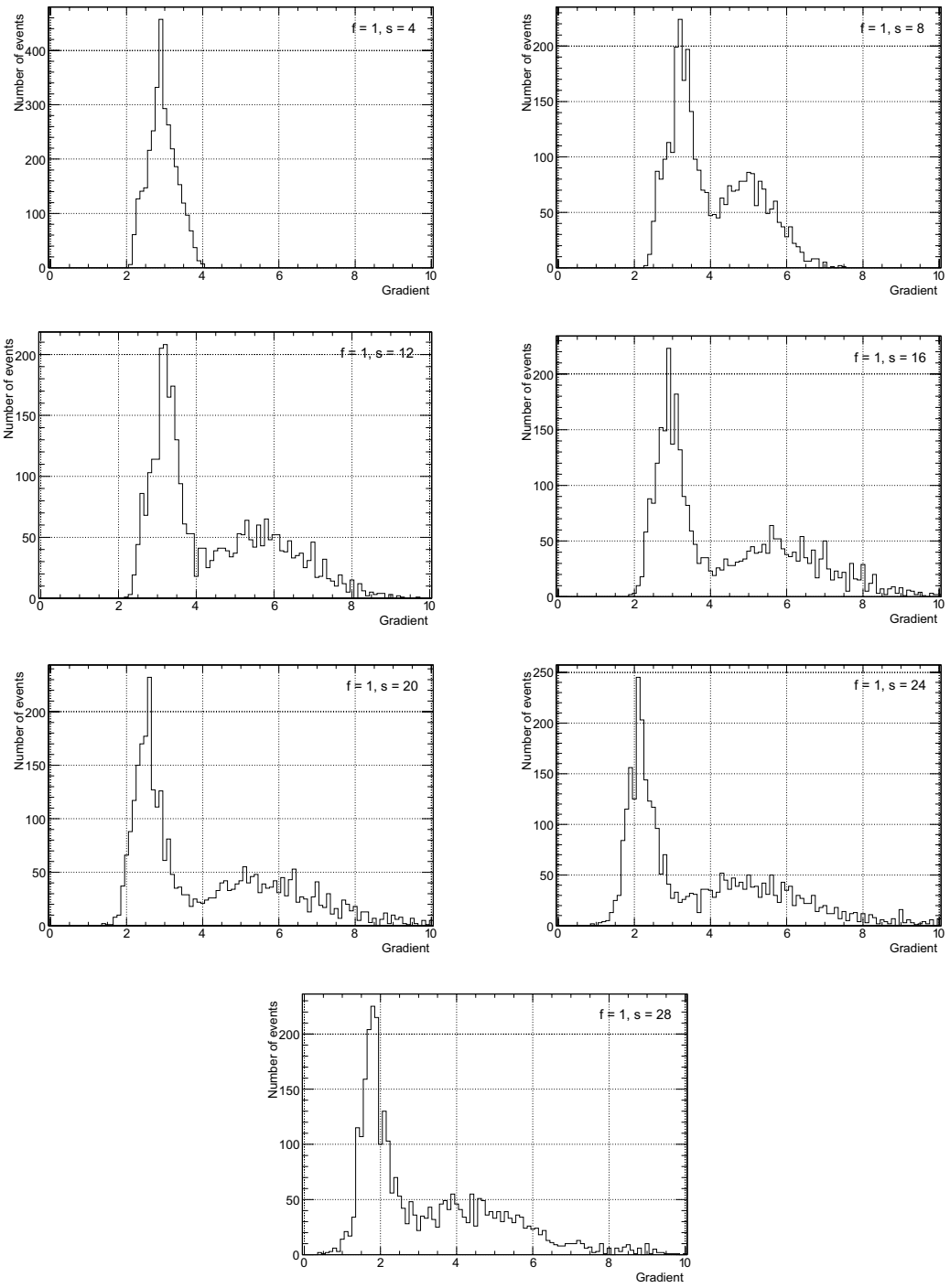

Figure B.1: The distributions of the fast and slow signals in the 15−20 keV band on the V_s/V_f ('gradient') space with the dataset of v1 board when $f = 1$. The sharp peaks on the left side are fast events and the wide peaks on the right side are slow events. They merge completely when $s = 4$. We can see the optimal s may be ~ 16.

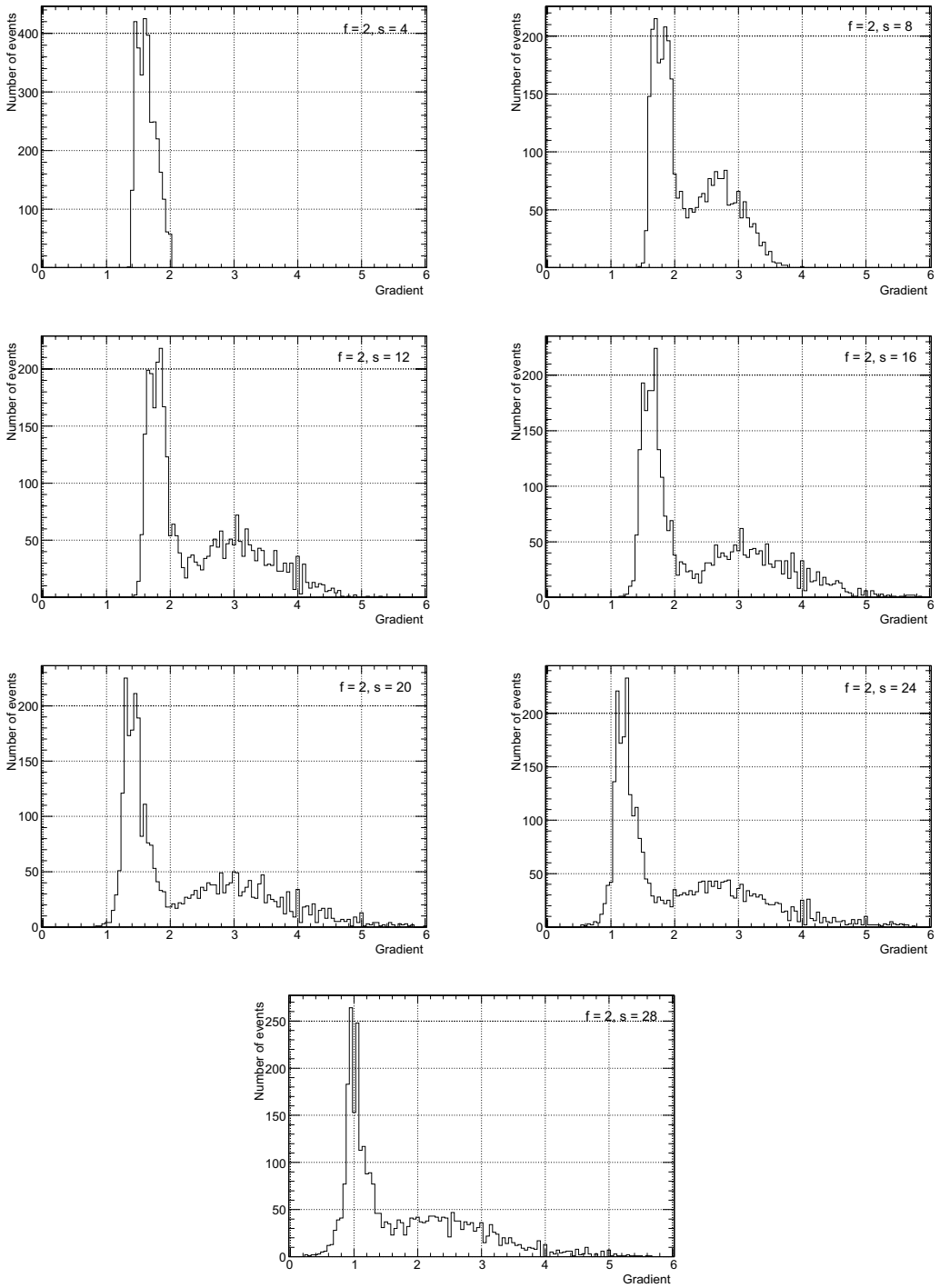

Figure B.2: Same as figure B.1, but for $f = 2$.

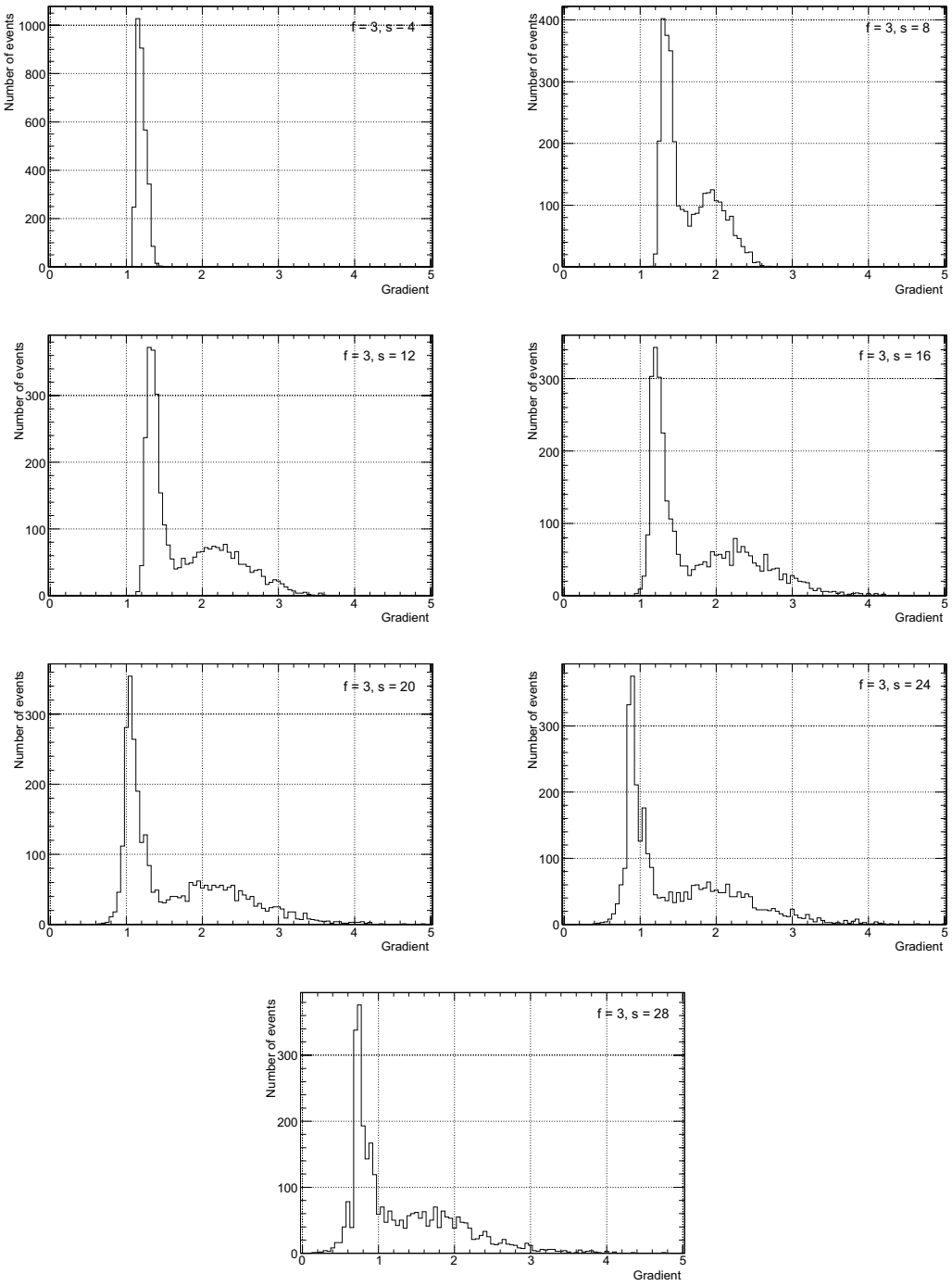

Figure B.3: Same as figure B.1, but for $f = 3$.

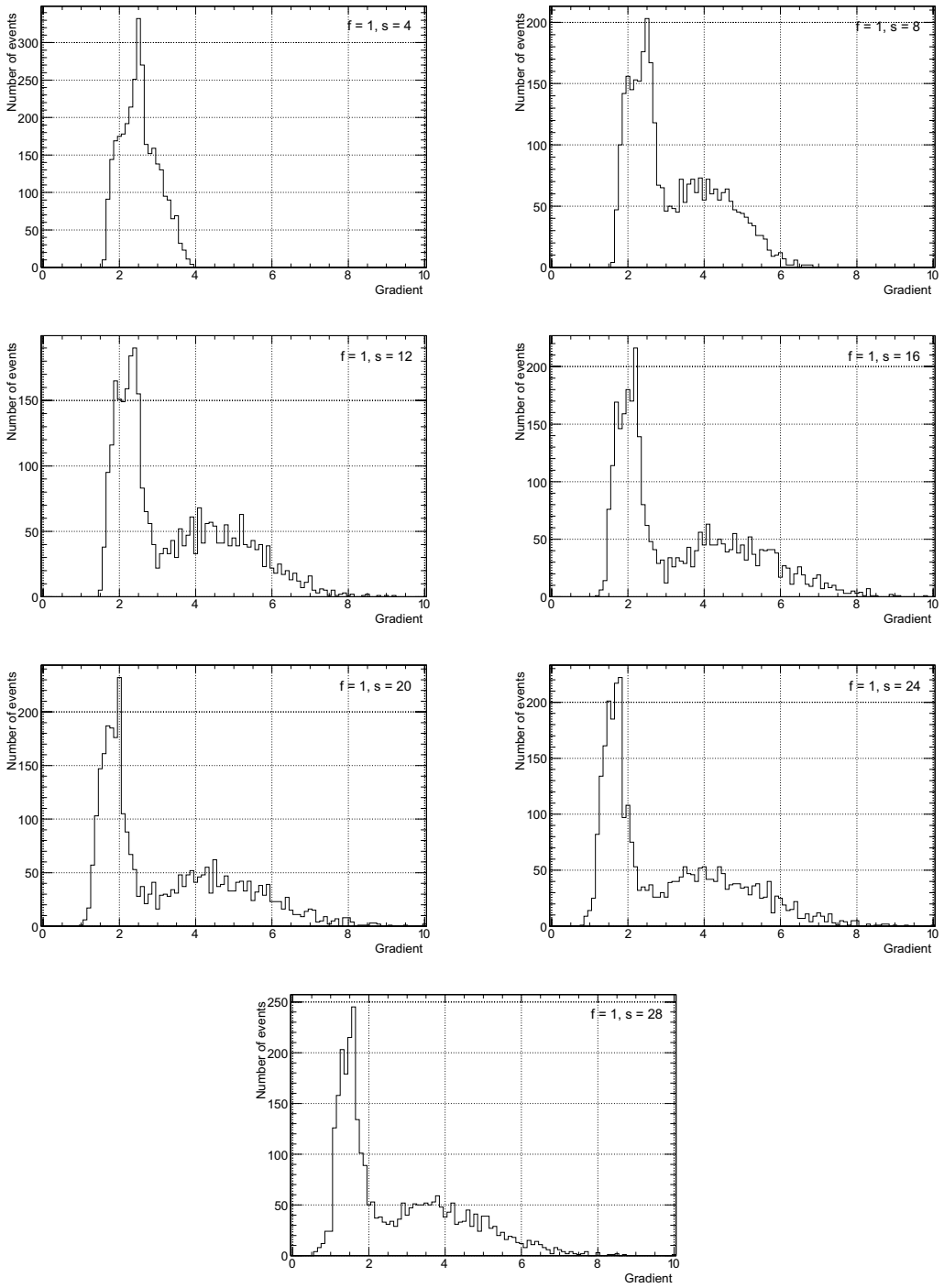

Figure B.4: Same as figure B.1, but for CP595H and $f = 1$.

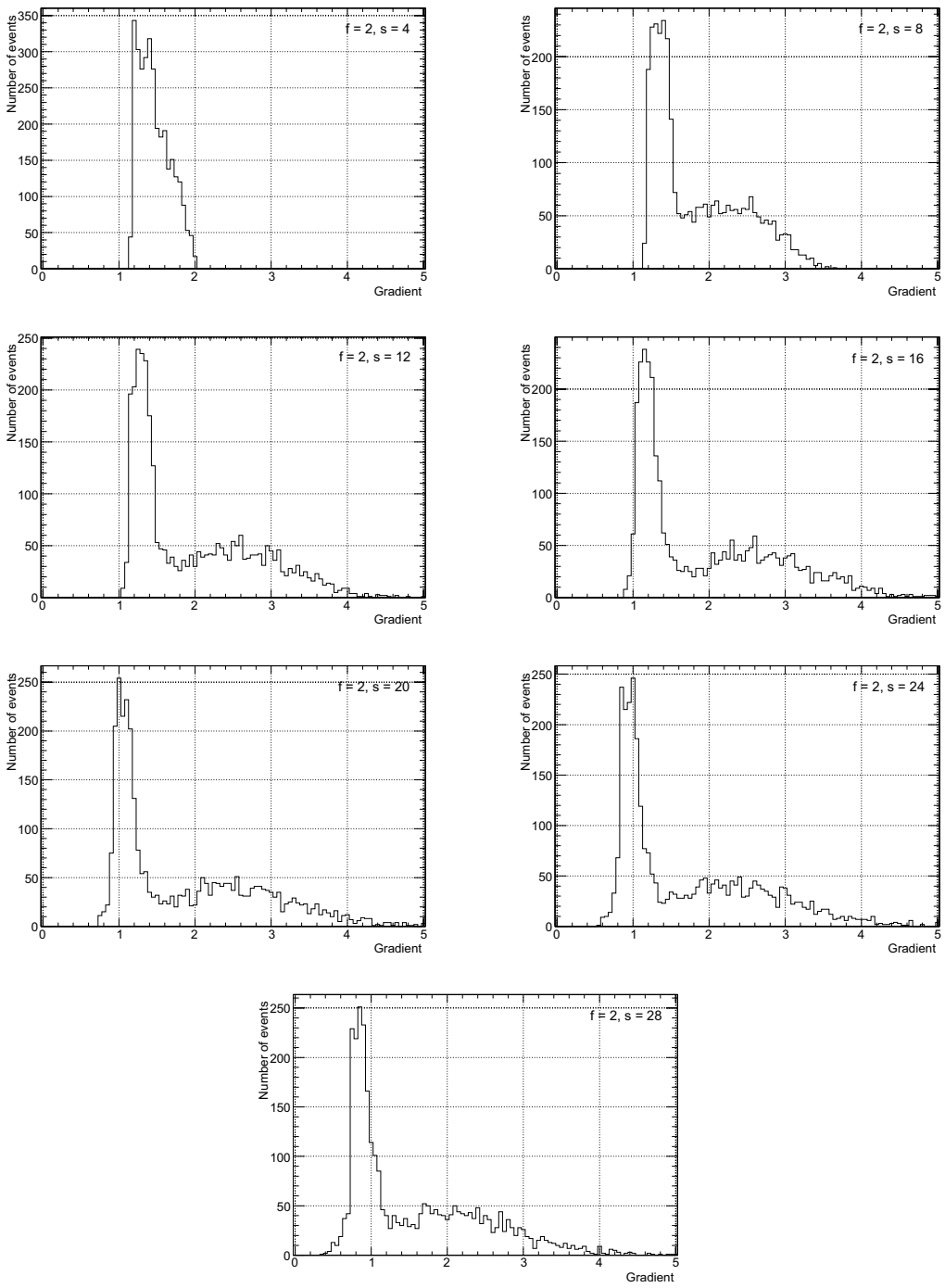

Figure B.5: Same as figure B.1, but for CP595H and $f = 2$.

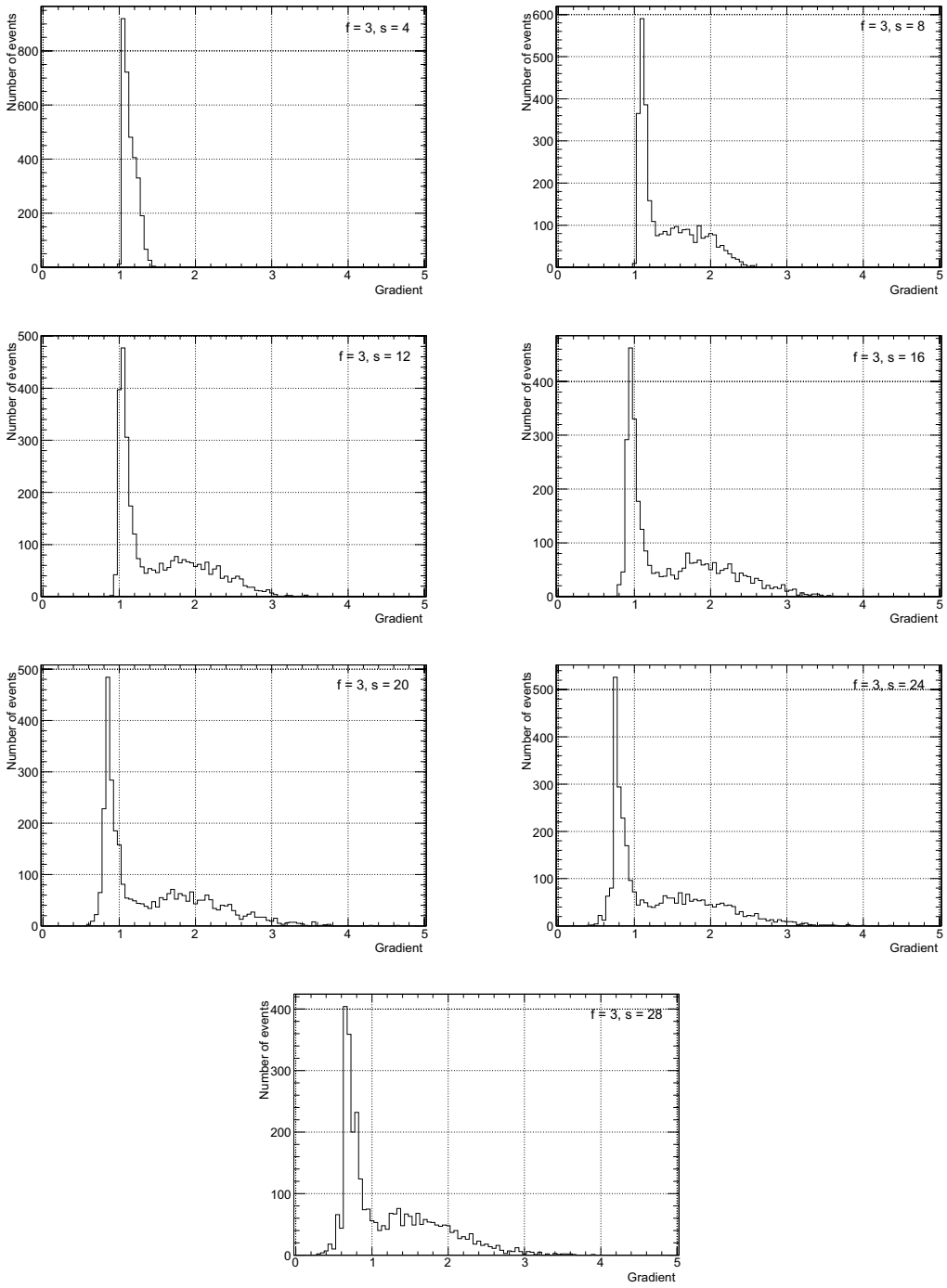

Figure B.6: Same as figure B.1, but for CP595H and $f = 3$.

Bibliography

[1] F. Lei, et al., Space Science Reviews 82 (1997) 309.

[2] M. C. Weisskopf, et al., Astrophysical Journal 208 (1976) L125.

[3] M. C. Weisskopf, et al., Astrophysical Journal 220 (1978) L117.

[4] E. H. Silver, et al., Astrophysical Journal 225 (1978) 221.

[5] K. S. Long, et al., Astrophysical Journal 238 (1980) 710.

[6] M. L. McConnell, et al., Advances in Space Research 34 (2004) 462.

[7] W. Coburn and S. Boggs, Nature 423 (2003) 415.

[8] R. E. Rutledge and D. B. Fox, Monthly Notices of the Royal Astronomical Society 350 (2004) 1272.

[9] C. Wigger, et al., Astrophysical Journal 613 (2004) 1088.

[10] H. Katagiri, et al., Proceedings of SPIE 6276 (2006) 62760Z.

[11] N. Produit, et al., Nuclear Instruments and Methods in Physics Research Section A 550 (2005) 616.

[12] J. Legere, et al., Proceedings of SPIE 5898 (2005) 413.

[13] S. Gunji, et al., Proceeding of the 28th International Cosmic Ray Conference (2003) 2779.

[14] R. Silva, et al., Proceedings of SPIE 4843 (2003) 543.

[15] T. Kamae, et al., Proceedings of SPIE 1734 (1992) 2.

[16] T. Kamae, et al., IEEE Transactions on Nuclear Science NS-40 (2) (1993) 204.

[17] T. Takahashi, et al., IEEE Transactions on Nuclear Science NS-40 (4) (1993) 890.

[18] S. Gunji, et al., Astrophysical Journal 397 (1992) L83.

[19] S. Gunji, et al., Astrophysical Journal 428 (1994) 284.

[20] S. Miyazaki, et al., Publications of the Astronomical Society of Japan 48 (1996) 801.

[21] N. Yamasaki, et al., Astrophysical Journal 481 (1997) 821.

[22] T. Kamae, et al., Proceedings of SPIE 2806 (1996) 314.

[23] T. Takahashi, et al., Astronomy and Astrophysics Supplement Series 120 (1996) 645.

[24] J. Kataoka, et al., Proceedings of SPIE 3445 (1998) 143.

[25] C. Tanihata, et al., Proceedings of SPIE 3765 (1999) 645.

[26] K. Makishima, et al., Astronomical Society of the Pacific Proceedings (H. Inoue and H. Kunieda, eds.) 251 (2001) 564.

[27] M. Kokubun, et al., IEEE Transactions on Nuclear Science NS-51 (2004) 1991.

[28] T. Takahashi, et al., Publications of the Astronomical Society of Japan 59 (2007) S35.

[29] M. Kokubun, et al., Publications of the Astronomical Society of Japan 59 (2007) S53.

[30] R. Blanford, et al., IEEE Nuclear Science Symposium Conference Record (2003) 1708.

[31] S. Larsson and M. Pearce, Nuclear Instruments and Methods in Physics Research Section A 525 (2004) 148.

[32] V. Andersson, et al., Proceedings of 22nd Texas Symposium on Relativistic Astrophysics at Stanford University (2004), posted at http://www.slac.stanford.edu/econf/C041213/papers/2508.PDF

[33] T. Mizuno, et al., Astrophysical Journal 614 (2004) 1113.

[34] K. Gunderson, et al., Proceedings of SPIE 5165 (2004) 158.

[35] S. J. Sturner, et al., Astrophysical Journal 445 (1995) 736.

[36] J. K. Daugherty and A. K. Harding, Astrophysical Journal 458 (1996) 278.

[37] K. S. Cheng, et al., Astrophysical Journal 300 (1986) 500.

[38] R. W. Romani and I.-A. Yadigaroglu, Astrophysical Journal 438 (1995) 314.

[39] R. W. Romani, Astrophysical Journal 470 (1996) 469.

[40] J. Dyks and B. Rudak, Astrophysical Journal 598 (2003) 1201.

[41] J. Dyks, et al., Astrophysical Journal 606 (2004) 1125.

[42] J. Poutanen, et al., Monthly Notices of the Royal Astronomical Society 283 (1996) 892.

[43] O. Engdegård, Master Thesis, submitted to Royal Institute of Technology (2006).

[44] T. Kii, Publications of the Astronomical Society of Japan 39 (1987) 781.

[45] M. B. Kiss, Master Thesis, submitted to Royal Institute of Technology (2006).

[46] Hamamatsu Photonics K.K., *Photomultiplier Tubes: Basics and Applications (Third Edition)*, Hamamatsu Photonics K.K. (2005).

[47] G. B. Rybicki and A. P. Lightman, *Radiative Processes in Astrophysics*, John Wiley & Sons (1979).

[48] HEXTE instrumental team, *The XTE Technical Appendix*, http://heasarc.gsfc.nasa.gov/docs/xte/RXTE_tech_append.pdf

[49] R. E. Rothschild, et al., Astrophysical Journal 496 (1998) 538.

[50] National Oceanic and Atmospheric Administration, National Aeronautics and Space Administration and United States Air Force, *U.S. Standard Atmosphere, 1976*, U.S. Government Printing Office (1976).

[51] T. Mizuno, et al., Nuclear Instruments and Methods in Physics Research Section A 540 (2005) 158.

[52] J. Kataoka, et al., Proceedings of SPIE 5898 (2005) 133.

[53] M. Arimoto, Master Thesis (in Japanese), submitted to Tokyo Institute of Technology (2006).

[54] T. Ylinen, Master Thesis, submitted to Royal Institute of Technology (2006).

[55] T. Shima, private communication.

[56] M. Arimoto, et al., talk in the Astronomical Society of Japan meeting (2006), Wakayama, Japan.

Following references are PoGOLite collaboration internal documents, available on request.

[57] T. Mizuno, *Update of Simulation of Crab Observation*, 2006/3/24.

[58] C. M. Bettolo and M. B. Kiss, *First results from the SAS BGO measurements*, 2006/6/4.

[59] T. Mizuno, *MC Study of PoGOLite trigger rate*, 2006/4/6.

[60] K. Yamamoto, et al., *Measurements of the Polarization Degree of the KEK Beam and the Response of the Plastic Scintillator* (in Japanese), 2006/2/2.

[61] T. Mizuno, *MC Simulation of Calibration Polarimeter Used for PoGO KEK Beam Test (updated)* (in Japanese), 2006/2/7.

Acknowledgments

I would like to thank my supervisors, Prof. Nobuyuki Kawai and Dr. Jun Kataoka for their guidance throughout two years of my master course. I especially express my gratitude to Dr. Jun Kataoka for the patient instruction in my experiments and report writing.

Many thanks go to all PoGOLite collaborators. Especially, Dr. Jun Kataoka, Dr. Tsunefumi Mizuno, Dr. Masaru Ueno have always advised and encouraged me. I would also like to thank Dr. Hiroyasu Tajima, Dr. Hiromitsu Takahashi, Makoto Arimoto, Kazuhide Yamamoto, Takuya Tanaka, Mozsi Kiss, Tomi Ylinen and Cecilia Marini Bettolo for the teamwork in the beam tests at the KEK-PF and the RCNP. Makoto Arimoto also provided me the Monte Carlo data. I am very grateful to Prof. Tsuneyoshi Kamae and Prof. Mark Pearce for their kind help in matters of my paper on the KEK-PF experiment.

This work has been performed under the approval of the Photon Factory Program Advisory Committee (Proposal No.2005G023) and the RCNP Beam-time Program Advisory Committee (Experiment No.E278). I greatly appreciate Dr. Shunji Kishimoto in the KEK-PF, Dr. Tatsushi Shima in the RCNP, and the staffs in both institutes for their generous and friendly support.

A very big thank goes to Teruyuki Okada and Tsuyoshi Ema in Hamamatsu Photonics K.K.. The PoGOLite PMT-ASSYs could not have been improved without their tireless efforts.

I wish to thank all members of Kawai group and Watanabe group. I especially acknowledge three former members, Tomoko Ikagawa, Yusuke Kuramoto and Takao Saito, for teaching me the ABCs of experiments and answering my stupid questions.

Finally, I would like to thank my family for the continuous support, which has allowed me live a comfortable life.